

SIMULATION STUDY OF LIPID BILAYER/NANOPARTICLE INTERACTIONS

by

Corey Evan Musolff

A DISSERTATION

Submitted
to Michigan State University
in partial fulfillment of the requirements
for the degree of

Physics - Doctor of Philosophy

2013

ABSTRACT

SIMULATION STUDY OF LIPID BILAYER/NANOPARTICLE INTERACTIONS

by

Corey Evan Musolff

A coarse-grained model is used to simulate lipid bilayers (LB) interacting with nanoparticles (NP). Different equilibrium states are observed as the size of the NP is varied along with the interaction strength between the NP and LB. Sufficient attraction causes the NP to become wrapped by the LB. Large NP are able to form pores in the LB. These various outcomes are explained using a continuum theory.

The same model is used to simulate pore healing in LB. It is observed that the area of the pore decreases linearly with time as explained by Allen-Cahn theory. Bulk properties of the LB can be used to predict the closing time of a pore as well as the amount of charge able to flow through the pore while it is open.

To my wife and advisor for their support and infinite patience.

TABLE OF CONTENTS

LIST OF TABLES	vi
LIST OF FIGURES	vii
CHAPTER 1 INTRODUCTION	1
CHAPTER 2 REVIEW	3
2.1 Introduction	3
2.2 Experimental Work	4
2.3 Atomistic Models	5
2.4 Coarse-Grained Models	6
2.4.1 Implicit Solvent	7
2.4.1.1 Tethered Models	7
2.4.1.2 Non-tethered Models	8
2.4.1.3 Cooke model	9
2.4.2 Explicit Solvent	11
2.4.2.1 MARTINI model	13
2.4.2.2 Klein model	15
2.5 Continuum Models	16
2.5.1 TGMB Theory	19
CHAPTER 3 THERMODYNAMICS OF NANOPARTICLE/LIPID BILAYER IN- TERACTIONS	21
3.1 Continuum Model Theory	21
3.1.1 Fixed boundary LB with spherical NP	22
3.1.1.1 Detached liposome (sphere)	24
3.1.1.2 Embedded liposome (sphere)	25
3.1.1.3 Partially wrapped spherical nanoparticle	26
3.1.1.4 Single layer micelle (sphere) states	28
3.1.2 Fixed boundary LB with infinite rod	31
3.1.2.1 Detached liposome (rod)	32
3.1.2.2 Embedded liposome (rod)	33
3.1.2.3 Partially wrapped rod-shaped nanoparticle	34
3.1.2.4 Single layer micelle (rod) states	35
3.1.3 Fixed tension ensemble	36
3.2 LB properties from simulation	38
3.3 Phase diagram	41
3.3.1 Fixed boundaries with spherical NP	41
3.3.2 Fixed boundaries with infinite rod NP	45
3.3.2.1 Small L	48
3.3.2.2 Large L	51

3.4	Comparison with Ginzburg and Balijepalli	51
3.5	Comparison with MD simulations	57
3.5.1	Implementation Details	57
3.5.2	MD Results	60
3.5.2.1	Spherical NP	60
3.5.2.2	Rod-shaped NP	62
CHAPTER 4	LIPID BILAYER PORE DYNAMICS	69
4.1	Tension required for pore formation	69
4.1.1	Fracture mechanics	69
4.1.2	Membrane rupturing	70
4.2	Dynamics of pore healing	71
4.2.1	Predicted time dependence	72
4.2.2	Simulation results	77
4.2.2.1	Flat LB	77
4.2.2.2	Spherical vesicle	80
4.2.2.3	Alternative fitting	83
4.2.2.4	Ion transfer	85
CHAPTER 5	CONCLUSION	87
APPENDICES	90
Appendix A	Ginzburg and Balijepalli Equations	91
Appendix B	Nosé-Hoover Thermostat/Barostat	95
BIBLIOGRAPHY	105

LIST OF TABLES

Table 4.1	Quadratic fit parameters for pore healing simulations	80
Table 4.2	Exponential plus quadratic fit parameters for pore healing simulations	84
Table 4.3	Double exponential fit parameters for pore healing simulations	85
Table 4.4	Charge transfer through pores	86

LIST OF FIGURES

Figure 2.1	Potential used in the Cooke model. The solid line indicates the attraction between tail beads. The dashed line indicates the hardcore repulsion for interactions involving head beads. For interpretation of the references to color in this and all other figures, the reader is referred to the electronic version of this dissertation.	11
Figure 3.1	Hydrophilic spherical NP states	23
Figure 3.2	Hydrophobic spherical NP states	30
Figure 3.3	Hydrophilic rod-shaped NP states	31
Figure 3.4	Hydrophobic rod-shaped NP states	36
Figure 3.5	Surface tension versus area in a flat LB. The green trace represents increasing area while the black trace represents decreasing area. The red circle indicates the critical point.	40
Figure 3.6	Phase diagram of spherical NP states. The x-axis shows the radius of the nanoparticle. The y-axis shows the attraction between the nanoparticle and lipid heads. Attraction increases with w . (A) Dissociated reference state, (D) Embedded liposome without a pore, (E) Embedded liposome with a pore, (I) Embedded single-layer micelle without a pore, (J) Embedded single-layer micelle with a pore. Schematics and energies for each phase are given in figures 3.1 and 3.2.	46
Figure 3.7	Phase diagram of short rod-shaped NP states. The x-axis shows the radius of the nanoparticle. The y-axis shows the attraction between the nanoparticle and lipid heads. Attraction increases with w . (A) Dissociated reference state, (D) Embedded liposome with and without a pore, (E) Embedded liposome with a spanning pore, (I) Embedded single-layer micelle with and without a pore, (J) Embedded single-layer micelle with a spanning pore. Schematics and energies for each phase are given in figures 3.3 and 3.4.	50
Figure 3.8	Phase diagram of long rod-shaped NP states. The x-axis shows the radius of the nanoparticle. The y-axis shows the attraction between the nanoparticle and lipid heads. Attraction increases with w . (A) Dissociated reference state, (D) Embedded liposome with and without a pore, (E) Embedded liposome with a spanning pore, (I) Embedded single-layer micelle with and without a pore, (J) Embedded single-layer micelle with a spanning pore. Schematics and energies for each phase are given in figures 3.3 and 3.4.	52

Figure 3.9	Phase diagram of spherical NP states. The x-axis shows the radius of the nanoparticle. The y-axis shows the attraction between the nanoparticle and lipid heads. (A) Dissociated reference state, (D) Embedded liposome without a pore, (E) Embedded liposome with a pore, (I) Embedded single-layer micelle without a pore, (J) Embedded single-layer micelle with a pore. Schematics and energies for each phase are given in figures (3.1 and 3.2). Data points indicate the results of Ginzburg and Balijepalli. (Blue circles): Embedded micelles with no pores. (Red squares): Embedded liposomes with no pores. (Green diamonds): Embedded liposomes with pores.	55
Figure 3.10	Area per lipid versus temperature from Cooke model simulation. The dark lines represent running averages of the raw data which is displayed as lighter dots. In the top trace the temperature is decreasing while in the bottom trace it is increasing. The gel to liquid transition occurs around $k_B T = 0.98 \epsilon$ while heating.	58
Figure 3.11	Radial distribution function for a lipid bilayer at various temperatures during the heating transition. The lack of long range order in $k_B T = 0.99 \epsilon$ indicates the liquid phase.	59
Figure 3.12	Typical starting configuration of my spherical nanoparticle/lipid bilayer simulations.	61
Figure 3.13	Cross section of single-layer hybrid micelle. A hydrophobic nanoparticle is embedded between two single layers of lipids.	61
Figure 3.14	Cross section of bilayer hybrid micelle. A hydrophilic nanoparticle is surrounded by a bilayer and embedded in the membrane.	62
Figure 3.15	Strongly hydrophilic nanoparticle is wrapped by a bilayer and causes a pore in the membrane.	63
Figure 3.16	Phase diagram of spherical NP states. The x-axis shows the radius of the nanoparticle. The y-axis shows the attraction between the nanoparticle and lipid heads. (A) Dissociated reference state, (D) Embedded liposome without a pore, (E) Embedded liposome with a pore, (I) Embedded single-layer micelle without a pore, (J) Embedded single-layer micelle with a pore. Schematics and energies for each phase are given in figures (3.1 and 3.2). Data points indicate my molecular dynamics results. (Blue circles): Embedded micelles with no pores. (Red squares): Embedded liposomes with no pores. (Green diamonds): Embedded liposomes with pores.	64
Figure 3.17	Typical starting configuration of my rod-shaped nanoparticle/lipid bilayer simulations.	65

Figure 3.18	Phase diagram of rod-shaped NP states. The x-axis shows the radius of the nanoparticle. The y-axis shows the attraction between the nanoparticle and lipid heads. (D) Embedded liposome with a small pore, (E) Embedded liposome with a spanning pore, (I) Embedded single-layer micelle with a small pore or no pore. Schematics and energies for each phase are given in figures (3.3 and 3.4). Data points indicate my molecular dynamics results. (Blue circles) : Embedded micelles with no pores. (Red squares) : Embedded micelles with small pores. (Green diamonds) : Embedded liposomes with spanning pores.	66
Figure 3.19	Narrow, hydrophobic, rod-shaped nanoparticle embedded in a bilayer. It is wrapped by a single layer of lipids and does not form a pore.	67
Figure 3.20	Thick, hydrophobic, rod-shaped nanoparticle embedded in a bilayer. It is wrapped by a single layer of lipids and does form a pore.	67
Figure 3.21	Strongly hydrophilic, rod-shaped nanoparticle embedded in a bilayer. It is wrapped by a double layer of lipids and has caused the membrane to rupture.	68
Figure 4.1	Snapshots of pore healing in a flat LB at three different times.	78
Figure 4.2	Pore area versus time in a flat lipid bilayer under zero tension. This is the raw data from 20 different runs.	78
Figure 4.3	Averaged pore area versus time in a flat lipid bilayer under zero tension. The data in figure 4.2 was averaged (red circles) and fit to a quadratic function (solid black line) as well as a linear function (dashed black line).	79
Figure 4.4	Snapshots of pore healing in a spherical vesicle at three different times.	81
Figure 4.5	Pore area versus time for a spherical vesicle. This is the raw data from 20 different runs.	81
Figure 4.6	Averaged pore area versus time for a spherical vesicle. The data in figure 4.5 was averaged and fit to both a linear and quadratic function.	82
Figure 4.7	Averaged flat lipid bilayer pore data with alternative fits. The data in figure 4.2 was averaged (red circles) and fit to a an exponential plus a linear term (solid green line) as well as a double exponential (dashed blue line).	84
Figure 4.8	Averaged vesicle pore data with alternative fits. The data in figure 4.5 was averaged (red circles) and fit to an exponential plus a quadratic function (solid green line) as well as a double exponential (dashed blue line).	85
Figure B.1	Histogram of kinetic energy for strong heat bath coupling ($Q = 0.648, T_{damp} = 0.005$). The scaling variable s fluctuates faster than the system and causes a bimodal, non-Gaussian distribution.	98

Figure B.2 Temperature versus time for various T_{damp} 99

Chapter 1

INTRODUCTION

I am interested in how nanomaterials interact with biological structures in the human body, specifically I am focused on interactions between nanoparticles (NP) and lipid bilayers (LB). NP can have both beneficial and adverse effects on living cells. Nano-sized structures are special because they are on the same size scale as lipids which are the building blocks of cell walls. Lipid molecules are roughly a few nanometers long, so that the thickness of a lipid bilayer is about 5 nm. Therefore, certain NP are able to penetrate cells under the right conditions and can disrupt the cell wall to varying degrees. NP are believed to be ideal drug delivery vehicles for this reason. If a drug molecule is not able to penetrate a cell on its own it may be able to be attached to a NP which can then be targeted to the cell. On the other hand certain NP can be toxic and are capable of rupturing cells. This has encouraged the active study of nanotoxicity. However, even this behavior could be useful if for instance cancerous cells are targeted.

NP/LB interactions have been looked at from many different angles. In chapter 2 I will give a review of recent experimental and theoretical work in this field. I have chosen to use molecular dynamics (MD) simulations to study the problem. MD can easily look at a system over a wide range of conditions without the usual experimental constraints. I would like to identify how NP/LB interactions are affected by fundamental properties such as the size, shape, and charge of NP. A deeper understanding of these relationships would be useful in explaining effects that have already been observed as well as predicting effects that have not yet been observed. New NP could be designed with certain properties to have desirable interactions or to prevent undesirable interactions.

In chapter 3 I look at the thermodynamics of NP/LB interactions. I use a continuum model to define the energy of various states. I then make phase diagrams showing the lowest energy states depending on the properties of the system. I have also run MD simulations which agree reasonably well with the predicted phase diagrams. Unlike the static states studied in chapter 3, chapter 4 looks

at the dynamics of pores in LB. I use a simple energy argument to predict the rate at which a pore will heal under different conditions. These predictions are again compared to MD simulations. My goal is to understand the general process of pore closing. In chapter 5 I will summarize my work and draw conclusions.

Chapter 2

REVIEW

2.1 Introduction

Understanding the interactions between nanoparticles (NP) and lipid bilayers (LB) is necessary for studying processes such as viral budding, endo/exocytosis, drug delivery, and harmful effects related to cytotoxicity. I am interested in the conditions under which nanoparticles become wrapped and possibly rupture lipid bilayers.

This chapter covers the experimental and theoretical work of others in the field, though an emphasis will be placed on molecular dynamics (MD) simulations. Experiments range from in vitro studies on small patches of LB to in vivo drug studies on animals. Simulations tend to focus on individual small scale interactions using a patch of LB or perhaps an entire vesicle or cell.

Simulations can take place over many length scales depending on the level of detail required, ranging from the atomic scale to that of the entire cell (four orders of magnitude!). A single simulation or model can not hope to bridge that gap. At the small end of the spectrum are atomistic or all-atom (AA) models. These of course have the advantage of including the most detail. We are confident that the interactions between individual atoms are understood well enough to create useful simulations. Unfortunately, these models are limited by computational constraints to looking at rather small systems (thousands of lipids) over short time scales (nanoseconds). Even with optimistic predictions for future computing power, these models will likely remain inadequate for looking at large patches of bilayers over long time scales (milliseconds).

At the other end of the spectrum are continuum models which do not have the same kind of size restrictions. A lipid membrane can be modeled as a simple two dimensional sheet. While these models can be used to study the large scale structural properties of the membrane, they are forced to ignore some of the details responsible for complicated interactions.

Between these two extremes lie any number of intermediate, mesoscale models. These coarse-grained models are similar to the AA models in that they simulate individual particle interactions, but instead of each particle representing a single atom these “beads” can represent several atoms. Typically, one bead will represent a few atoms. Besides a reduction in the number of particles being simulated, the interactions between them can also be simplified for instance from multi-body to pairwise forces. Another enormous simplification can be made if the solvent or water molecules surrounding the membrane are neglected. While water is in a sense responsible for lipid bilayer formation via the hydrophobic effect, bilayer formation can still be achieved by using effective forces. These are so called implicit solvent models while those that include water molecules are explicit solvent models. Since there are many more water molecules surrounding the cell than the number of lipids, neglecting the water allows much larger and longer simulations.

I will first review experiments in the field in section 2.2. Then I will review various theoretical models ranging from atomistic to continuum in sections 2.3-2.5. Special emphasis will be given to a few coarse-grained (CG) models because I have chosen to use a CG model for my simulations.

2.2 Experimental Work

Interactions between NP and LB require a mutual attraction. Hou et al. looked at the accumulation of functionalized gold NP on LB. They observed that adsorption depended on the specific functionalization as well as the pH of the system [1]. After allowing some time for the NP to adhere, they measured the total mass of the accumulated NP using inductively coupled plasma- optical emission spectroscopy (ICP-OES). A wide range of NP sizes (1-100 nm) were tested with larger NP producing a higher NP mass concentration on the membrane while smaller NP accumulated in larger numbers producing a higher number concentration.

In addition to a NP simply adsorbing to a LB surface there are various ways in which it can disrupt the surface, forming pores. Pore formation can be observed either directly by using an imaging method such as atomic force microscopy (AFM) [2, 3, 4, 5, 6], or indirectly by measuring the flow of current [7, 8] or dye molecules [5, 6, 7] across the membrane.

The method of measuring current flow across a membrane requires an applied voltage. While the membrane is intact, its natural resistance will prevent current flow. Any spikes in current indicate a pore. de Planque et al. used this technique to test the dependence of NP size and functionalization on membrane disruption [8]. They found that small (50 nm) unfunctionalized silica NP caused more disruption than when they were amine-functionalized. Conversely, larger (500 nm) NP caused no disruption unless they were functionalized. This implies a balance between size and functionalization.

The effect of NP size alone was studied by Roiter et al. [2, 3]. They began by placing various sized silica NP on a smooth silica substrate. Then a LB was formed over the top. AFM was used to observe any pores formed in the membrane. NP smaller than 1.2 nm only slightly deformed the surface and did not produce any pores. Larger NP (1.2-22 nm) did result in pore formation. Smooth NP larger than 22 nm caused significant deformation of the membrane as it wrapped around the NP, though they did not produce any pores. Large NP with sharp features or bumps with higher curvature were also able to form pores. This intermediate range of NP sizes can be explained by balancing the cost of bending the membrane against the favorable attraction between the NP and LB. I will discuss this in detail in the next chapter.

Attraction between NP and LB is greatly affected by the charge of the NP. This was demonstrated in an experiment by Hong et al. [6] in which both supported LB and cells in vitro were exposed to various polymer NP. The main determining factor for pore formation was the charge concentration on the NP. Positively charged NP are known to be more attracted to LB which tend to have a slight negative charge.

Medical research often focuses on either the toxicity of NP [9] or their use in drug delivery [10, 11].

2.3 Atomistic Models

Atomistic models allow simulations on the smallest scale possible under classical mechanics. Lyubartsev and Rabinovich published a recent review of current simulation techniques and fo-

cused on atomistic models [12]. In these models individual atoms interact through Lennard-Jones and Coulomb forces. The three most popular models are GROMOS, CHARMM, and AMBER.

The GROMOS model was developed at the University of Groningen in 1978 by van Gunsteren et al. and is an acronym for GRONingen MOlecular Simulation [13, 14]. It makes the simplification of combining hydrogen atoms with the heavy atom they are bound to. The parameters have been refined over the years. The newest set includes parameters for additional dihedral-angle and torsional-angle terms [15]. Poger et al. presented a modified set optimized for dipalmitoylphosphatidylcholine (DPPC) lipids which produced lipid area and volume densities in agreement with experiments [16].

CHARMM was created at Harvard and is an acronym for Chemistry at HARvard Macromolecular Mechanics [17, 18]. In contrast to GROMOS, CHARMM treats hydrogen atoms explicitly and has its own set of Lennard-Jones, Coulomb, and bond energy parameters. A recent parameter set was developed specifically for lipids [19].

AMBER was developed at the University of California, San Francisco and is an acronym for Assisted Model Building with Energy Refinement [20]. It was originally designed to model nucleic acids and proteins. A newer version called the general Amber force field (GAFF) was created to simulate drug molecules [21]. It was recently shown to accurately simulate LB [22].

Tieleman used the GROMOS model to simulate electroporation in LB [23]. In the simulation he applied a voltage across a pure LB surrounded by water. At an electric field strength of 0.5 V/nm he observed pores forming over the span of one nanosecond. Another study by Tarek used CHARMM to look at similar processes including resealing of the pore after the electric field is turned off [24].

2.4 Coarse-Grained Models

I am most interested in using coarse-grained (CG) models to study LB. They are able to strike a balance between the detailed realism of atomistic models and the large scale and speed of continuum models. Several reviews have been written about current CG models [25, 26, 27, 28, 29, 30, 31].

The term coarse-grained is somewhat broad and can include a wide range of detail. Different CG models have varying levels of complexity depending on the properties being studied. It is possible for very simple models to accurately simulate large scale structural properties. They are near the continuum model end of the spectrum. Many levels of complexity can be added including the number of beads, the types of interactions between beads, and the inclusion of solvent beads. These details bring us closer to the atomistic end of the spectrum and are necessary for capturing nanoscale processes.

Certain interesting NP/LB interactions take place on patches of LB which are hundreds of nanometers wide (hundreds of thousands of lipids) and occur over millisecond time scales. These scales are completely beyond the current capabilities of AA models. I will discuss the current CG models available which I classify as either implicit or explicit solvent models. I will describe three of the most popular models in more detail.

2.4.1 Implicit Solvent

The simplest and fastest models available employ an implicit solvent, meaning that the solvent molecules, usually water, are not included in the simulation. These are a good place to start when looking at LB systems if you are primarily interested in the large scale structural properties of the LB itself. At first glance it seems impossible to model LB without including water. Water is responsible for creating and keeping LB together through the hydrophobic effect. Lipids are not held together by their own attraction to each other. Rather the hydrophobic tails are repelled by the water and form micelles and bilayers in order to wall themselves off from it. To solve this problem, the LB structure must be maintained by other means. The typical methods are either to tether the head beads or to include an effective attractive force between tail beads.

2.4.1.1 Tethered Models

In tethered models the head beads are either tethered to their neighbors or else confined to move along a two dimensional sheet with certain given properties [32]. Similar to continuum models,

tethered models are tuned to reproduce structural surface properties. While the level of detail is greater than in continuum models and one is able to look at lipid diffusion and surface dynamics, it is still fairly limited. LB formation and surface pore formation are not observable with such models. Brannigan et al. discuss recent tethered model applications in their review [26].

2.4.1.2 Non-tethered Models

Without tethering or solvent molecules, effective forces are needed to hold the LB together. If an attractive force is used between tail beads, lipids will naturally aggregate into micelles and bilayers. These models can be used to study such formations. Effective force models can capture much more dynamic behavior, but it can be tricky to tune the attractive forces just right. Early such models could not produce a liquid phase. The Lennard-Jones type pair forces used proved to be too short ranged. Forces strong enough to hold the lipids together tend to form solid structures, but fall apart at higher temperatures. LB in their natural state should have a robust liquid phase. It was shown by Drouffe in the early 1990's that multibody forces could be used to produce a liquid phase [33]. In the early 2000's a few groups proposed pair potential models also capable of producing a liquid phase. Pair potentials are much more desirable because they are computationally simpler and can be easily implemented by popular molecular dynamics software packages.

The Farago model uses rigid lipids composed of three beads and a different Lennard-Jones potential for each combination of bead type [34]. Farago was able to produce a liquid-gel phase transition and to look at membrane elasticity and pore formation. The bending rigidity found using this model was significantly higher than was expected for a single component membrane. Other downsides of the model are that it can not spontaneously form bilayers and that the number of potential combinations is somewhat cumbersome.

Brannigan and Brown proposed a model using spherocylinders to represent each lipid [35]. The pair potential between lipids depended on their distances from each other as well as their relative angles. Their model could reproduce the same behavior as the Farago model as well as being able to self assemble.

2.4.1.3 Cooke model

Around the same time, Cooke et al. [36, 37] proposed their own model. Each lipid in the Cooke model consists of three beads, one hydrophilic head bead and two hydrophobic tail beads. Interactions are limited to simple pair potentials which I will describe presently. All non-bonded beads experience a hardcore repulsion via a Weeks-Chandler-Andersen potential

$$V_{rep}(r;b) = \begin{cases} 4\epsilon \left[\left(\frac{b}{r}\right)^{12} - \left(\frac{b}{r}\right)^6 + \frac{1}{4} \right], & r \leq r_c \\ 0, & r > r_c \end{cases} \quad (2.1)$$

which is simply a shifted Lennard-Jones potential cut off at the minimum $r_c = 2^{1/6}b$. The length scale in the model is set by the diameter of a tail bead $\sigma = b_{tail,tail} \simeq 0.9$ nm. The authors claim that the head bead should be slightly smaller in order to ensure the correct lipid shape. Therefore they use $b_{head,head} = b_{head,tail} = 0.95\sigma \simeq 0.86$ nm. I have run most of my simulations at $k_B T = 0.9\epsilon$. Assuming this is near room temperature, a rough energy scale is found to be $\epsilon \approx 2\text{-}3$ kJ/mol.

Individual lipids are held together by strong FENE (finitely extensible nonlinear elastic) bonds of the form

$$V_{bond}(r) = -\frac{1}{2}k_{bond}r_\infty^2 \log \left[1 - \left(\frac{r}{r_\infty}\right)^2 \right] \quad (2.2)$$

where $k_{bond} = 30\epsilon/\sigma^2$ is the stiffness and $r_\infty = 1.5\sigma$ is the divergence length. Lipids are kept straight by a harmonic potential between the two end beads

$$V_{bend}(r) = \frac{1}{2}k_{bend}(r - 4\sigma)^2 \quad (2.3)$$

which has a rest length of 4σ . $k_{bend} = 10\epsilon/\sigma^2$ is the bending stiffness of the lipid. In addition to the aforementioned hardcore repulsion experienced by all non-bonded beads, tail beads feel a broad attraction to each other of the form

$$V_{attr}(r) = \begin{cases} -\varepsilon, & r < r_c \\ -\varepsilon \cos^2\left(\frac{\pi(r-r_c)}{2w_c}\right), & r_c \leq r \leq r_c + w_c \\ 0, & r > r_c + w_c \end{cases} \quad (2.4)$$

This is a square well potential of depth ε below r_c which then tapers to zero between r_c and $r_c + w_c$. The total inter-lipid bead potentials are shown in figure 2.1. The key to the Cooke model is the width of the potential, w_c , which determines the properties of the bilayer such as the melting temperature. It is the only tunable parameter. The reason why previous pair potential models failed to produce a liquid phase was that the potential wells were too narrow. Cooke et al. argued that the form of the potential is unimportant as long as it is wide [37]. To demonstrate this they tried two different forms of the potential. One simply inserted a flat extension from the minimum of the normal LJ potential while the other slowly tapered the energy from the minimum to zero following the smooth cosine squared shape shown in the figure. They showed that both potentials behaved similarly and were both able to produce a liquid phase.

An estimated timescale can be calculated based on the other parameters $\sigma\sqrt{m/\varepsilon} \approx 10$ ps. However, the effective timescale can be much longer for coarse-grained models with relatively few degrees of freedom [38, 39]. Cooke and Deserno estimated the effective timescale for the Cooke model to be $\tau \approx 10$ ns [37, 40] by comparing their simulated diffusion constant with experiment [41].

The Cooke model was originally used to study several LB properties including lipid density, diffusion, and bending energy. The authors looked at the effects of stress on LB observing pore formation and buckling which was previously impossible using tethered models [36, 37]. Deserno has further used the model to simulate interactions with proteins [40]. Ruiz-Herrero et al. have used the Cooke model to simulate the wrapping of NP by flat LB under zero tension. The Cooke model appears to contain enough detail to simulate realistic nanoparticle interactions. At the same time its simplicity and coarseness allow simulations over large size (100 nm) and time (milliseconds) scales. That is why I have chosen to use this model in my own simulations. I will discuss my

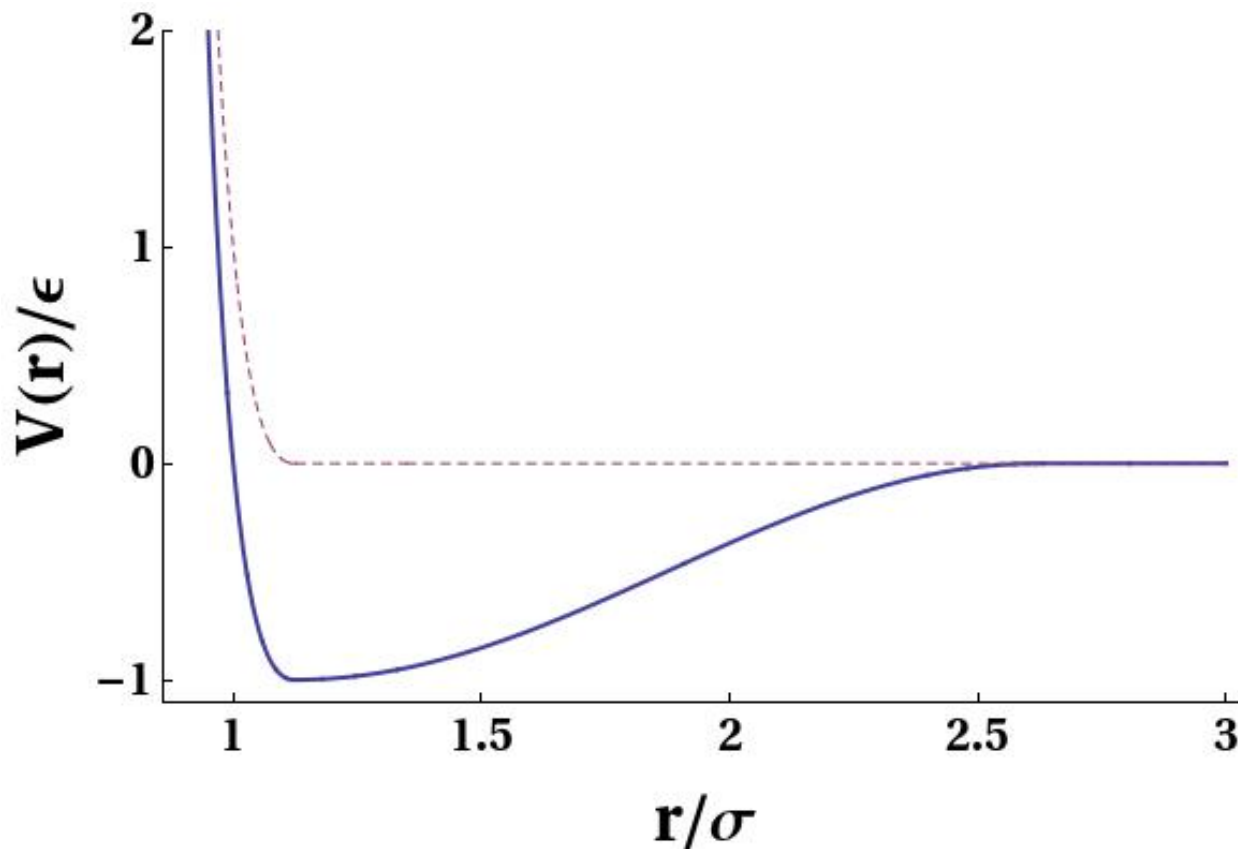


Figure 2.1: Potential used in the Cooke model. The solid line indicates the attraction between tail beads. The dashed line indicates the hardcore repulsion for interactions involving head beads. For interpretation of the references to color in this and all other figures, the reader is referred to the electronic version of this dissertation.

implementation of the Cooke model in chapter 3.

2.4.2 Explicit Solvent

As the name suggests, explicit solvent models differ in that they include explicit solvent beads, usually water. The size of the solvent beads are generally chosen to be similar to that of the lipid beads. For that reason water beads tend to represent multiple water molecules. I will describe some of the current models below.

One of the first explicit solvent models was developed by Goetz and Lipowsky [42]. They used three types of beads. Lipids consisted of one or two tail chains containing four hydrophobic beads each. Head groups were made up of either one or three hydrophilic beads depending on whether

the lipid was single or double tailed. The solvent beads were treated the same as hydrophilic head beads. All three beads had the same mass. Hydrophilic and hydrophobic beads interacted through a strictly repulsive soft-core ($1/r^9$) potential. Hydrophilic beads, both water and head beads, were attracted by a Lennard-Jones potential. Lipids were held together by harmonic potentials. They looked at both rigid and floppy lipids by including a bond bending potential. Their model was able to self assemble fluid bilayers and micelles and they were able to measure the properties of those structures. A very similar model was used by Stevens et al. to study liposome fusion [43].

Loison et al. used a similar model to study pore formation in LB [44, 45]. The Loison model represents each lipid with two hydrophilic head beads and two hydrophobic tail beads. Solvent beads consist of a single bead which represents approximately three water molecules. Individual beads are bound together by strong FENE bonds. All beads are repelled at short range by a Lennard-Jones like potential. Beyond the Lennard-Jones minimum, beads from different lipids and solvent beads are attracted by the potential

$$U(r) = \frac{\phi}{2} \left[\cos(\alpha r^2 + \beta) - 1 \right] \quad (2.5)$$

α and β determine the cutoff radius at which the potential becomes zero and above which the potential remains zero. The potential depth, ϕ , determines the strength of the potential. It is the same for all pairs of beads of the same type as well as between head and solvent beads. Tail beads are not attracted to head or solvent beads, making the corresponding ϕ value zero. Apart from the addition of water molecules, this looks very similar to the Cooke model [36, 37]. The shape of the attractive part of the potential is slightly different. The more gradual increase approaching the cutoff radius does affect the stability of the membrane. Loison et al. found that the bilayer state was unstable in the presence of large amounts of solvent [45].

The explicit solvent models listed thus far share the fact that they use simple effective forces which are tuned to recreate large scale behavior. They also tend to use very few types of beads. These characteristics make them similar to the implicit solvent models. Also, the models mentioned thus far have not used any electrostatic forces. The next group of explicit solvent

models differ in that they try to simulate atomic scale interactions more accurately. They use a larger variety of beads as well as a variety of potentials to simulate the different interactions between species. Electrostatic forces are also included. The added details make these models more complicated and less general, but arguably more realistic depending on the system. The two most popular models in this regime are the MARTINI [46, 47] and Klein [48, 49, 25] models. Each uses beads consisting of four heavy atoms that interact through Lennard-Jones and electrostatic forces. I will explain both of these models in more detail below.

Dissipative particle dynamics (DPD) was developed as an alternative to traditional molecular dynamics (MD) by Hoogerbrugge and Koelman [50, 51]. Groot and Rabone adapted this method to simulate LB [52]. Their model uses beads consisting of three heavy atoms which is comparable to the MARTINI and Klein models. Each bead experiences a conservative force, a random force, and a drag force. The conservative force defines a cutoff radius, below which beads feel a repulsion that increases linearly as they get closer. This extremely soft repulsion greatly increases diffusion. The time step used in MD is limited by the usual hard-core repulsion between beads. Trajectories must be updated frequently in MD to make sure beads don't wander too close together. Without having to worry about the infinite energy of overlapping beads, DPD can use a time step 1000 times larger than in MD. The coarse-graining gives an additional effective speedup, allowing Groot and Rabone to use a time step of about 5 ps.

2.4.2.1 MARTINI model

Marrink et al. developed a popular coarse grained model called MARTINI [46, 47]. MARTINI classifies 18 different building blocks for lipids and solvents. Each bead represents about four heavy atoms. A typical lipid is therefore composed of about twelve beads. The main distinction between beads is polarity. Beads are classified as being polar, nonpolar, apolar, or charged. Nonpolar and charged beads are subdivided according to their affinity for hydrogen bonding. The subtypes are donor, acceptor, both, or none. Polar and apolar beads are assigned a number from one to five indicating its degree of polarity.

Lipids are held together by a weak harmonic potential between nearest neighbors

$$V_{bond}(R) = \frac{1}{2}K_{bond}(R - R_{bond})^2 \quad (2.6)$$

where $K_{bond} = 1250 \text{ kJ mol}^{-1} \text{ nm}^{-2}$ and $R_{bond} = 0.47 \text{ nm}$ for every combination of beads.

Next nearest neighbors experience a bending potential

$$V_{angle}(\theta) = \frac{1}{2}K_{angle}[\cos(\theta) - \cos(\theta_0)]^2 \quad (2.7)$$

where $K_{angle} = 25 \text{ kJ mol}^{-1}$ and $\theta_0 = 180^\circ$ for most types of bonds. Besides nearest neighbors, every combination of beads experiences one of ten different Lennard-Jones potentials.

$$U_{LJ}(r) = 4\varepsilon_{ij} \left[\left(\frac{\sigma_{ij}}{r} \right)^{12} - \left(\frac{\sigma_{ij}}{r} \right)^6 \right] \quad (2.8)$$

The interaction strengths, ε_{ij} , vary from 2.0-5.6 kJ/mol. The closest approach distance, σ_{ij} , equals 0.47 nm for all but a couple interactions. The final contribution is the Coulomb potential for charged beads.

$$U_{el}(r) = \frac{q_i q_j}{4\pi\varepsilon_0\varepsilon_r r} \quad (2.9)$$

Screening is enforced by setting $\varepsilon_r = 15$. The original model had the problem of water beads freezing near room temperature. The newest version inhibits nucleation by replacing 10% of the water beads with “antifreeze” beads that have an effective radius of 0.57 nm instead of the typical 0.47 nm.

Model parameters have been tuned to reproduce experimental results. The use of 18 different building blocks allows the MARTINI model to capture a wide variety of interactions while keeping a manageable number of parameters. The effective reduction in the number of atoms along with the use of simple pair interactions makes it possible to simulate larger systems over longer times compared to all-atom models. Simulations can be run with a time step of about 40 fs. The effective timescale is about four times longer than that due to the lack of friction.

The MARTINI model has been used to simulate NP/LB interactions. A molecular dynamics study by Lee and Larson found membrane pore formation caused by small dendrimers ($R \approx 2$ nm) [53]. Nanoparticle shape is another important factor. Nangia and Sureshkumar performed MD simulations of NP with various shapes and charge densities interacting with LB [54]. They found that shapes with high aspect ratios like rice were able to translocate more easily than spheres.

2.4.2.2 Klein model

Another earlier model was developed by Shelley et al. to specifically simulate dimyristoylphosphatidylcholine (DMPC) lipids [48, 49, 25]. Water beads represent four water molecules and interact with each other via a Lennard-Jones 6-4 potential

$$V(r_{ij}) = \frac{15}{4} \epsilon_{\alpha\beta} \left[\left(\frac{\sigma_{\alpha\beta}}{r_{ij}} \right)^6 - \left(\frac{\sigma_{\alpha\beta}}{r_{ij}} \right)^4 \right] \quad (2.10)$$

The parameters were calibrated to reproduce the correct melting temperature of DMPC. The lipid tails consist of two different beads, $(CH_2)_3$ and $(CH_2)_2 - CH_3$. The heads are made up of choline, phosphate, glycerol backbone, and ester group beads. Adjacent beads are bound together by a harmonic potential

$$V(r_{ij}) = \frac{k_{b;\alpha\beta}}{2} (r_{ij} - r_{0;\alpha\beta})^2 \quad (2.11)$$

The bond angles among tail beads are governed by a cosine potential

$$V(\theta_{ijk}) = k_{\theta;\alpha\beta\gamma} [1 - \cos(\pi - \theta_{ijk})] \quad (2.12)$$

These parameters are tuned by comparing with atomistic simulations. Bond angles involving head beads are governed by a quartic bond angle potential

$$V_Q(\theta_{ijk}) = AB^2/4 \quad (2.13)$$

$$A = K_{\theta;\alpha\beta\gamma}/(2d_0)$$

$$B = d_0 - (\theta_{ijk} - \pi)^2$$

$$d_0 = (\theta_{0;\alpha\beta\gamma} - \pi)^2$$

All non-bonded interactions other than water-water are given by a Lennard-Jones 9-6 potential

$$V(r_{ij}) = \frac{15}{4} \epsilon_{\alpha\beta} \left[\left(\frac{\sigma_{\alpha\beta}}{r_{ij}} \right)^9 - \left(\frac{\sigma_{\alpha\beta}}{r_{ij}} \right)^6 \right] \quad (2.14)$$

These parameters were determined by matching densities from experiments and radial distribution functions from atomistic simulations. Finally, the choline and phosphate beads were assigned respective charges of +e and -e and a dielectric constant of 78.

The Klein model is a niche model designed to study a very specific type of lipid (DMPC). Its parameters have been finely tuned to accurately represent that system. The coarseness of the model is about the same the MARTINI model with an entire lipid consisting of thirteen beads. The bond length and bond angle potentials must be calculated every femtosecond while the non-bonded interactions less than 11 Å are updated every 2 *fs* and longer non-bonded interactions are updated every 40 *fs*.

2.5 Continuum Models

Continuum models are useful tools for studying the shape and large scale dynamics of LB [55, 56, 26]. LB lend themselves to continuum models due to their relatively simple morphology and the large number of lipids usually involved. Bulk parameters such as bending energy and surface tension act as inputs to the models. Some recent reviews of continuum models are given by Brannigan et al. [26] and Brown [57].

Canham was one of the first to use such a model to understand the shapes of red blood cells [55]. He was able to produce a variety of shapes by minimizing bending energy alone. Shortly after, Helfrich developed a similar model which has become the standard [56]. He considered three types of strain: stretching, tilt, and curvature. He found that the curvature modulus is much smaller than the stretching or tilt moduli. That means that the surface area and tilt of the LB tend to remain

fixed and that the shape of the LB is determined mostly by the curvature. He also argued that tilt is less important than stretching. The Canham-Helfrich (C-H) Hamiltonian of the LB, neglecting tilt, is given by [27, 55, 56, 58]

$$\mathcal{H} = \int d^2A \left(\gamma + \frac{\kappa}{2} (C_1 + C_2 - C_0)^2 + \bar{\kappa} C_1 C_2 \right) \quad (2.15)$$

where γ is the lateral membrane tension. κ and $\bar{\kappa}$ are the bending rigidity and saddle-splay modulus. C_1 and C_2 are the local curvatures. For a sphere of radius R , $C_1 = C_2 = 1/R$. C_0 is the spontaneous curvature which is zero as long as the LB composition is the same on both sides. I will make that assumption in later calculations. For a LB of fixed topology the last term in the integral will contribute only a constant and can therefore be neglected. Yoo et al. calculated the energy of bending that occurs around the edge of a pore to find the equilibrium shape and compared with MD simulations [59].

In addition to bending energy there is a stretching energy associated with stretching or compressing bonds in the membrane. To lowest order it is assumed that the stretching energy is proportional to the square of the change in area. If the membrane is interacting with another surface such as a NP, there will also be an adhesion energy proportional to the contact area.

Deserno has used continuum models to find equilibrium configurations involving NP and LB [60, 61, 62, 40]. A paper by Deserno and Gelbart [60] looked at the interactions between spherical colloids and spherical vesicles. They considered the following factors: the sizes of the colloid and vesicle, the adhesion energy between them, and also the surface tension and bending energy of the vesicle. The colloid was treated as a hard sphere while the vesicle was able to deform while binding with the colloid. The energy contributions they considered were the adhesion energy between the colloid and vesicle (E_{ad}), the tension energy of the stretched vesicle (E_{ten}), and the curvature energy for bending the vesicle (E_c).

$$E_{total} = E_{ad} + E_{ten} + E_c \quad (2.16)$$

$$E_{ad} = -k_{ad} A_{ad} \quad (2.17)$$

$$E_{ten} = \frac{k_{ten}}{2} \frac{[\max(A; A_1) - A_1]^2}{A_1} \quad (2.18)$$

$$E_c = \oint \frac{1}{2} k_c (\kappa_1 + \kappa_2)^2 dA \quad (2.19)$$

where k_{ad} is the adhesion constant and A_{ad} is the area of contact. k_{ten} is the lateral compressibility, A_1 is the unstretched vesicle surface area, and A is equilibrium stretched area. The \max function in E_{ten} ensures that the vesicle will only stretch and can not be compressed. E_c is simply the Helfrich energy defined above, neglecting the Gaussian and spontaneous curvatures. The energy gain through adhesion must be balanced against the deformation costs.

For a given set of vesicle and colloid sizes and membrane parameters they were able to minimize the energy to find how far the colloid penetrated as well as the curvature of the vesicle near separation. They found that vesicles greater than a certain minimum ($R \sim 300$ nm) were able to completely envelop colloids within a certain range of sizes. Colloids that were too large were only partially wrapped. Vesicles below the critical size could only achieve partial wrapping regardless of the size of the colloid. Very small colloids were not able to penetrate the vesicle at all and remained unbound. In that case the surface tension cost overwhelmed the potential gain from adhesion.

Other studies have looked at the interactions of NP with flat membranes and found similar conditions for partial or complete wrapping [62, 61, 63]. In a more recent paper Deserno calculated the tension required to form a pore in a membrane in the absence of a NP which agreed with coarse-grained MD simulations [40].

Van Lehn and Alexander-Katz also used the C-H Hamiltonian to model NP interacting with a LB under zero tension [64]. Their NP consisted of two different phases which were either hydrophilic or hydrophobic and were free to mix. This caused different adhesion energies depending on which part of the NP was in contact with either the lipid head or tail region. In addition to the bending and adhesion terms, they included the mixing energy for the NP surface. They predicted varying degrees of penetration depending on the adhesion strengths and ratio of phases on the NP which they compared to their own MD simulations.

2.5.1 TGMB Theory

Although different from the continuum models above, Ginzburg and Balijepalli used a combination of self-consistent field theory and density functional theory to model the interaction between NP and LB [65]. Their work is significant because it proposes a phase diagram of NP/LB states. They predict outcomes based on NP properties which can be compared to other theories and experiments. I have run simulations closely following the conditions used by Ginzburg and Balijepalli. I will present a comparison in chapter 3.

The technique was developed earlier by Thompson, Ginzburg, Matsen, and Balazs (TGMB) to model the interaction between NP and block polymers [66, 67]. In the Ginzburg and Balijepalli adaptation, diblock polymers are replaced by lipid diblocks (D) which have hydrophilic (H) and lipophilic (L) parts. The other two components are the water solvent (W) and the nanoparticle (P). The total free energy can be written as

$$\frac{FN_D}{k_B T \rho_0 V} = f_1 + f_2 + f_3 + f_4 \quad (2.20)$$

$$f_1 = \frac{\phi_P}{\alpha} \ln \left(\frac{Q_P}{V} \right) - \phi_D \ln \left(\frac{Q_D}{V} \right) - N_D \phi_W \left(\frac{Q_W}{V} \right) \quad (2.21)$$

$$f_2 = \frac{1}{V} \int dr \left[\sum_{\alpha, \beta} \left(\chi_{\alpha\beta} N_D \right) \phi_\alpha(r) \phi_\beta(r) - \xi(r) \left(1 - \sum_{\alpha} \phi_\alpha(r) \right) \right] \quad (2.22)$$

$$f_3 = \frac{1}{V} \int dr \left[- \sum_{\alpha (\neq P)} w_\alpha(r) \phi_\alpha(r) - w_P(r) \rho_P(r) \right] \quad (2.23)$$

$$f_4 = \frac{1}{V} \int dr \left[\rho_P(r) \Psi_{CS}(\bar{\phi}_P(r)) \right] \quad (2.24)$$

The first term, f_1 (2.21), contains the entropic free energies. The second term, f_2 (2.22), contains the local interactions determined by Flory-Huggins parameters [68, 69]. I will explain each of the contributions in detail in appendix 5.

Ginzburg and Balijepalli solved the above field equations on a two dimensional lattice 120x120. The size of each lattice site was 0.36 nm on a side making the total lattice roughly 43x43 nm². They used nanoparticles of radii ($R_p = 1.6, 2.0, 2.4, 2.8, \text{ and } 3.2$ nm). The nanoparticles were

made stationary and their densities were defined by sharp Gaussian functions. The Flory-Huggins parameters for the interactions between nanoparticle (P), water (W), hydrophilic (H), and lipophilic (L) blocks were as follows: $\chi_{HL} = \chi_{WL} = 1.0$ meaning that the lipophilic blocks will separate from the water and hydrophilic blocks. $\chi_{WH} = \chi_{PL} = 0.0$ meaning that water and hydrophilic blocks as well as nanoparticle and lipophilic blocks are as likely to mix as not. $\chi_{PW} = 1.0$ while χ_{PH} varies from +1.0 (repulsive) to -3.0 (strongly attractive). They argue that $\chi_{PH} = +1.0$ corresponds to uncharged or hydrophobic nanoparticles while $\chi_{PH} = -3.0$ corresponds to highly charged nanoparticles. It is known that nanoparticles are attracted more strongly to bilayers when charged [70, 71]. The values of χ_{PL} and χ_{PW} make it more favorable for the nanoparticle to become absorbed into the lipophilic region than to remain separated from the membrane. The other possible configuration is for the nanoparticle to become surrounded by the bilayer in contact with the hydrophilic blocks. The most favorable configuration is determined by the size of the nanoparticle and the interaction between nanoparticle and hydrophilic block.

They found that electrically neutral nanoparticles were absorbed into the center of the bilayer for all particle sizes tested. As the charge density was increased (χ_{PH} decreased) the nanoparticle-hydrophilic block interactions became more favorable. Charged nanoparticles were coated by a bilayer of lipids instead of the monolayer needed for the uncharged nanoparticles. That caused twice as many lipids to be pulled away from the membrane surface resulting in thinning and even rupture. Small charged nanoparticles formed micelles while remaining embedded in the membrane. Charged nanoparticles above a certain critical size, in addition to forming micelles, were also found to form pores in the membrane. While the study was done over a narrow range of nanoparticle sizes they assume that the trend of large, highly charged nanoparticles causing pores would continue. I will present the details of their results in chapter 3 as they pertain to my results. Ginzburg and Balijepalli acknowledged that their model only deals with the thermodynamics of the system and that a dynamical model is needed to understand the details of the pore formation such as energy barriers and time scales.

Chapter 3

THERMODYNAMICS OF NANOPARTICLE/LIPID BILAYER INTERACTIONS

Interactions between nanoparticles (NP) and lipid bilayers (LB) can be understood in terms of the membrane properties and the attraction between the NP and LB. In this chapter I will outline a simple continuum model and define the free energies for various NP/LB states. I consider both spherical and rod-shaped NP. By comparing those energies I will make a phase diagram to identify when NP become wrapped and when pore formation becomes favorable. I will then compare my phase diagram with the DFT results of Ginzburg and Balijepalli [65]. As I mentioned in section 2.5.1, I have chosen to compare with their work because they have also proposed a phase diagram. Finally, I will present MD simulations I have run which I will compare with my predicted phase diagram.

3.1 Continuum Model Theory

The energy of a membrane can be characterized in terms of large scale deformations like bending and stretching. In this section I will present the energies for various NP/LB states. All energies are defined with respect to an initial reference state in which the NP and LB are separated. I will first define the energies and then compare them in order to make a phase diagram.

The choice of ensemble is an important factor in determining the wrapping behavior. In the case of an isolated cell or vesicle interacting with small NP, a fixed area ensemble may be appropriate. While there can be significant deformation of the membrane near the NP, the large scale dimensions of the LB remain relatively unchanged. This assumes that there are insufficient free lipids to be added to the LB or that the process occurs much more slowly than the NP wrapping. This means that wrapping will increase tension in the LB and that exceeding a critical tension could rupture the LB. I calculate free energies for the various states in this ensemble and later present corresponding fixed boundary MD simulations.

Alternatively, it may be more appropriate to fix the lateral tension of the LB. Cells are able to regulate a small but nonzero tension by adding or removing lipids. While wrapping is still possible, stable pore formation is impossible under low tension. One could imagine a very large or highly charged NP causing severe stretching and inhibiting the cell's tension regulation. That would cause a spike in tension and temporary pore formation. Ruiz-Herrero et al. observed such transient pores in their simulations [63]. One must be very careful in defining the barostat in MD simulations. The barostat controls how quickly the pressure can relax and can therefore be responsible for pressure/tension spikes.

In this section I will consider a fixed area and fixed tension LB interacting with a spherical NP. I will also discuss the infinite rod NP case as it appears to be similar to a 2D system.

3.1.1 Fixed boundary LB with spherical NP

Here I list the possible states for a spherical NP interacting with a LB with fixed boundaries. I first consider hydrophilic NP meaning that the NP will adhere to the lipid heads, opposed to the tails. I will separately consider hydrophobic NP which prefer to be in contact with the lipid tails. For each state I define the free energy with respect to the reference state in which the NP and LB are dissociated. Figures 3.1 and 3.2 show schematics for each of the states along with their free energies.

Figure 3.1:

Hydrophilic spherical NP states

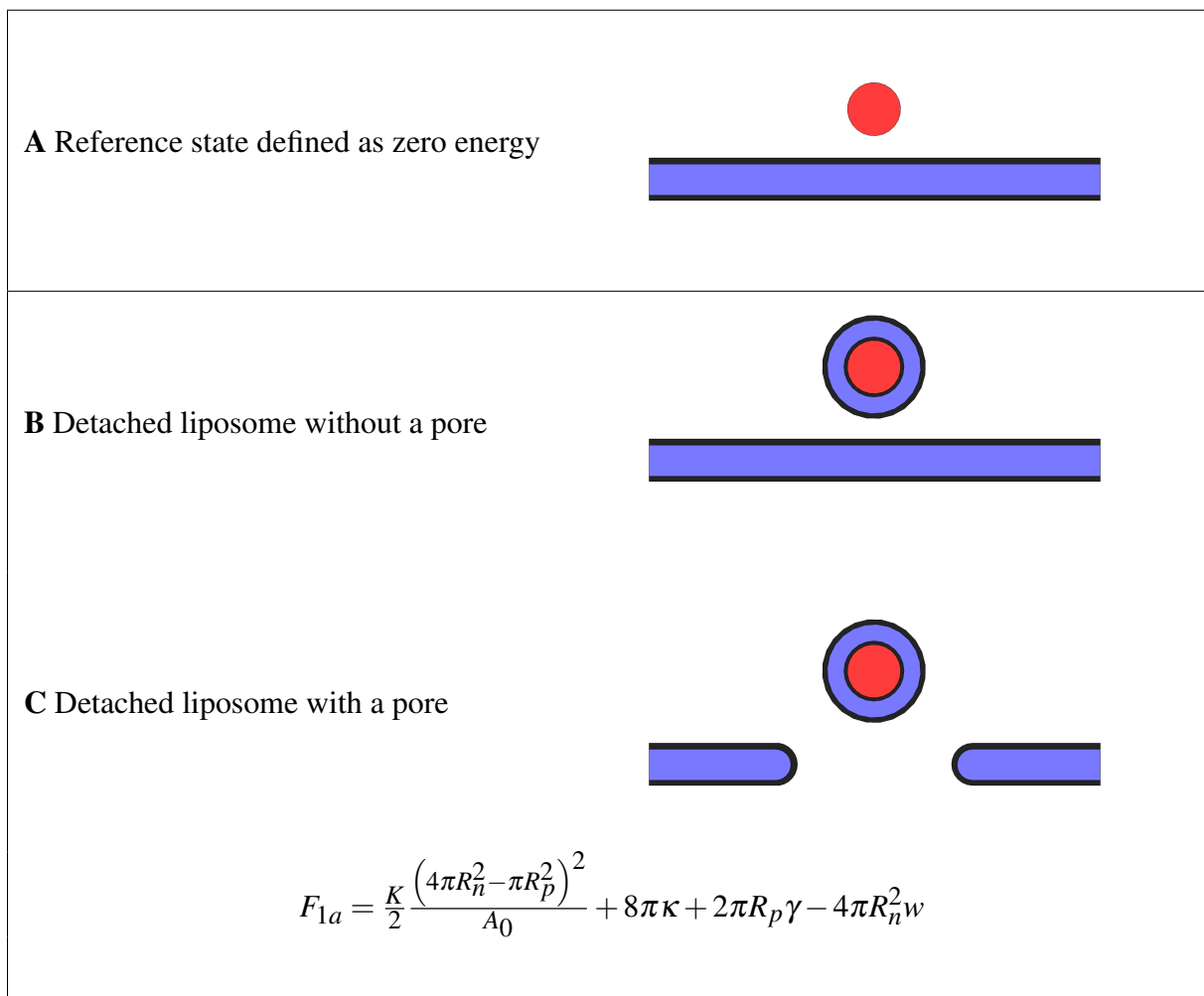
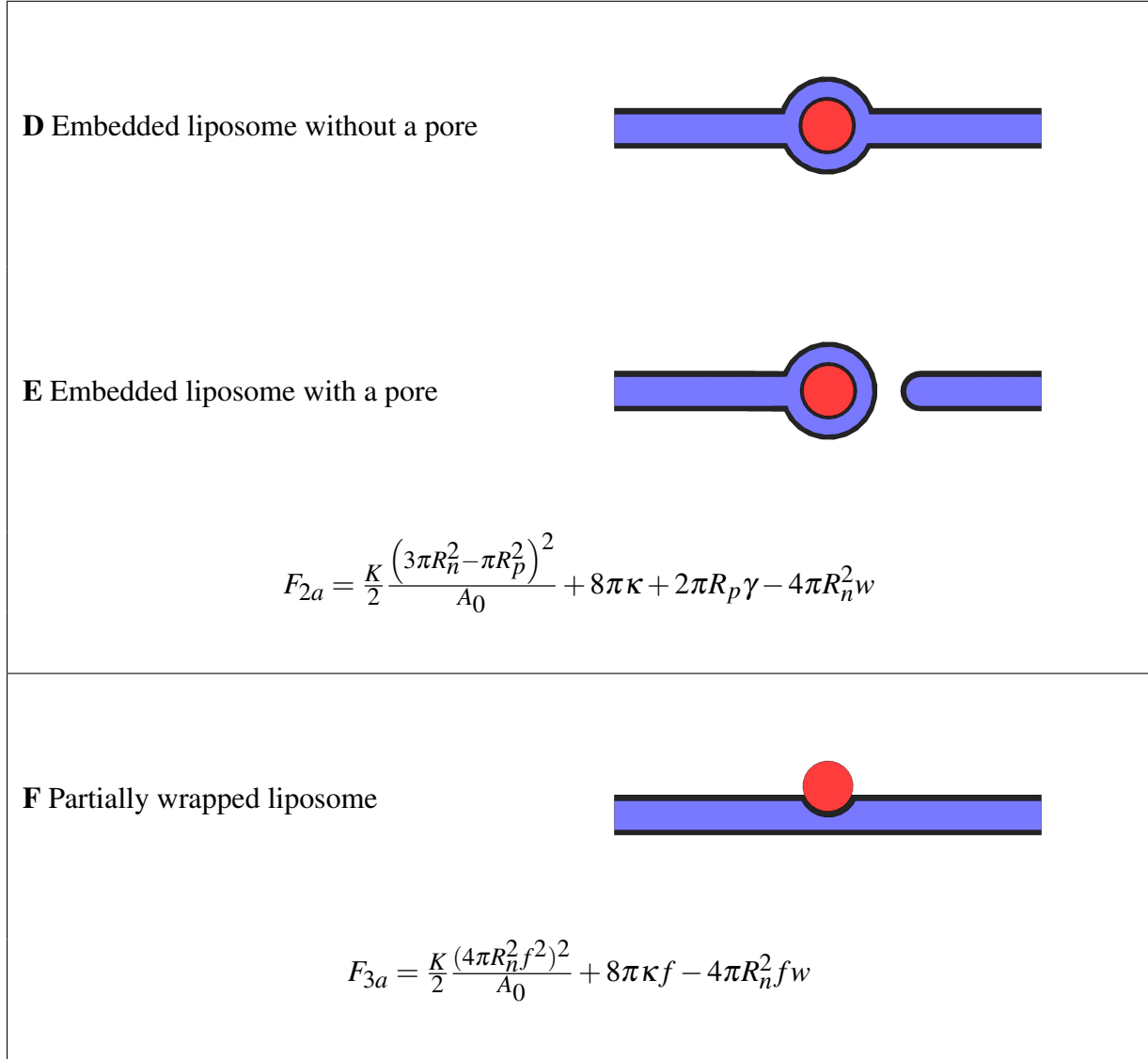


Figure 3.1 (cont'd)



3.1.1.1 Detached liposome (sphere)

The first nonzero energy state involves the nanoparticle being completely wrapped and detached from the bilayer. I call this state “detached”. Its energy is

$$F_{1a} = \frac{K}{2} \frac{(4\pi R_n^2 - \pi R_p^2)^2}{A_0} + 8\pi\kappa + 2\pi R_p \gamma - 4\pi R_n^2 w \quad (3.1)$$

The first term is the stretching energy of the bilayer. This is an harmonic approximation appropriate for relatively small changes to the membrane area [34, 72, 37, 40]. K is the stretching

modulus and R_n is the radius of the NP. A_0 is the starting unstretched area of the bilayer and is a constant in this ensemble. The squared term in parentheses is the change in area, in this case the surface area of the NP minus the area of a possible pore of radius R_p .

The second term is the bending energy of the bilayer around the nanoparticle and is independent of the nanoparticle size in the case of total spherical coverage [56]. κ is the bending modulus of the LB. The third term is the line energy around the edge of the pore. The cost comes from lipid heads having to curve around the edge of the pore to protect the hydrophobic tails. The constant, γ , is a material property and is directly proportional to K . In section 3.2 I will calculate values for K , A_0 , κ , and γ based on my own MD simulations.

The last term is the adhesion energy proportional to the nanoparticle's surface area and is the only favorable term. The constant, w , is a parameter in my simulations on the order of $20 \epsilon/\sigma^2$. While I treat w as a constant, it should depend on the lipid concentration in contact with the NP. A weakly attractive NP will allow thinning of the LB and result in less adhesion energy. On the other hand, a strongly attractive NP could cause a tight aggregation of lipids in contact with it and result in a higher adhesion energy. Assuming a constant w is reasonable for small changes in lipid concentration. This issue will come up again later when analyzing my phase diagram.

This energy applies to states B and C in figure 3.1 depending on whether or not there is a pore.

3.1.1.2 Embedded liposome (sphere)

The second state consists of a completely covered nanoparticle which is embedded in the bilayer. The energy is

$$F_{2a} = \frac{K}{2} \frac{(3\pi R_n^2 - \pi R_p^2)^2}{A_0} + 8\pi\kappa + 2\pi R_p\gamma - 4\pi R_n^2 w \quad (3.2)$$

and corresponds to states D and E in figure 3.1 depending on whether or not there is a pore. The change in area in the first term is the surface area of the NP minus the cross sectional area of the NP displacing the membrane as well as the area of the pore. The only difference from the

detached state is a reduction in stretching energy. For that reason, the embedded states will always be more favorable.

Equation (3.2) assumes that the pore is physically separated from the embedded liposome. It is possible and in some cases preferable for the pore to be adjacent to the liposome. By sharing an edge, the line energy around the pore can be reduced. This decrease in energy is somewhat mitigated by a decrease in pore area which increases the stretching energy. After calculating the changes to the stretching and line energy terms, I found that the effect on the total energy is negligible.

An additional energy contribution I have neglected is the LB curvature around the interface of the embedded liposome. For small NP, whose size is comparable to the LB thickness, the interface curvature will be negligible. For larger NP, the curvature will increase until the radius of curvature around the interface is similar to that around the edge of a pore. In this large NP limit, an additional line energy term should be included in which γ increases with the NP radius. I believe equation (3.2) is appropriate for describing my simulations which involve small NP.

3.1.1.3 Partially wrapped spherical nanoparticle

Another possible state is the partially wrapped NP given by state F in figure 3.1. If f represents the fraction of the NP covered, its energy is

$$F_{3a} = \frac{K (4\pi R_n^2 f^2)^2}{2 A_0} + 8\pi\kappa f - 4\pi R_n^2 f w \quad (3.3)$$

The bending and adhesion terms are simply proportional to f . This equation assumes that the NP is less than half wrapped ($0 \leq f \leq 1/2$). Further wrapping requires a more complicated form. The stretching term contains the surface area of a spherical cap minus the excluded circular intersection area. The derivative with respect to f must be taken to find the optimal wrapping fraction.

$$\frac{dF_{3a}}{df} = 4\pi \left(\frac{8\pi R_n^4 f^3 K}{A_0} + 2\kappa - R_n^2 w \right) \quad (3.4)$$

Initial wrapping depends on the derivative as f approaches zero. Setting the limit of the derivative as f approaches zero equal to zero gives the following condition.

$$\begin{aligned} \frac{dF_{3a}}{df} \Big|_{f \rightarrow 0} &= 0 \\ \Rightarrow 4\pi R_n^2 w &= 8\pi\kappa \end{aligned} \quad (3.5)$$

The two remaining terms are the adhesion and bending energies. If the adhesion is stronger, then at least partial wrapping will occur. For a given value of w a critical nanoparticle radius can be found.

$$R_{n1} = \sqrt{\frac{2\kappa}{w}} \quad (3.6)$$

The condition for at least a metastable half wrapped state can be found by taking the limit of the derivative as f approaches 1/2.

$$\begin{aligned} \frac{dF_{3a}}{df} \Big|_{f \rightarrow 1/2} &= 0 \\ \Rightarrow 4\pi R_n^2 w &= 8\pi\kappa + K \frac{(2\pi R_n^2)^2}{A_0} \end{aligned} \quad (3.7)$$

In this case the adhesion not only has to overcome the cost of bending but also some stretching. Again, assuming a constant w , the critical minimum radius would be

$$R_{n2} = \sqrt{\frac{A_0}{2\pi K} \left(w - \sqrt{w^2 - \frac{8\pi\kappa K}{A_0}} \right)} \quad (3.8)$$

In order to see if total wrapping is favorable, let's compare the half wrapped state and the embedded state with no pore

$$F_{2a}|_{R_p \rightarrow 0} - F_{3a}|_{f \rightarrow 1/2} = 2\pi \left(\frac{2\pi R_n^4 K}{A_0} + 2\kappa - R_n^2 w \right) \quad (3.9)$$

The condition for complete wrapping can be determined by finding when equation (3.9) is negative. There are two positive roots indicating a range over which complete wrapping is favorable.

$$\frac{1}{\sqrt{\pi K}} \sqrt{1 - \sqrt{1 - \xi}} < R_n < \frac{1}{\sqrt{\pi K}} \sqrt{1 + \sqrt{1 - \xi}} \quad (3.10)$$

where

$$\xi = \frac{16\pi\kappa K}{A_0 w^2} \quad (3.11)$$

Very small NP can not gain enough through adhesion to pay the cost of bending. Very large NP simply require too much stretching.

3.1.1.4 Single layer micelle (sphere) states

The previous sections assumed a hydrophilic NP in contact with lipid heads and wrapped with a bilayer. If instead, the NP is hydrophobic or attracted more to the lipid tails, then it will prefer to be wrapped by a single layer and the energies will be slightly different. Again I consider the embedded and detached states with and without pores. First, the detached states, corresponding to states G and H in figure 3.2 will have an energy similar to F_{1a} ,

$$F_{4a} = \frac{K}{2} \frac{\left(2\pi R_n^2 - \pi R_p^2\right)^2}{A_0} + 4\pi\kappa + 2\pi R_p \gamma - 4\pi R_n^2 \nu \quad (3.12)$$

The bending and stretching terms are smaller because only a single layer of lipids is being deformed. The adhesion term has a new constant, ν , corresponding to the NP/tail interaction. There is an increase in energy from the separation of monolayers around the nanoparticle. Since that is also proportional to the surface area of the nanoparticle I have combined that effect with the nanoparticle adhesion by lowering ν appropriately. Although ν and the NP/head attraction strength,

w , can be independent, what matters is their relative magnitudes. In later sections I will treat v as a constant while allowing w to vary.

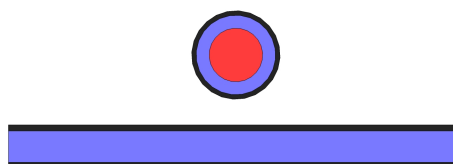
The embedded states corresponding to states I and J in figure 3.2 will be similar to F_{2a} ,

$$F_{5a} = \frac{K}{2} \frac{(\pi R_n^2 - \pi R_p^2)^2}{A_0} + 4\pi\kappa + 2\pi R_p \gamma - 4\pi R_n^2 v \quad (3.13)$$

Figure 3.2:

Hydrophobic spherical NP states

G Detached micelle without a pore

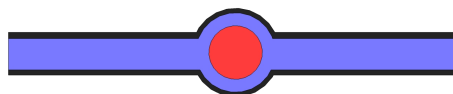


H Detached micelle with a pore

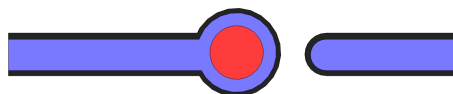


$$F_{4a} = \frac{\kappa}{2} \frac{(2\pi R_n^2 - \pi R_p^2)^2}{A_0} + 4\pi\kappa + 2\pi R_p\gamma - 4\pi R_n^2 v$$

I Embedded micelle without a pore



J Embedded micelle with a pore



$$F_{5a} = \frac{\kappa}{2} \frac{(\pi R_n^2 - \pi R_p^2)^2}{A_0} + 4\pi\kappa + 2\pi R_p\gamma - 4\pi R_n^2 v$$

3.1.2 Fixed boundary LB with infinite rod

Now I will list the possible states of the same fixed boundary LB, instead interacting with an infinite rod. Schematics of the side views of these states, looking down the length of the rod, are the same as those for spherical NP. The energies are listed in figures 3.3 and 3.4. The subscripts, “*b*” and “*c*”, denote the rod states opposed to the “*a*” previously used for the spherical NP. I will still use R_n to now represent the radius of the rod. Additionally, I define the length of the rod as L . By infinite rod, I mean that it spans the length of my simulation box which has periodic boundaries. The area of the unstretched LB is therefore L^2 .

Figure 3.3:

Hydrophilic rod-shaped NP states

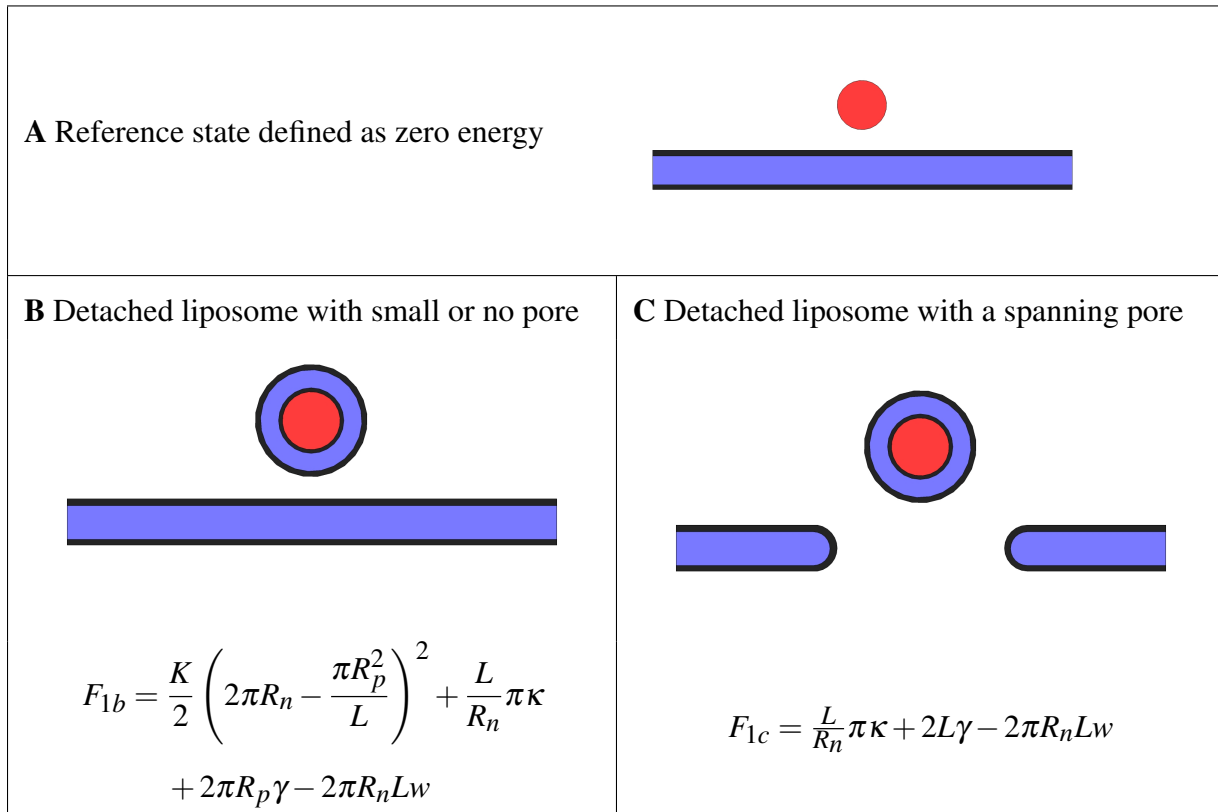
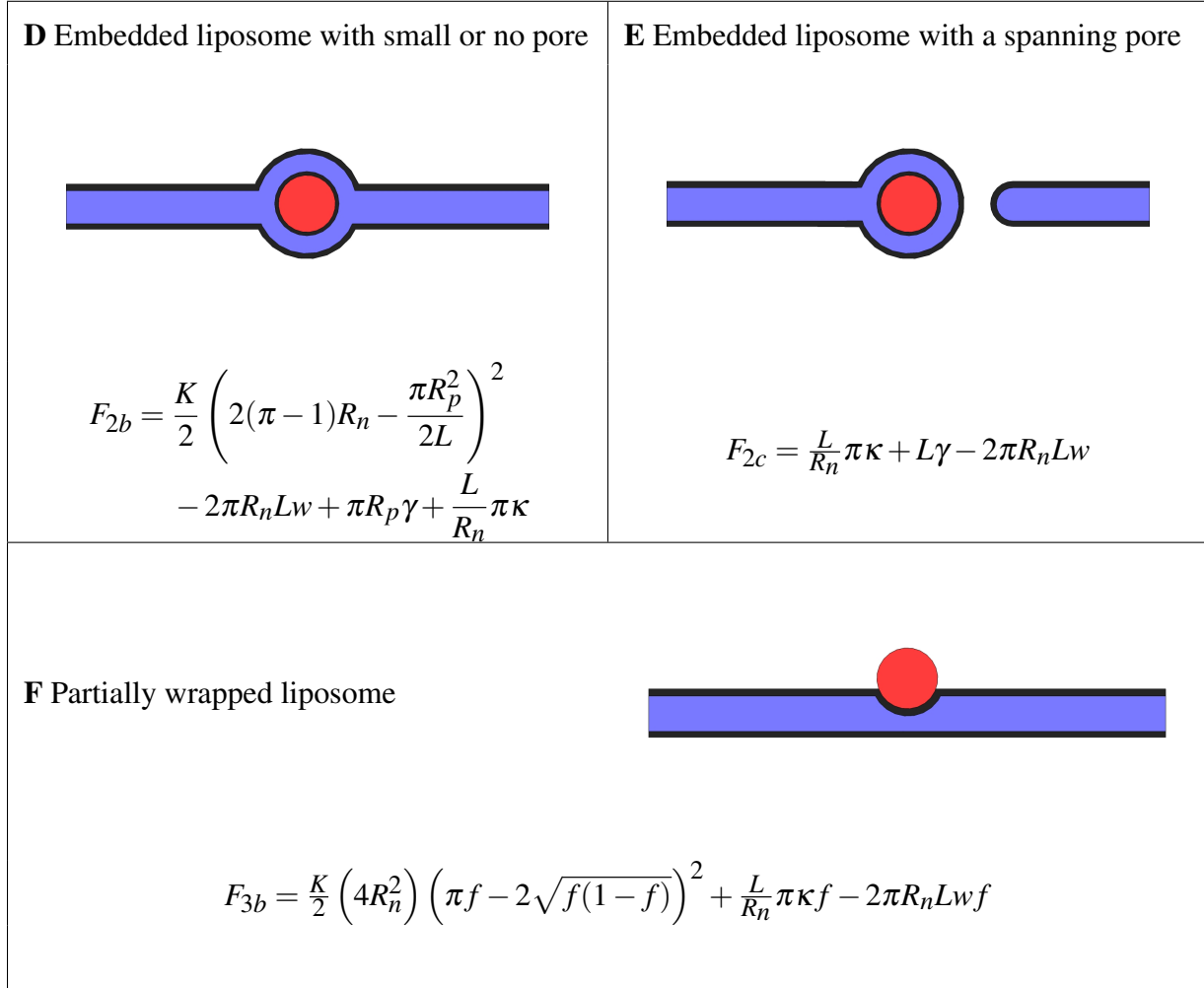


Figure 3.3 (cont'd)



3.1.2.1 Detached liposome (rod)

The detached states (B and C in figure 3.3) again consist of a completely wrapped NP (this time rod-shaped) and a LB which may have a pore.

In the spherical NP cases, we assumed that the pore area which was proportional to the NP area was much smaller than the area of the LB. In the infinite rod case, the length of the rod is comparable (in our case equal) to the length of the LB. It is therefore possible for a pore to span the entire length of the membrane. I separately consider the cases of small pores and pores that span the entire length of the LB. The energy for a detached liposome state with a small round pore is

$$F_{1b} = \frac{K}{2} \left(2\pi R_n - \frac{\pi R_p^2}{L} \right)^2 + \frac{L}{R_n} \pi \kappa + 2\pi R_p \gamma - 2\pi R_n L w \quad (3.14)$$

The area term now contains the surface area of the rod as well as the pore area. Both terms in parentheses are divided by L because of the division by the LB area. The bending term is now size dependent because the curvature is still $1/R_n$ while the rod's surface area is $2\pi R_n L$. Integrating the curvature then gives

$$\begin{aligned} E_b &= \int dA \left\{ \frac{\kappa}{2} \left(\frac{1}{R_n} \right)^2 \right\} = \frac{\kappa}{2} \left(\frac{2\pi R_n L}{R_n^2} \right) \\ &= \frac{L}{R_n} \pi \kappa \end{aligned} \quad (3.15)$$

The line energy term remains the same while the adhesion term is again proportional to the rod's surface area. Equation (3.14) also describes the state without a pore if R_p is equal to zero.

In the case of a large spanning pore, the LB is free to retract and relieve all of the stretching energy. The free energy of the spanning pore state is

$$F_{1c} = \frac{L}{R_n} \pi \kappa + 2L\gamma - 2\pi R_n L w \quad (3.16)$$

Besides the absence of stretching energy, the only other difference is that the line energy is proportional to $2L$ because there are two edges equal to the length of the LB.

3.1.2.2 Embedded liposome (rod)

The embedded states (D and E in figure 3.3) can also have either a small or spanning pore. The energy of the small pore state is

$$F_{2b} = \frac{K}{2} \left(2(\pi - 1)R_n - \frac{\pi R_p^2}{2L} \right)^2 - 2\pi R_n L w + \pi R_p \gamma + \frac{L}{R_n} \pi \kappa \quad (3.17)$$

The change in area is equal to the surface area of the rod ($2\pi R_n L$) minus the displaced area ($2R_n L$) and the pore area. The most energy efficient pore shape is a half circle adjacent to the

liposome. It allows a smaller line energy for a given pore area. That is why the line energy is proportional to πR_p . The bending and adhesion terms remain the same.

The energy for the spanning pore case is

$$F_{2c} = \frac{L}{R_n} \pi \kappa + L\gamma - 2\pi R_n Lw \quad (3.18)$$

The line energy is half of that in equation (3.16) because there is only one edge.

3.1.2.3 Partially wrapped rod-shaped nanoparticle

The partially wrapped rod-shaped nanoparticle has an energy of

$$F_{3b} = \frac{K}{2} \left(4R_n^2 \right) \left(\pi f - 2\sqrt{f(1-f)} \right)^2 + \frac{L}{R_n} \pi \kappa f - 2\pi R_n Lw f \quad (3.19)$$

The area term contains the surface area of the LB in contact with the NP minus the displaced area. The bending and adhesion terms are the same as in states B-E except that they are proportional to the wrapping fraction, f .

As in the spherical NP case we can find the condition for wrapping by taking the derivative with respect to f

$$\frac{dF_{3b}}{df} = 4K \left(\pi - \frac{1-2f}{f(1-f)} \right) (f\pi - 2\sqrt{f(1-f)}) R_n^2 + L \left(\frac{\pi \kappa}{R_n} - 2\pi R_n w \right) \quad (3.20)$$

Since I am assuming an *infinite* rod ($L \gg R_n$), only the terms proportional to L are significant. Therefore the derivative is negative and wrapping is favorable if

$$R_n > \sqrt{\frac{\kappa}{2w}} \quad (3.21)$$

Notice that this condition is independent of f meaning that total wrapping will occur for rods above the critical radius. For a finite rod, there is a stable partially wrapped state which I'll describe in section 3.3.2.

3.1.2.4 Single layer micelle (rod) states

Similar to the spherical hydrophobic NP states, I will now list the states in which the rod prefers to be in contact with lipid tails and is therefore wrapped by a single layer of lipids, forming a micelle. I begin with the detached rod-shaped micelle state with a small pore (G in figure 3.4). The energy is given by

$$F_{4b} = \frac{K}{2} \left(\pi R_n - \frac{\pi R_p^2}{L} \right)^2 + \pi \kappa \frac{L}{2R_n} + 2\pi R_p \gamma - 2\pi R_n L v \quad (3.22)$$

The stretching and bending terms are smaller than in state B (F_{1b}) because it is easier to bend or stretch a single layer of lipids. The energy for a detached micelle with a spanning pore (H in figure 3.4) is

$$F_{4c} = \pi \kappa \frac{L}{2R_n} + 2L\gamma - 2\pi R_n L v \quad (3.23)$$

The bending energy is half of that for state C (F_{1c}). An embedded rod-shaped micelle with a small pore (I in figure 3.4) has an energy of

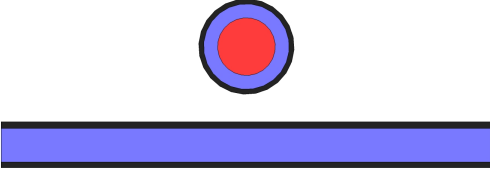
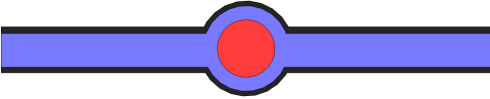
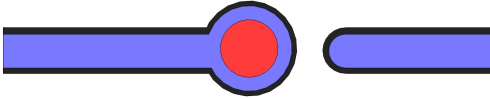
$$F_{5b} = \frac{K}{2} \left((\pi - 2)R_n - \frac{\pi R_p^2}{2L} \right)^2 + \pi \kappa \frac{L}{2R_n} + \pi R_p \gamma - 2\pi R_n L v \quad (3.24)$$

The stretching and bending terms are similarly smaller than in state D (F_{2b}) because of the single layer wrapping. An embedded rod-shaped micelle with a spanning pore (J in figure 3.4) has an energy of

$$F_{5c} = \pi \kappa \frac{L}{2R_n} + L\gamma - 2\pi R_n L v \quad (3.25)$$

Figure 3.4:

Hydrophobic rod-shaped NP states

<p>G Detached micelle with small or no pore</p>  $F_{4b} = \frac{K}{2} \left(\pi R_n - \frac{\pi R_p^2}{L} \right)^2 + \pi \kappa \frac{L}{2R_n} + 2\pi R_p \gamma - 2\pi R_n L \nu$	<p>H Detached micelle with a spanning pore</p>  $F_{4c} = \pi \kappa \frac{L}{2R_n} + 2L\gamma - 2\pi R_n L \nu$
<p>I Embedded micelle with small or no pore</p>  $F_{5b} = \frac{K}{2} \left((\pi - 2)R_n - \frac{\pi R_p^2}{2L} \right)^2 + \pi \kappa \frac{L}{2R_n} + \pi R_p \gamma - 2\pi R_n L \nu$	<p>J Embedded micelle with a spanning pore</p>  $F_{5c} = \pi \kappa \frac{L}{2R_n} + L\gamma - 2\pi R_n L \nu$

3.1.3 Fixed tension ensemble

If the tension of the LB is held constant then it becomes impossible for a stable pore to exist. The only benefit of a pore is to relieve tension. If the LB is kept at zero tension then any pore will heal

itself to avoid the unfavorable line energy around the edge of the pore. If the LB is under positive tension, then there will be competition between tension relief and line energy.

As an example, let us consider the detached spherical liposome state. The only change from F_{1a} (equation 3.1) is in the stretching term. Under constant tension this term is simply equal to the tension, Σ , times the change in area with respect to the reference state.

$$F_{1d} = \Sigma(4\pi R_n^2 - \pi R_p^2) + 8\pi\kappa + 2\pi R_p\gamma - 4\pi R_n^2 w \quad (3.26)$$

First let us determine when wrapping is favorable before a pore forms. For that we need to find when the energy is negative.

$$F_{1d}(R_p = 0) = \pi(4R_n^2(\Sigma - w) + 8\kappa) \leq 0$$

$$\Rightarrow R_{nc} \geq \sqrt{\frac{2\kappa}{w - \Sigma}} \quad (3.27)$$

A minimum requirement for wrapping is that the benefit from adhesion outweighs the cost of stretching ($w > \Sigma$). Additionally, the nanoparticle must be larger than the critical size in equation (3.27) in order to overcome the cost of bending which dominates for small nanoparticles. Ruiz-Herrero et al. performed simulations at zero tension and found the same condition for wrapping [63].

To see the dependence of pore size on the energy we can differentiate with respect to R_p

$$\frac{dF_{1d}}{dR_p} = 2\pi(\gamma - \Sigma R_p) \quad (3.28)$$

The slope is initially positive meaning that there is a barrier to pore formation. The derivative becomes negative for pores larger than

$$R_{pc} = \gamma/\Sigma \quad (3.29)$$

Any pore larger than this will continue to grow. The size of the energy barrier can be found by comparing the energy at the critical pore radius and the energy for no pore.

$$\begin{aligned} E_{barrier} &= F_{1d}(R_p = \gamma/\Sigma) - F_{1d}(R_p = 0) \\ &= \pi\gamma^2/\Sigma \end{aligned} \quad (3.30)$$

While the critical radii and size of the energy barriers will be different for other states, the general behavior remains the same. Very small NP will not become wrapped and pores will be unstable for any value of Σ . Under positive tension small pores will heal themselves while pores larger than a critical size will grow until the LB tears apart.

3.2 LB properties from simulation

Several LB properties can be determined from simulation. If the LB is slowly stretched biaxially, the surface tension is expected to increase linearly with the area. The critical tension at which a pore forms is related to the line tension around the pore. Cooke and Deserno performed such tests on their LB model [37, 40]. I have run my own simulations using their model to measure these properties. As discussed in section 3.1, the energy of a LB with a pore is

$$E = \frac{K}{2} \frac{(A - A_0 - \pi R_p^2)^2}{A_0} + 2\pi\gamma R_p \quad (3.31)$$

Tolpekina et al. [72] used the following relation between the membrane free energy and surface tension in the canonical ensemble

$$\left(\frac{dE}{dL_{\parallel}} \right)_{N,V,T} = L_{\perp} L_{\parallel} (2p_{zz} - p_{xx} - p_{yy}) = 2L_{\parallel} \Sigma \quad (3.32)$$

where L_{\parallel} and L_{\perp} are the simulation box dimensions parallel and perpendicular to the membrane. p_{ij} represent the pressure tensor components. The right-hand side serves as the definition of the surface tension, Σ . The area of the LB, A_0 , is equal to $(L_{\parallel})^2$. Differentiating equation (3.31) gives

$$\left(\frac{dE}{dL_{\parallel}}\right)_{N,V,T} = 2L_{\parallel} \frac{K}{A_0} (A - A_0 - A_p)$$

$$\Rightarrow \Sigma = \frac{K}{A_0} (A - A_0 - A_p) \quad (3.33)$$

The optimal pore size occurs when the derivative with respect to R_p is zero.

$$\frac{dE}{dR_p} = 2\pi \left[\gamma - \frac{KR_p}{A_0} (A - A_0 - \pi R_p^2) \right] = 0 \quad (3.34)$$

Equation (3.34) only has a positive root if its discriminant is positive.

$$\text{Discriminant} \left[\frac{dE}{dR_p} \right] = \frac{4\pi^5 K^2}{A_0^4} (4K^2(A - A_0)^3 - 27\pi\gamma^2 A_0^2) \quad (3.35)$$

At the critical point ($A = A_c$), the discriminant is equal to zero and can be solved for the line energy constant, γ .

$$\gamma = \frac{2K}{3A_0} \sqrt{\frac{(A_c - A_0)^3}{3\pi}} \quad (3.36)$$

Figure 3.5 shows surface tension versus area for my simulations. I measured the tension for both slowly increasing (green) and decreasing (black) areas. Tension was calculated from the pressure components which are easily accessible from the simulation. Although equation (3.33) assumes a constant volume, it is still appropriate if the box is stretched very slowly.

Under low tension, the relation is linear as indicated by equation (3.33). By fitting my data to that equation I was able to determine $K \approx 22 \text{ } \varepsilon/\sigma^2$ and $A_0 \approx 1820 \text{ } \sigma^2$. The hysteresis between the green and black traces is due to the energy barrier for pore formation and is rate dependent. As the rate of area change is decreased, the two traces should converge. The true critical point should lie between the two peaks and depend only on the membrane properties indicated by equation (3.36). By running constant area simulations over a range of areas, I observed the true critical point to be around $1970 \text{ } \sigma^2$, indicated by the red point in figure 3.5. Along with the other previously determined parameters, equation (3.36) gives a value of $\gamma \approx 4.0 \text{ } \varepsilon/\sigma$. The values for K and γ are

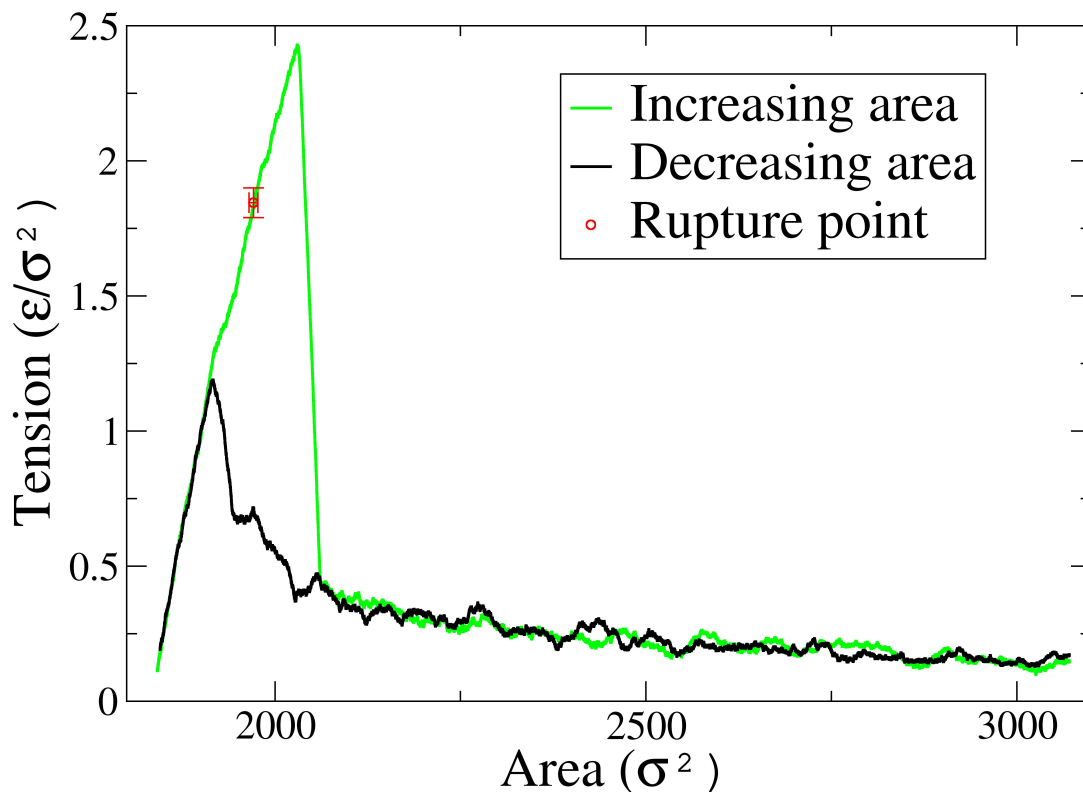


Figure 3.5: Surface tension versus area in a flat LB. The green trace represents increasing area while the black trace represents decreasing area. The red circle indicates the critical point.

in good agreement with those found by Deserno [40]. My values are slightly larger because my simulations were run at a lower temperature.

The bending modulus, κ , can be estimated from thin plate theory as

$$\kappa = \frac{Kh^2}{48(1-\nu^2)} \quad (3.37)$$

where h is the thickness of the membrane and ν is the Poisson ratio measuring compressibility. Assuming a perfectly incompressible membrane, $\nu = 0.5$. A LB thickness of $5 \text{ nm} \approx 5.6 \sigma$, along with my value for K gives a bending modulus of $\kappa \approx 19 \epsilon$. This value is also in good agreement with the bending modulus found by Cooke and Deserno using fluctuation measurements [37]. I

will use these values when calculating phase diagrams in the next section.

3.3 Phase diagram

I will now compare the various states described in section 3.1 to see which are the most favorable for different parameters. I will then create a phase diagram to compare with my simulation results and with those of Ginzburg and Balijepalli [65].

3.3.1 Fixed boundaries with spherical NP

The embedded states will always have a lower energy because the stretching energy is smaller. This is a result of my neglecting the curvature around the embedded liposome or micelle interface. As previously mentioned, a large embedded NP will cause significant bending. In the limiting case where the line energy around the interface is equal to that around the edge of a pore, the detached states clearly become more favorable. In all of my small NP simulations, only embedded states were observed.

My phase diagrams will depend on the properties of the NP, namely the size and strength of attraction. By comparing the energies I will determine the transitions. First I will find the critical NP size required for pore formation. A pore will form in the embedded liposome case when the energies of states D and E are equal. It is useful to define the difference between the energies as

$$\Delta F_{2a} = F_{2a}(R_p) - F_{2a}(R_p = 0) \quad (3.38)$$

$$= \pi R_p \left(\frac{\pi R_p K}{2A_0} (-6R_n^2 + R_p^2) + 2\gamma \right) \quad (3.39)$$

This function is by definition equal to zero at ($R_p = 0$) and increases as R_p increases. The pore state is favorable if the function has a positive root, meaning that it eventually becomes negative for a positive pore radius. The factor of R_p corresponds to the zero at the origin. The zero we are interested in must lie in the cubic function in parentheses. Cubic equations have multiple roots

only if their discriminant is positive. Therefore finding the discriminant of the term in parentheses gives another constraint.

$$\text{Discriminant}[\Delta F_{2a}] = \frac{27\pi^2 K^2}{A_0^4} (2\pi^2 K^2 R_n^6 - A_0^2 \gamma^2) \quad (3.40)$$

Setting the discriminant equal to zero and solving for R_n determines the critical NP radius which transitions from D to E. Nanoparticles larger than this will form an embedded liposome and pore.

$$R_{Ea} = \left(\frac{\gamma A_0}{\sqrt{2\pi K}} \right)^{1/3} \quad (3.41)$$

The same procedure can be used to compare the embedded micelle states with and without pores. Again, I start with the difference between energies

$$\Delta F_{3a} = F_{3a}(R_p) - F_{3a}(R_p = 0) \quad (3.42)$$

$$= \frac{\pi R_p}{2A_0} \left(\pi R_p K (-2R_n^2 + R_p^2) + 4A_0 \gamma \right) \quad (3.43)$$

Taking the discriminant of the cubic factor gives

$$\text{Discriminant}[\Delta F_{5a}] = 256\pi^4 R_n^6 K^4 - 432\pi^2 A_0^2 \gamma^2 K^2 \quad (3.44)$$

The critical NP radius at which an embedded micelle forms a pore, transitioning from I to J, is therefore

$$R_{Ja} = \sqrt{3} \left(\frac{\gamma A_0}{\sqrt{2\pi K}} \right)^{1/3} \quad (3.45)$$

R_{Ea} and R_{Ja} give clear transitions for micelle and liposome pore formation. Now I will find when total wrapping becomes more favorable than the dissociated reference state. Since I am using a single adhesion strength between the NP and tail beads, v , it is easier to find the transition from the dissociated state (A) to the embedded micelle state (I). Setting F_{5a} with no pore equal to zero and solving for R_n gives

$$F_{5a}(R_p = 0) = \pi \left(\frac{\pi R_n^4 K}{2A_0} - 2R_n^2 v + 4\kappa \right) = 0$$

$$\Rightarrow R_{Ia} = 2 \sqrt{\frac{A_0 v}{\pi K} \left(1 - \sqrt{1 - \frac{\pi \kappa K}{2A_0 v^2}} \right)} \quad (3.46)$$

The sizes of the three transition radii are as follows

$$R_{Ia} < R_{Ea} < R_{Ja} \quad (3.47)$$

This defines four regions in each of which there are two possible states. For NP smaller than R_{Ia} the possible states are A and D. For NP between R_{Ia} and R_{Ea} the possible states are D and I. Between R_{Ea} and R_{Ja} the possible states are E and I. For NP larger than R_{Ja} the possible states are E and J. To find the adhesion strength (w) dependence of the transitions we must compare the energies in each region.

The transition from the dissociated reference state (A) to the embedded liposome (D) can be found by setting F_{2a} with no pore equal to zero and solving for w

$$w_{ADa} = \frac{9\pi R_n^2 K}{8A_0} + \frac{2\kappa}{R_n^2} \quad (3.48)$$

There is also a partially wrapped state (F). In section 3.1 I found the minimum NP radius required for partial wrapping. If equation(3.5) is solved instead for w , we find the transition from detached (A) to partially wrapped (F).

$$w_{AFa} = \frac{2\kappa}{R_n^2} \quad (3.49)$$

which is the second term in equation (3.48). Once the adhesion strength reaches w_{ADa} , the fully wrapped, embedded state is favorable. The range of w over which a NP becomes partially wrapped is given by the first term in equation (3.48). The partially wrapped phase becomes larger as the surface area of the NP increases with respect to the LB area. For small NP ($R_n^2 \ll A_0$), the partially wrapped phase is negligible.

The transition from state D to I in the second region can be found by setting F_{2a} equal to F_{5a} and solving for w

$$w_{DIa} = \frac{\pi R_n^2 K}{A_0} + \frac{\kappa}{R_n^2} + v \quad (3.50)$$

To find the remaining two transitions we must first solve for the optimal pore sizes for states E and J. This is done by setting the derivative of F_{2a} with respect to R_p equal to zero and solving for R_p .

$$\begin{aligned} \frac{dF_{2a}}{dR_p} &= 2\pi \left(\frac{\pi R_p K}{A_0} (R_p^2 - 3R_n^2) + \gamma \right) = 0 \\ \Rightarrow R_{p2a} &= R_n \left(\frac{(\sqrt{\alpha_a^2 - 1} - \alpha_a)^{2/3} + 1}{(\sqrt{\alpha_a^2 - 1} - \alpha_a)^{1/3}} \right) \end{aligned} \quad (3.51)$$

where

$$\alpha_a = \frac{A_0 \gamma}{2\pi R_n^3 K} \quad (3.52)$$

The optimal micelle pore radius can be found similarly.

$$\begin{aligned} \frac{dF_{5a}}{dR_p} &= 2\pi \left(\frac{\pi R_p K}{A_0} (R_p^2 - R_n^2) + \gamma \right) = 0 \\ \Rightarrow R_{p5a} &= \frac{R_n}{\sqrt{3}} \left(\frac{(\sqrt{\beta_a^2 - 1} - \beta_a)^{2/3} + 1}{(\sqrt{\beta_a^2 - 1} - \beta_a)^{1/3}} \right) \end{aligned} \quad (3.53)$$

where

$$\beta_a = \frac{3\sqrt{3}A_0\gamma}{2\pi R_n^3 K} \quad (3.54)$$

The transition from state E to I in the third region can be found by setting F_{2a} equal to F_{5a} with no pore and solving for w .

$$F_{2a}(R_p = R_{p2a}) = F_{5a}(R_p = 0)$$

$$\Rightarrow w_{EJa} = \frac{\pi K}{4A_0} \left(4R_n^2 - 3R_{p2a}^2 + \frac{R_{p2a}^4}{2R_n^2} \right) + v + \frac{1}{R_n^2} \left(\frac{R_{p2a}}{2} \gamma + \kappa \right) \quad (3.55)$$

where R_{p2a} is given by equation (3.51). The transition from state E to J in the fourth region can be found by setting F_{2a} equal to F_{5a} with the appropriate pore size substitutions (3.51) and (3.53) and solving for w .

$$F_{2a}(R_p = R_{p2a}) = F_{5a}(R_p = R_{p5a})$$

$$\begin{aligned} \Rightarrow w_{EJa} = & \frac{\pi K}{4A_0} \left(4R_n^2 + \frac{R_{p2a}^4 - R_{p5a}^4}{2R_n^2} + R_{p5a}^2 - 3R_{p2a}^2 \right) \\ & + v + \frac{1}{R_n^2} \left(\frac{R_{p2a} - R_{p5a}}{2} \gamma + \kappa \right) \end{aligned} \quad (3.56)$$

Figure 3.6 shows the phase diagram of w versus R_n with w_{ADa} , w_{AFa} , w_{DIa} , w_{EJa} , and w_{EJa} plotted over their respective regions. The partially wrapped state is present but is narrower than the line thickness of the plot. As mentioned before, the favorable region for partial wrapping is negligible for NP small compared to the LB.

3.3.2 Fixed boundaries with infinite rod NP

Similar to the previous section I will now explain the phase transitions for the case of an infinite rod NP interacting with a LB with fixed boundaries. The energies are given in figures 3.3 and 3.4. The phase diagram looks similar to that of the spherical NP case with a couple differences. The relative sizes of the critical radii depend on the size of the membrane. For that reason I will make one phase diagram for large L and one for smaller L .

Embedded states are always preferable to detached states because there will be less stretching. Again, this is because I have neglected the curvature around the interface of the embedded NP which I believe is appropriate for small NP. We are left with states A, D, E, F, I, and J as possibi-

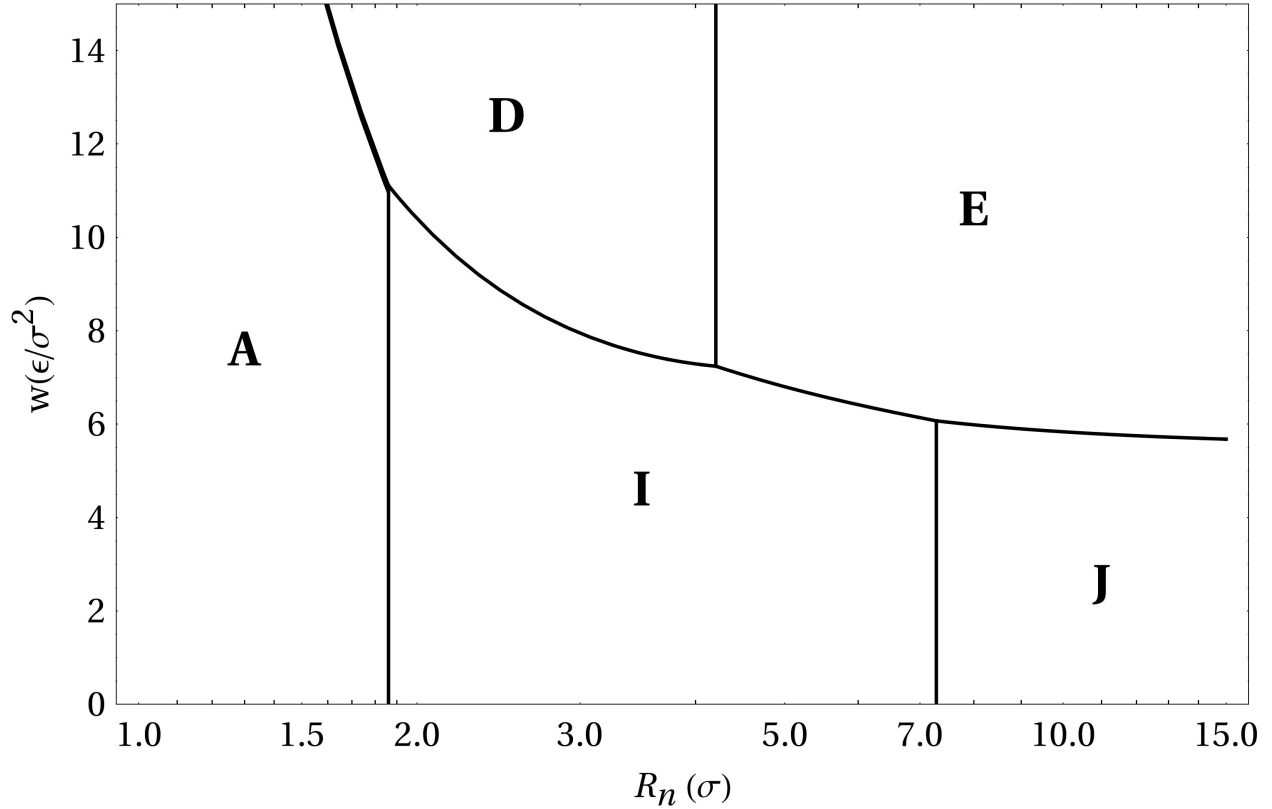


Figure 3.6: Phase diagram of spherical NP states. The x-axis shows the radius of the nanoparticle. The y-axis shows the attraction between the nanoparticle and lipid heads. Attraction increases with w . **(A)** Dissociated reference state, **(D)** Embedded liposome without a pore, **(E)** Embedded liposome with a pore, **(I)** Embedded single-layer micelle without a pore, **(J)** Embedded single-layer micelle with a pore. Schematics and energies for each phase are given in figures 3.1 and 3.2.

ties. To see when a small pore becomes favorable with an embedded liposome we find where F_{2b} is smaller than its value at $R_p = 0$.

$$\Delta F_{2b} = F_{2b} - F_{2b}(R_p = 0) \quad (3.57)$$

$$= \pi R_p \left[\frac{K}{L} \left(\frac{\pi R_p^3}{8L} + (\pi - 1) R_n R_p \right) + \gamma \right] \quad (3.58)$$

This has a positive root if the discriminant of the cubic expression in brackets is positive.

$$\text{Discriminant}[\Delta F_{2b}] = \frac{\pi K^2}{64L^5} \left(32(\pi - 1)^3 R_n^3 K^2 - 27\pi L \gamma^2 \right) \quad (3.59)$$

$$\Rightarrow R_{Db} = \frac{3}{2(\pi - 1)} \left(\frac{\pi L \gamma^2}{4K^2} \right)^{1/3} \quad (3.60)$$

The same procedure can be used to find the critical NP size required to form a small pore in the embedded micelle case.

$$\Delta F_{5b} = F_{5b} - F_{5b}(R_p = 0) \quad (3.61)$$

$$= \pi R_p \left[\gamma - \frac{R_p K}{2L} \left((\pi - 2)R_n - \frac{\pi R_p^2}{4L} \right) \right] \quad (3.62)$$

$$\text{Discriminant}[\Delta F_{5b}] = \frac{\pi K^2}{64L^5} \left(4(\pi - 2)^3 R_n^3 K^2 - 27\pi L \gamma^2 \right) \quad (3.63)$$

$$\Rightarrow R_{Ib1} = \frac{3}{\pi - 2} \left(\frac{\pi L \gamma^2}{4K^2} \right)^{1/3} \quad (3.64)$$

R_{Db} is always smaller than R_{Ib1} . To find the minimum NP radius required to form an embedded micelle with no pore we can set F_{5b} equal to zero (the reference energy) and solve for R_n .

$$F_{5b}(R_p = 0) = \frac{1}{2} \pi^2 R_n^2 K - 2\pi L R_n v + \frac{\pi L \kappa}{2R_n} = 0 \quad (3.65)$$

$$\Rightarrow R_{Ib2} = \frac{1}{4\phi} \sqrt{\frac{\kappa}{v}} \left(\sqrt{3} - \sqrt{3} \cos \left[\frac{1}{3} \cos^{-1} \left[1 - 2\phi^2 \right] \right] \right) \quad (3.66)$$

$$+ 3 \sin \left[\frac{1}{3} \cos^{-1} \left[1 - 2\phi^2 \right] \right] \quad (3.67)$$

where

$$\phi = \frac{3(\pi - 2)^2 K}{16\pi L} \sqrt{\frac{3\kappa}{v^3}} \quad (3.68)$$

These three critical points, R_{Db} , R_{Ib1} , and R_{Ib2} , are again independent of w and will appear as vertical segments in the phase diagram. R_{Ib2} can be either larger or smaller than R_{Ib1} depending on the size of L .

The optimal pore radii in states D and I can be found by seeing when the derivatives of F_{2b} and F_{5b} with respect to R_p are equal to zero. By substituting the optimal pore radius back into F_{2b} and comparing with the energy of the spanning pore state (F_{2c}), we can find the NP transition radius from state D to E, R_{Eb} .

The NP transition radius from state I to J, R_{Jb} , can similarly be found by substituting the optimal pore radius into F_{5b} and setting the energy equal to F_{5c} . R_{Jb} is always larger than both R_{Ib1} and R_{Eb} , but the order of R_{Ib1} and R_{Eb} depends on the size of L .

Now that I have calculated all of the transitions which are strictly radius dependent, I will calculate the transitions which depend on the adhesion constant, w .

3.3.2.1 Small L

For relatively small L , the order of the radial transitions is

$$R_{Db} < R_{Ib2} < R_{Eb} < R_{Ib1} < R_{Jb} \quad (3.69)$$

which defines six regions in which w dependent transitions are required. For NP smaller than R_{Db} , the possible states are A, D, and F. The transition from state A to D can be found by setting F_{2b} with no pore equal to zero and solving for w .

$$\begin{aligned} F_{2b}(R_p = 0) &= 2(\pi - 1)^2 R_n^2 K + \pi L \left(\frac{\kappa}{R_n} - 2R_n w \right) = 0 \\ \Rightarrow w_{ADb1} &= \frac{(\pi - 1)^2 R_n K}{\pi L} + \frac{\kappa}{2R_n^2} \end{aligned} \quad (3.70)$$

As in the spherical case, there is also a stable, partially wrapped state which can be found by finding when the derivative of F_{3b} with respect to f as f approaches zero, is negative.

$$\begin{aligned} \left. \frac{dF_{3b}}{df} \right|_{f \rightarrow 0} &= 8R_n^2 K + \pi L \left(\frac{\kappa}{R_n} - 2R_n w \right) = 0 \\ \Rightarrow w_{AFb} &= \frac{4R_n K}{\pi L} + \frac{\kappa}{2R_n^2} \end{aligned} \quad (3.71)$$

For NP between R_{Db} and R_{Ib2} , the possible states are A and D with a small pore. The transition can be found by substituting the optimal pore radius into F_{2b} and finding where it becomes zero.

$$F_{2b}(R_p = R_{p2b}) = 0$$

$$\Rightarrow w_{ADb2} = \frac{1}{2R_n L} \left[\frac{K}{8\pi L^2} \left(\pi R_{p2b}^2 - 4(\pi - 1)R_n L \right)^2 + R_{p2b} \gamma + \frac{L\kappa}{R_n} \right] \quad (3.72)$$

where R_{p2b} is the optimal small pore radius. For NP between R_{Ib2} and R_{Eb} , the possible states are I without a pore and D with a small pore. The transition can be found by substituting the optimal pore radius into F_{2b} and setting the energy equal to F_{5b} without a pore. Solving for w gives

$$F_{2b}(R_p = R_{p2b}) = F_{5b}(R_p = 0)$$

$$\Rightarrow w_{D2I1b} = \frac{1}{4R_n L} \left[\frac{K}{4L^2} \left(2R_n L - R_{p2b}^2 \right) \left(2(3\pi - 4)R_n L - \pi R_{p2b}^2 \right) + 2R_{p2b} \gamma + L \left(4R_n \nu + \frac{\kappa}{R_n} \right) \right] \quad (3.73)$$

For NP between R_{Eb} and R_{Ib1} , the possible states are I without a pore and E. The transition can be found by setting F_{5b} without a pore equal to F_{2c} and solving for w .

$$F_{2c} = F_{5b}(R_p = 0)$$

$$\Rightarrow w_{EI1b} = \frac{1}{4\pi R_n^2} \left[2R_n (2\pi R_n \nu + \gamma) + \pi \kappa - \frac{(\pi - 2)^2 R_n^3 K}{L} \right] \quad (3.74)$$

For NP between R_{Ib1} and R_{Jb} , the possible states are I with a small pore and E. The transition can be found by setting F_{5b} with its optimal pore radius equal to F_{2c} and solving for w .

$$F_{2c} = F_{5b}(R_p = R_{p5b})$$

$$\Rightarrow w_{EI2b} = \frac{1}{2\pi R_n L} \left[(2\pi R_n \nu + \gamma)L - \pi R_{p5b} \gamma + \frac{\pi L \kappa}{2R_n} - \frac{K}{8L^2} \left(\pi R_{p5b}^2 - 2(\pi - 2)R_n L \right) \right] \quad (3.75)$$

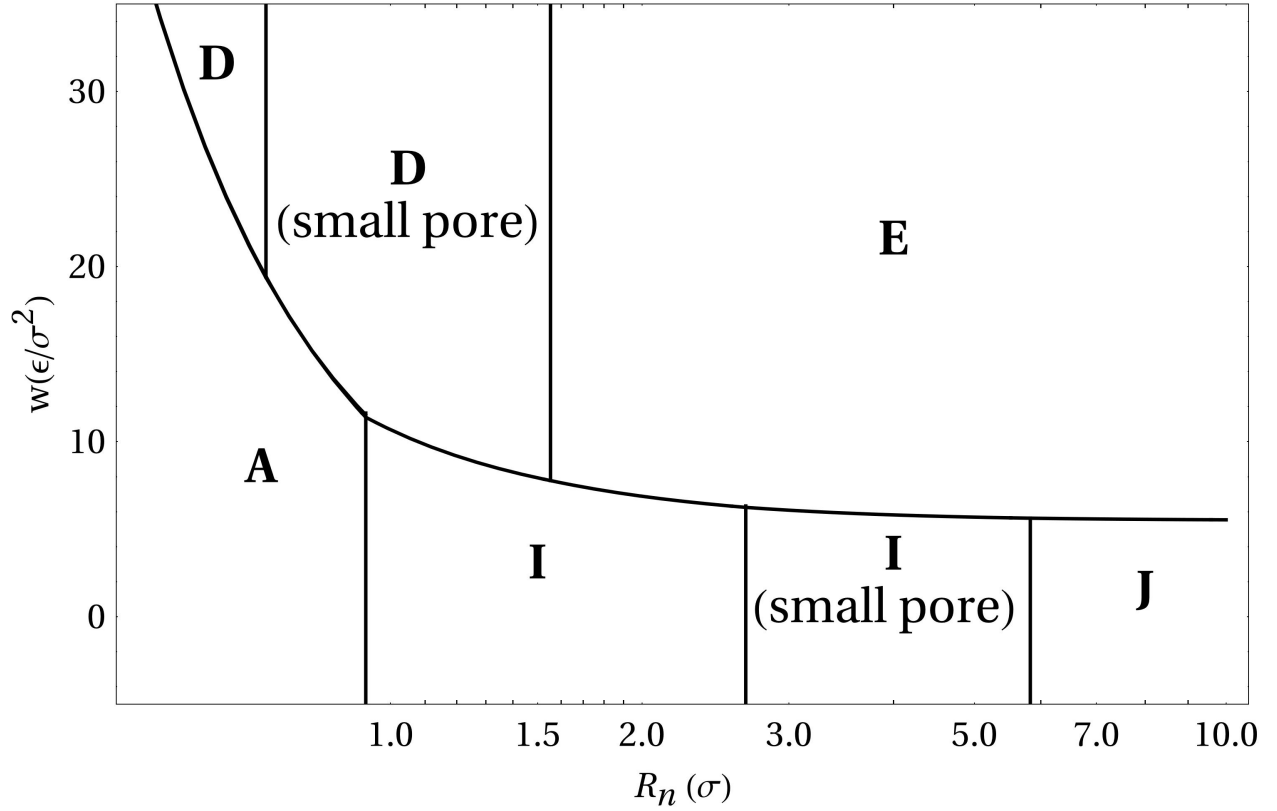


Figure 3.7: Phase diagram of short rod-shaped NP states. The x-axis shows the radius of the nanoparticle. The y-axis shows the attraction between the nanoparticle and lipid heads. Attraction increases with w . (A) Dissociated reference state, (D) Embedded liposome with and without a pore, (E) Embedded liposome with a spanning pore, (I) Embedded single-layer micelle with and without a pore, (J) Embedded single-layer micelle with a spanning pore. Schematics and energies for each phase are given in figures 3.3 and 3.4.

Finally, for NP larger than R_{Jb} , the possible states are E and J. The transition can be found by setting F_{2c} equal to F_{5c} and solving for w .

$$\begin{aligned}
 F_{2c} &= F_{5c} \\
 \Rightarrow w_{EJb} &= \frac{\kappa}{4R_n^2} + v
 \end{aligned} \tag{3.76}$$

Figure 3.7 shows the w vs. R_n phase diagram for $L = 40\sigma$. The partially wrapped state between A and D is narrower than the line width.

3.3.2.2 Large L

For larger L , the order of the radial transitions becomes

$$R_{Ib2} < R_{Db} < R_{Ib1} < R_{Eb} < R_{Jb} \quad (3.77)$$

This introduces two new transitions. For NP between R_{Ib2} and R_{Db} , the possible states are D without a pore and I without a pore. The transition can be found by setting F_{2b} equal to F_{5b} and solving for w .

$$\begin{aligned} F_{2b}(R_p = 0) &= F_{5b}(R_p = 0) \\ \Rightarrow w_{D1I1b} &= \frac{(3\pi - 4)R_n K}{4L} + \frac{\kappa}{4R_n^2} + \nu \end{aligned} \quad (3.78)$$

For NP between R_{Ib1} and R_{Eb} , the possible states are D and I, each with a small pore. The transition can be found by substituting the optimal pore radii into F_{2b} and F_{5b} and finding when they are equal.

$$\begin{aligned} F_{2b}(R_p = R_{p2b}) &= F_{5b}(R_p = R_{p5b}) \\ \Rightarrow w_{D2I2b} &= \frac{1}{4R_n L} \left[\frac{K}{L^2} \left(R_{p2b}^2 - R_{p5b}^2 - 2R_n L \right) \left(8R_n L + \pi \left(R_{p2b}^2 + R_{p5b}^2 - 6R_n L \right) \right) \right. \\ &\quad \left. + 2 \left(R_{p2b} - R_{p5b} \right) \gamma + L \left(4R_n \nu + \frac{\kappa}{R_n} \right) \right] \end{aligned} \quad (3.79)$$

where R_{p2b} and R_{p5b} are the optimal small pore radii for the embedded doubly and singly wrapped states respectively. Figure 3.8 shows the w vs. R_n phase diagram for a much longer rod ($L = 1000\sigma$).

3.4 Comparison with Ginzburg and Balijepalli

I will now see how well my phase diagram agrees with the DFT results of Ginzburg and Balijepalli [65]. As explained in section 2.5.1 they calculated the favorable states for NP/LB interactions while

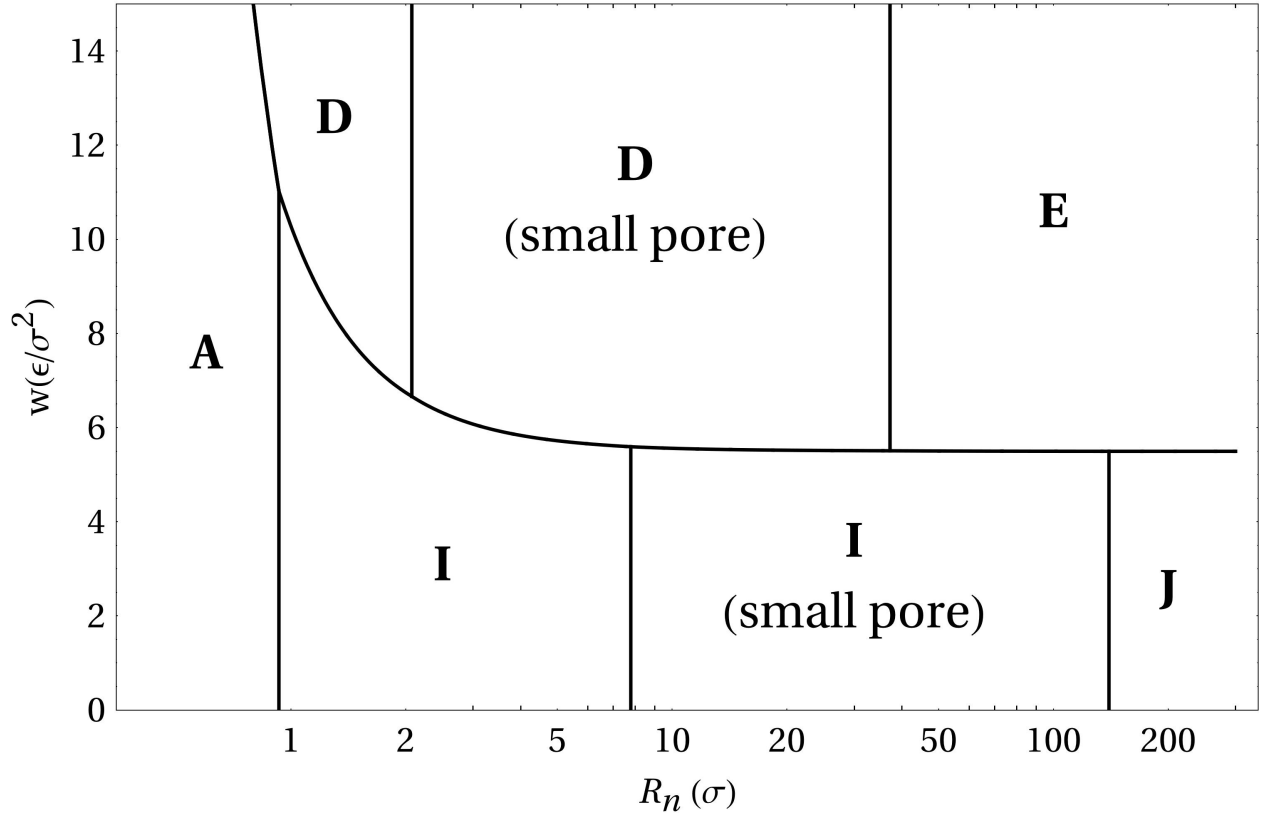


Figure 3.8: Phase diagram of long rod-shaped NP states. The x-axis shows the radius of the nanoparticle. The y-axis shows the attraction between the nanoparticle and lipid heads. Attraction increases with w . (**A**) Dissociated reference state, (**D**) Embedded liposome with and without a pore, (**E**) Embedded liposome with a spanning pore, (**I**) Embedded single-layer micelle with and without a pore, (**J**) Embedded single-layer micelle with a spanning pore. Schematics and energies for each phase are given in figures 3.3 and 3.4.

varying the size and charge density of the NP. In order to compare with Ginzburg and Balijepalli's results I first need to relate the Florry-Huggins parameter, χ , to the adhesion energy density, w . Let us start with the definition of the Florry-Huggins parameter between two types of material (say A and B).

$$\chi_{AB} = \frac{z}{\tau} \left[w_{AB} - \frac{1}{2}(w_{AA} + w_{BB}) \right] \quad (3.80)$$

where z is the coordination of a particular bead, τ is equal to the Boltzmann constant times the temperature, and w is the interaction energy between two beads. The Florry-Huggins parameter

indicates the energy difference between mixed and unmixed states. The three types of beads I use below are hydrophilic (H), lipophilic (L), and nanoparticle (P), corresponding to the head, tail, and NP beads respectively. The attraction between lipid beads is fixed by the Cooke model, so I will use those constraints to set the energy scale. The hydrophilic-lipophilic Flory-Huggins parameter is given by

$$\chi_{HL} = \frac{z}{\tau} \left[w_{HL} - \frac{1}{2}(w_{HH} + w_{LL}) \right] = 1.0 \quad (3.81)$$

The value on the right hand side of this equation as well as those used in the following equations are the values used by Ginzburg and Balijepalli. The Cooke model sets $w_{HL} = w_{HH} = 0$ and $w_{LL} = -\varepsilon$. This gives us the relation between the energy scales.

$$\frac{z}{\tau} = \frac{2}{\varepsilon} \quad (3.82)$$

Now let us look at the particle-tail interaction.

$$\chi_{PL} = \frac{z}{\tau} \left[w_{PL} - \frac{1}{2}(w_{PP} + w_{LL}) \right] = 0.0 \quad (3.83)$$

While w_{LL} is fixed, we have the freedom to choose $w_{PL} = w_{PP} = -\varepsilon$ to satisfy the relation. Finally, we can determine the nanoparticle-head interaction.

$$\chi_{PH} = \frac{z}{\tau} \left[w_{PH} - \frac{1}{2}(w_{PP} + w_{HH}) \right] \quad (3.84)$$

$$w_{PH} = \frac{\varepsilon}{2}(\chi_{PH} - 1) \quad (3.85)$$

I can now appropriately map Flory-Huggins parameters in Ginzburg and Balijepalli's model to interaction strengths in the Cooke model. Since the Cooke model does not have an explicit solvent, we can safely think of it as having solvent beads with effectively zero interaction strength with all other beads. For the sake of completeness let us look at the Flory-Huggins parameters involving the solvent.

$$\chi_{LW} = \frac{z}{\tau} \left[w_{LW} - \frac{1}{2}(w_{LL} + w_{WW}) \right] = 1.0 \quad (3.86)$$

The new subscript, W , denotes the solvent beads. w_{LW} and w_{WW} are not uniquely determined, but we can choose $w_{LW} = w_{WW} = 0$ to satisfy the relation. Similarly,

$$\chi_{HW} = \frac{z}{\tau} \left[w_{HW} - \frac{1}{2}(w_{HH} + w_{WW}) \right] = 0.0 \quad (3.87)$$

$$\chi_{PW} = \frac{z}{\tau} \left[w_{PW} - \frac{1}{2}(w_{PP} + w_{WW}) \right] = 1.0 \quad (3.88)$$

give $w_{HW} = w_{PW} = 0$.

The only interaction varied by Ginzburg and Balijepalli is χ_{PH} which is related to the NP bead/head bead attraction, w_{PH} . The adhesion energy density referred to in the phase diagrams of the previous section can be calculated by estimating the number of nearest neighbors to be

$$w = 1.89 - 9.51w_{PH} \quad (3.89)$$

Substituting equation (3.85) gives a linear relation between the Flory-Huggins parameter and adhesion energy density.

$$w = 6.6 - 4.8\chi_{PH} \quad (3.90)$$

Ginzburg and Balijepalli varied χ_{PH} from -3 to +1 corresponding to w ranging from 2 to 20. Their NP radii ranged from 1.6 nm to 3.2 nm. Figure 3.9 shows my predicted phase diagram along with Ginzburg and Balijepalli's results. The blue circles indicate an embedded micelle with no pore which corresponds to state I. The red squares indicate an embedded liposome with no pore, corresponding to state D. The green diamonds indicate an embedded liposome state with a pore, corresponding to state E.

One discrepancy between my phase diagram and Ginzburg and Balijepalli's results is the three points in the lower left of figure 3.9. My phase diagram appears to overestimate the wrapping

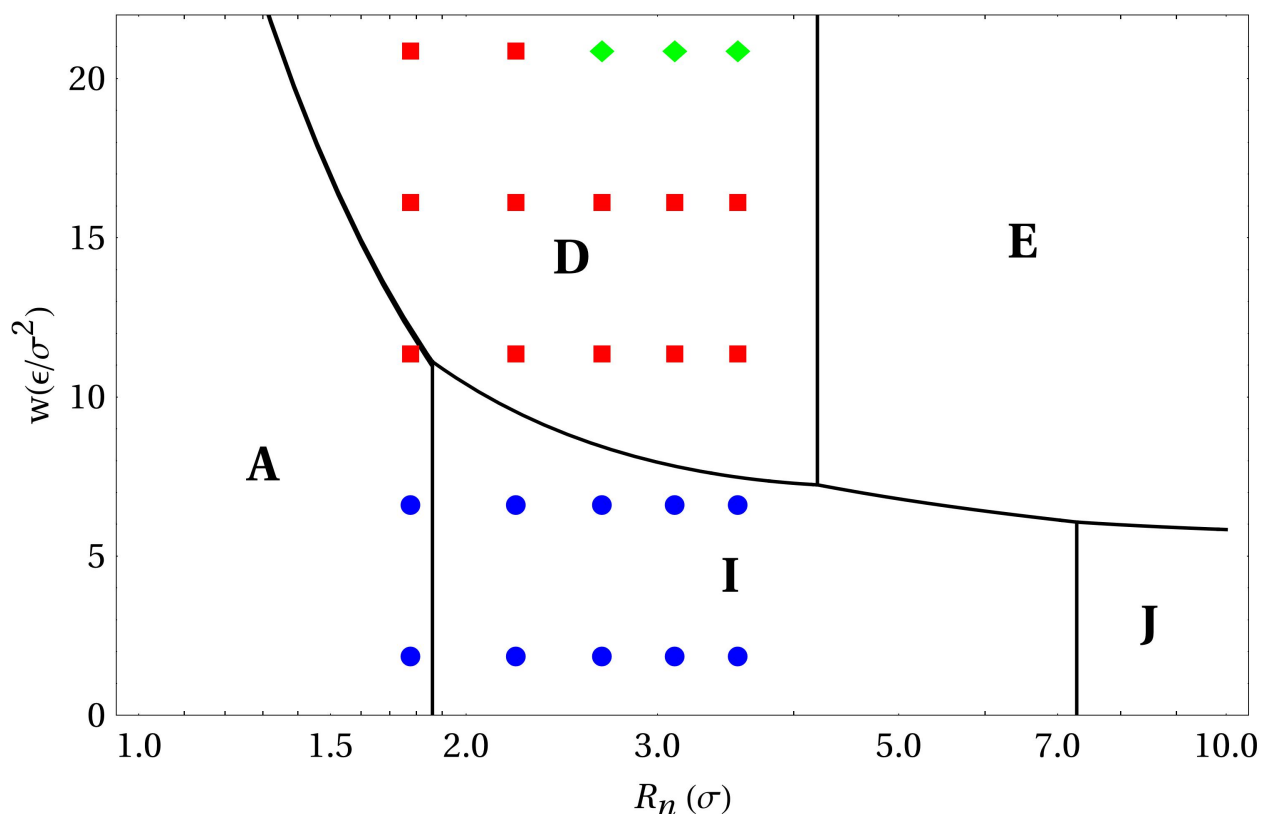


Figure 3.9: Phase diagram of spherical NP states. The x-axis shows the radius of the nanoparticle. The y-axis shows the attraction between the nanoparticle and lipid heads. **(A)** Dissociated reference state, **(D)** Embedded liposome without a pore, **(E)** Embedded liposome with a pore, **(I)** Embedded single-layer micelle without a pore, **(J)** Embedded single-layer micelle with a pore. Schematics and energies for each phase are given in figures (3.1 and 3.2).

Data points indicate the results of Ginzburg and Balijepalli. **(Blue circles)**: Embedded micelles with no pores. **(Red squares)**: Embedded liposomes with no pores. **(Green diamonds)**: Embedded liposomes with pores.

transitions to states D and I. I believe this comes from an overestimate of the bending energy which dominates for small NP wrapping. I assumed bending around a closed spherical surface. However, there is a band around the equator of the NP where it intersects with the LB that should not be counted. This region can be ignored if the NP is much thicker than the LB, but it makes up a significant fraction of the surface area for small NP. Appropriate reduction of the bending energy would lower the wrapping transition.

Another discrepancy in my phase diagram is related to pore formation. My prediction of a

larger critical NP size required for pore formation goes back to my neglect of the curvature around the NP/LB interface. As the NP gets larger that neglected curvature becomes comparable to the curvature around the edge of a pore. By including that curvature cost, the transition from state D to E would occur for slightly smaller NP.

The final discrepancy is that I have predicted the pore transition to be independent of w while Ginzburg and Balijepalli only observed pore formation for strongly attractive NP. I assumed that stretching occurred uniformly throughout the LB with a small uniform decrease in lipid concentration and that the adhesion was independent of stretching. It's true that a weakly attractive NP will cause uniform stretching throughout the LB regardless of whether or not it is in contact with the NP. However, as w increases, lipids will pack more tightly around the NP, increasing the stretching away from the NP. In that way, a strongly attractive NP could increase the stretching above a critical tension, causing a pore. Combining the stretching and adhesion energy terms may fix the discrepancy.

One could argue that a more appropriate comparison with Ginzburg and Balijepalli's results would be with the infinite rod phase diagram shown in figure 3.7. While the predicted transition from singly wrapped micelles to doubly wrapped liposomes is in agreement, there are significant discrepancies with the predicted pore transitions. The spanning pore transition for hydrophilic NP should occur around $R_n = 1.1$ nm according to my predictions compared to the 2.4 nm observed by Ginzburg and Balijepalli. I would also expect a spanning pore transition for hydrophobic NP to occur around $R_n = 2.1$ nm while such a state would presumably exist above 3.2 nm in the Ginzburg and Balijepalli model.

While qualitative comparisons can be made, differences in the models prevent quantitative agreement regarding transition points. Ginzburg and Balijepalli stressed that their results represented only a qualitative view of the dependency of these transitions on NP size and surface treatment. Hydrophobic NP will become singly wrapped while hydrophilic NP will become doubly wrapped. There is also a critical NP size in the nanometer range which causes pore formation. On these general trends, our models are in agreement. A more careful comparison would require de-

termining the the bending and stretching moduli which correspond to the Ginzburg and Balijepalli model.

3.5 Comparison with MD simulations

I have used molecular dynamics to simulate the NP/LB interactions described in the previous sections for both spherical and rod-shaped NP. Interactions were simulated using the Cooke model [36, 37] which was explained in chapter 2. As was previously stated, the Cooke model was chosen for it's ability to handle large systems. For the purpose of comparison, I tried to mimic the same system properties used by Ginzburg and Balijepalli [65]. In this section I will first go over the details of my particular implementation and then I will present my results.

3.5.1 Implementation Details

Simulations were run using LAMMPS (Large-scale Atomic/Molecular Massively Parallel Simulator), which is an open source molecular dynamics package distributed by Sandia National Laboratories. One benefit of using this package is that it can easily be run on parallel systems. My simulations were run on the High Performance Computer Cluster (HPCC) at Michigan State University. The HPCC consists of multiple clusters with both AMD and Intel processors, both dual and quad cores, ranging from 2.2 GHz to 2.4 GHz per core. I used generic submissions to the cluster which used a combination of any available nodes.

Nanoparticles were chosen to have the same radii as those used by Ginzburg and Balijepalli (1.6-3.2 nm) [65]. A square patch of LB containing 3200 lipids was used. The simulation box had fixed periodic boundary conditions with dimensions roughly $40 \times 40 \times 27 \text{ nm}^3$. The horizontal dimensions were initially equilibrated at zero tension before the NP was introduced. The temperature was held constant at $k_B T = 1.0 \epsilon$ using a Nosé-Hoover thermostat [73, 74]. That temperature was shown to be in the liquid phase by Cooke and Deserno [37]. I confirmed this by measuring the projected area as a function of temperature. The phase diagram is shown in figure 3.10. The lighter

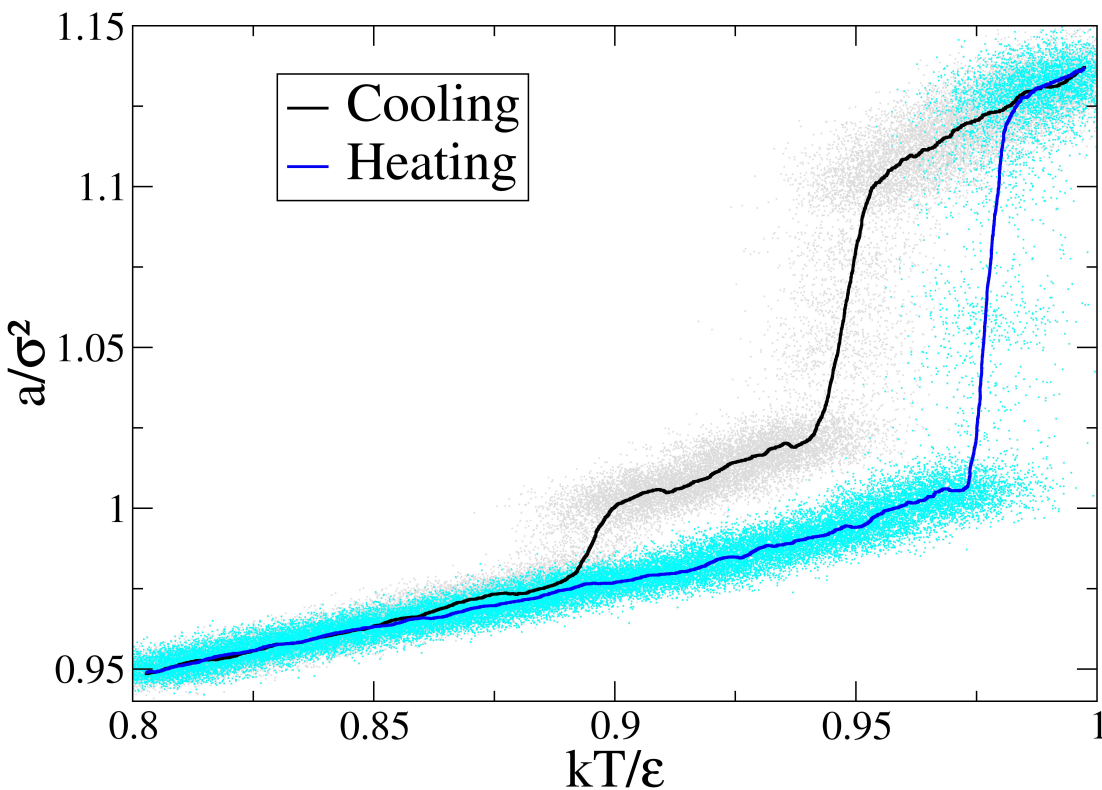


Figure 3.10: Area per lipid versus temperature from Cooke model simulation. The dark lines represent running averages of the raw data which is displayed as lighter dots. In the top trace the temperature is decreasing while in the bottom trace it is increasing. The gel to liquid transition occurs around $k_B T = 0.98 \epsilon$ while heating.

dots indicate the raw data while the dark lines are running averages to clearly show the transition. The top trace represents the cooling transition while the bottom trace represents the heating transition. Cooke and Deserno observed a similar hysteresis. The gel-fluid transition occurs around $k_B T = 0.98 \epsilon$ in the lower trace.

I also looked at the radial distribution function of the bilayer at various temperatures during the heating transition as shown in figure 3.11. It is clear from the disappearance of long range order that the liquid transition occurs between $k_B T = 0.97 \epsilon$ and 0.99ϵ .

The main tunable parameter in the Cooke model is the potential width, w_c , which I set to 1.6σ .

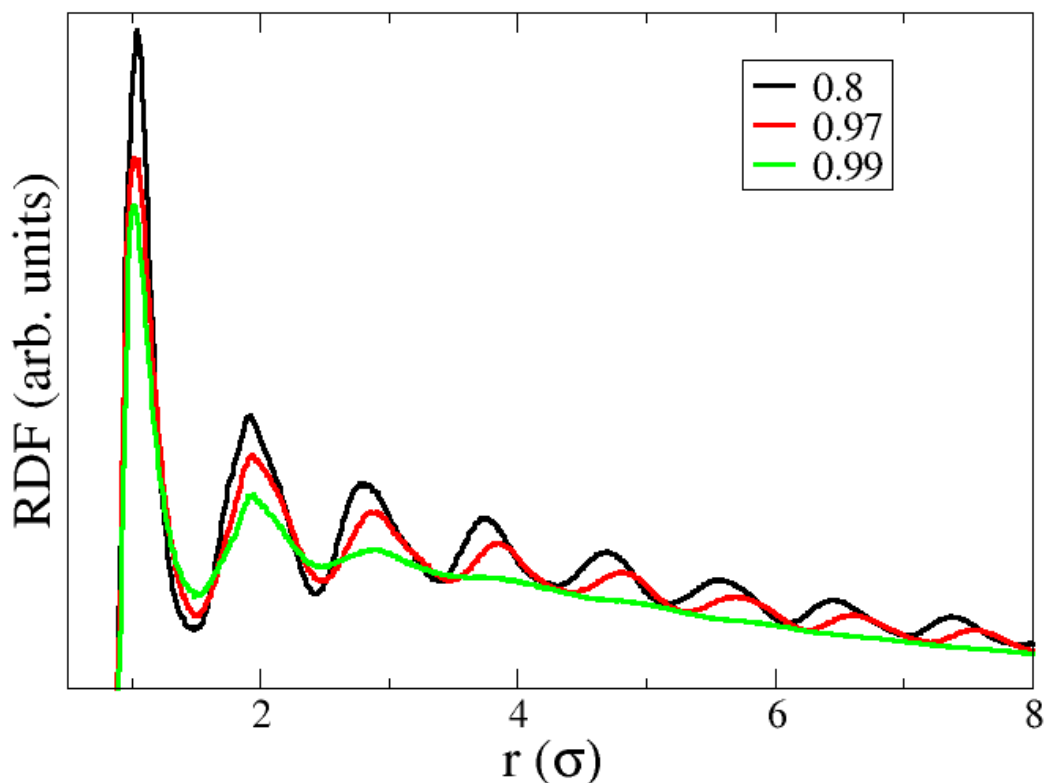


Figure 3.11: Radial distribution function for a lipid bilayer at various temperatures during the heating transition. The lack of long range order in $k_B T = 0.99 \epsilon$ indicates the liquid phase.

That set the overall cutoff distance to $2.6 \sigma \approx 2.3 \text{ nm}$. Nanoparticles consisted of beads which were the same size as the lipid beads (σ), arranged in a spherical cutout of an FCC lattice. The relative positions of the NP beads were held rigid throughout the simulation.

Interactions between NP and lipid beads were also governed by the Cooke potential. Different strengths of the potential were used to correspond to the Flory-Huggins parameters used by Ginzburg and Balijepalli. The relation between the Flory-Huggins parameter and the interaction between individual beads was explained in the previous section.

Simulations were run in the canonical ensemble, keeping the temperature, volume, and number of particles constant, similar to Ginzburg and Balijepalli's work. I used a Nosé-Hoover thermostat

[73, 74] which is explained in appendix 5. A single damping parameter, Q , is used to determine how strongly the system is coupled to the heat bath. It is the effective “mass” associated with the virtual variable s . Great care must be taken to select appropriate Q values [75]. I explain my choice of Q in appendix 5.

I used a time step of 0.01τ which was used by Cooke and Deserno [37]. The bilayer was allowed to equilibrate for $10^4 \tau$ (≈ 93 ns) before introducing the NP. The NP was initially placed at rest about 1 nm from the bilayer. Simulations were run for another $10^4 \tau$ after the NP was introduced. Each simulation ran in parallel on nine cores of the HPCC for approximately one hour. LAMMPS divided the simulation box into a 3x3 grid and calculated interactions in each region on a separate processor.

3.5.2 MD Results

In this section I will describe my simulation results. As explained in the previous section I tried to reproduce the same conditions used by Ginzburg and Balijepalli [65]. Again, the bilayer contained 3200 lipids and had an area of approximately $40 \times 40 \text{ nm}^2$. The temperature was set to $kT = \epsilon$ and, like the area, was held constant. I used five different sizes of spherical nanoparticles with radii ranging from 1.6 nm to 3.2 nm. I also ran simulations on infinite rods with the same radii. The Flory-Huggins parameter governing the attraction between NP and lipid head beads ranged from -3 to +1.

3.5.2.1 Spherical NP

Figure 3.12 shows the initial configuration for the spherical NP system. For every combination of parameters the NP became embedded in the bilayer. For each configuration, I observed whether the NP became wrapped by a single layer of lipids which Ginzburg and Balijepalli called a single-layer hybrid micelle or by a bilayer which they called a bilayer hybrid micelle. Figures 3.13 and 3.14 show cross sections of those two outcomes.

In addition to the type of micelle formed I also observed the formation of pores by certain NP.

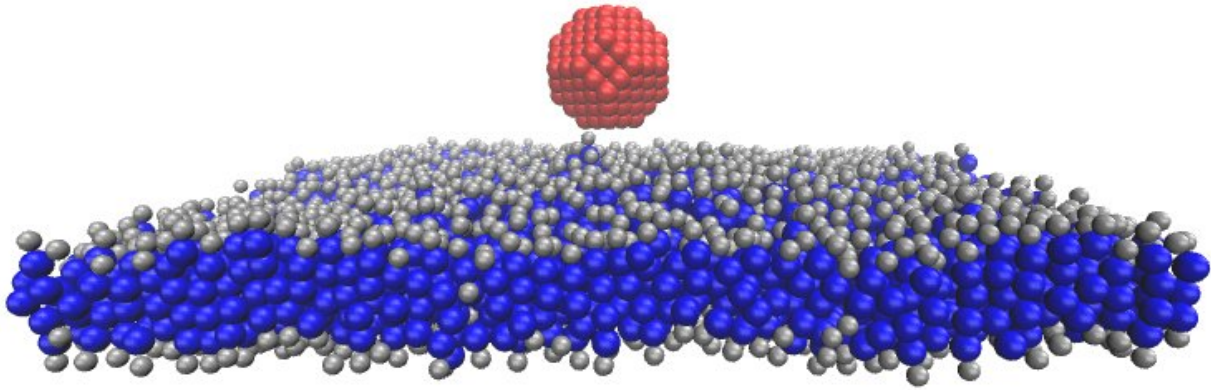


Figure 3.12: Typical starting configuration of my spherical nanoparticle/lipid bilayer simulations.

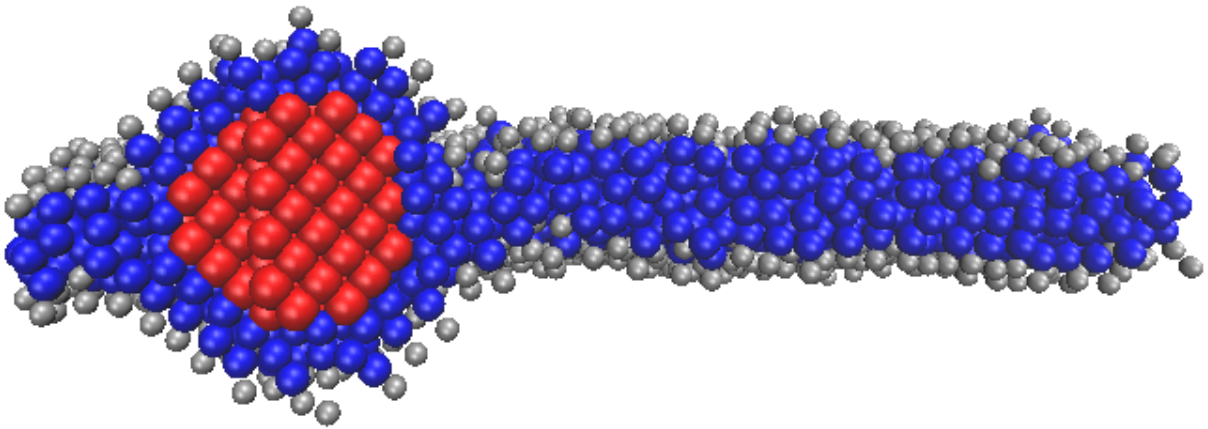


Figure 3.13: Cross section of single-layer hybrid micelle. A hydrophobic nanoparticle is embedded between two single layers of lipids.

In each of those cases the NP was wrapped by a bilayer. Figure 3.15 shows the top view of a NP embedded in a bilayer and the accompanying pore that is located adjacent to the NP as explained in section 3.1.1.2. The pore is mostly round while sharing an edge with the liposome. That allows it to maximize its area while minimizing the line energy around the edge of the pore.

Figure 3.16 shows my predicted phase diagram along with my simulation results. The symbols have the same meaning as in figure 3.9. The same discrepancies are present in the lower left and upper right. The same explanation given at the end of section 3.4 applies.

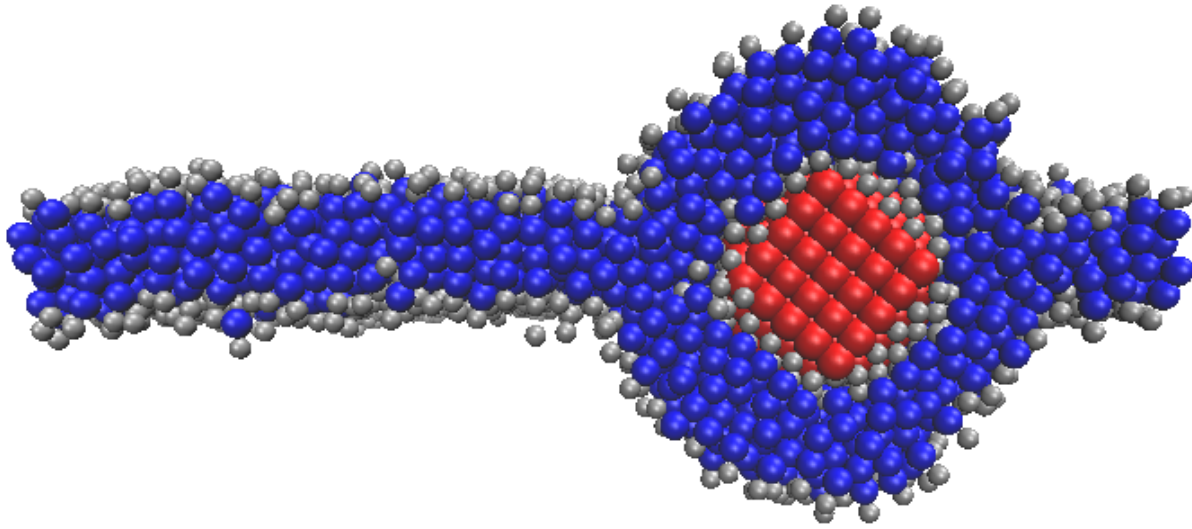


Figure 3.14: Cross section of bilayer hybrid micelle. A hydrophilic nanoparticle is surrounded by a bilayer and embedded in the membrane.

3.5.2.2 Rod-shaped NP

I performed the same simulations with “infinite” rod nanoparticles which spanned the simulation box with periodic boundaries. The radii of the rods were the same as those of the spherical nanoparticles. Figure 3.17 shows the starting configuration for the 3.2 nm rod.

In all cases the NP became embedded as either a singly wrapped micelle or a doubly wrapped liposome. Figure 3.18 includes the same phase diagram as figure 3.7 except scaled for the sizes I have used. The data points represent my simulation results.

The blue circles in the lower left represent narrow hydrophobic rods which form embedded micelles without a pore. These agree with state I predicted by my phase diagram. Figure 3.19 shows the resulting equilibrium state.

The red squares in the lower right represent thicker hydrophobic rods which form embedded micelles but also form small pores. These also agree with state I and are above the critical NP radius required for pore formation. Figure 3.20 shows one of these states. Notice the semicircular pore located adjacent to the micelle which is the most efficient shape.

The green diamonds in the upper region represent hydrophilic rods. In all cases the rod formed

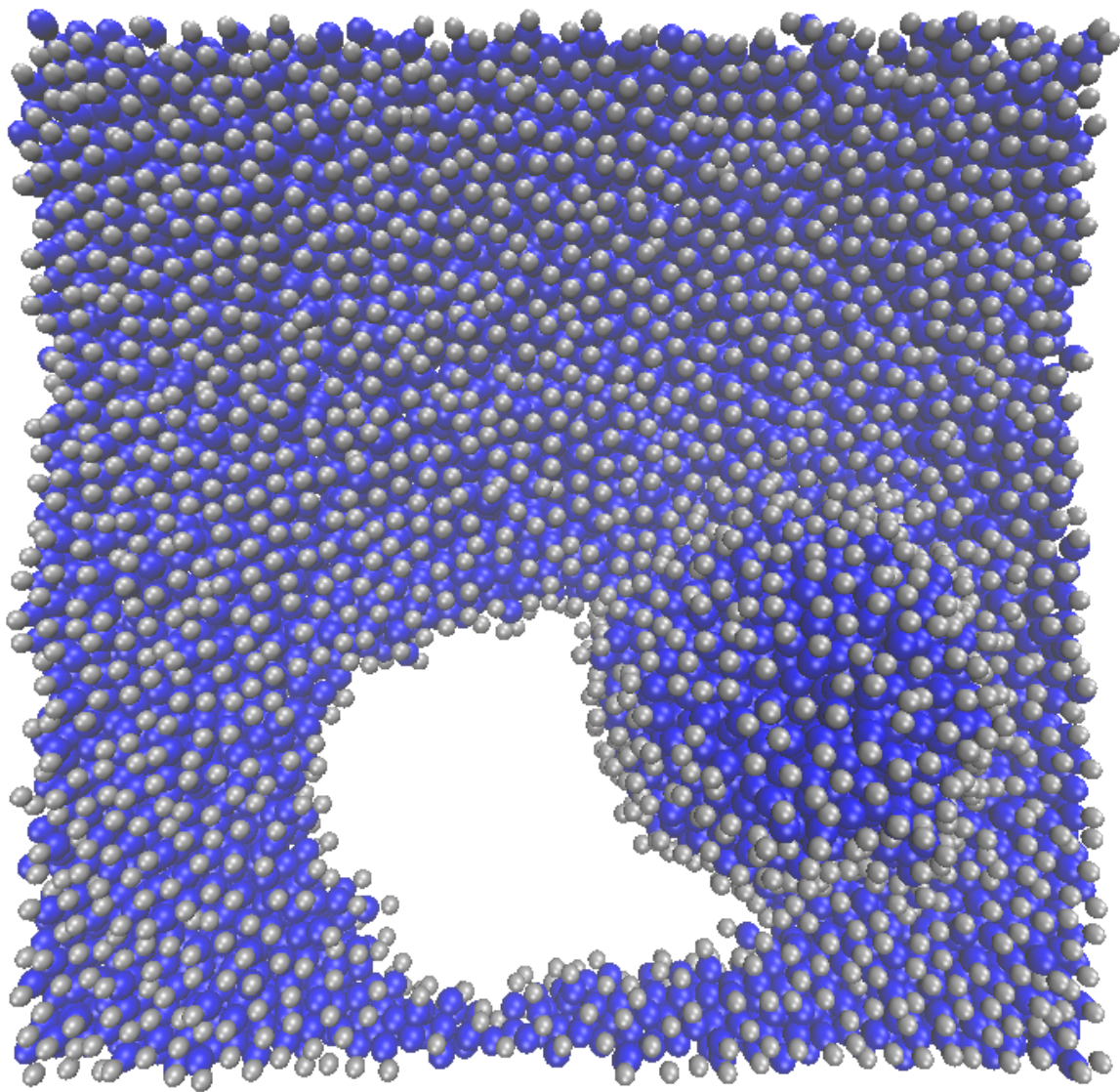


Figure 3.15: Strongly hydrophilic nanoparticle is wrapped by a bilayer and causes a pore in the membrane.

an embedded liposome and caused a pore which spanned the entire length of the LB. This is in agreement with state E predicted by my phase diagram. Figure 3.21 shows one such final state. The left side of the figure shows the severed edge that continues straight across the membrane. The right side of the liposome is smooth where it detached from the membrane.

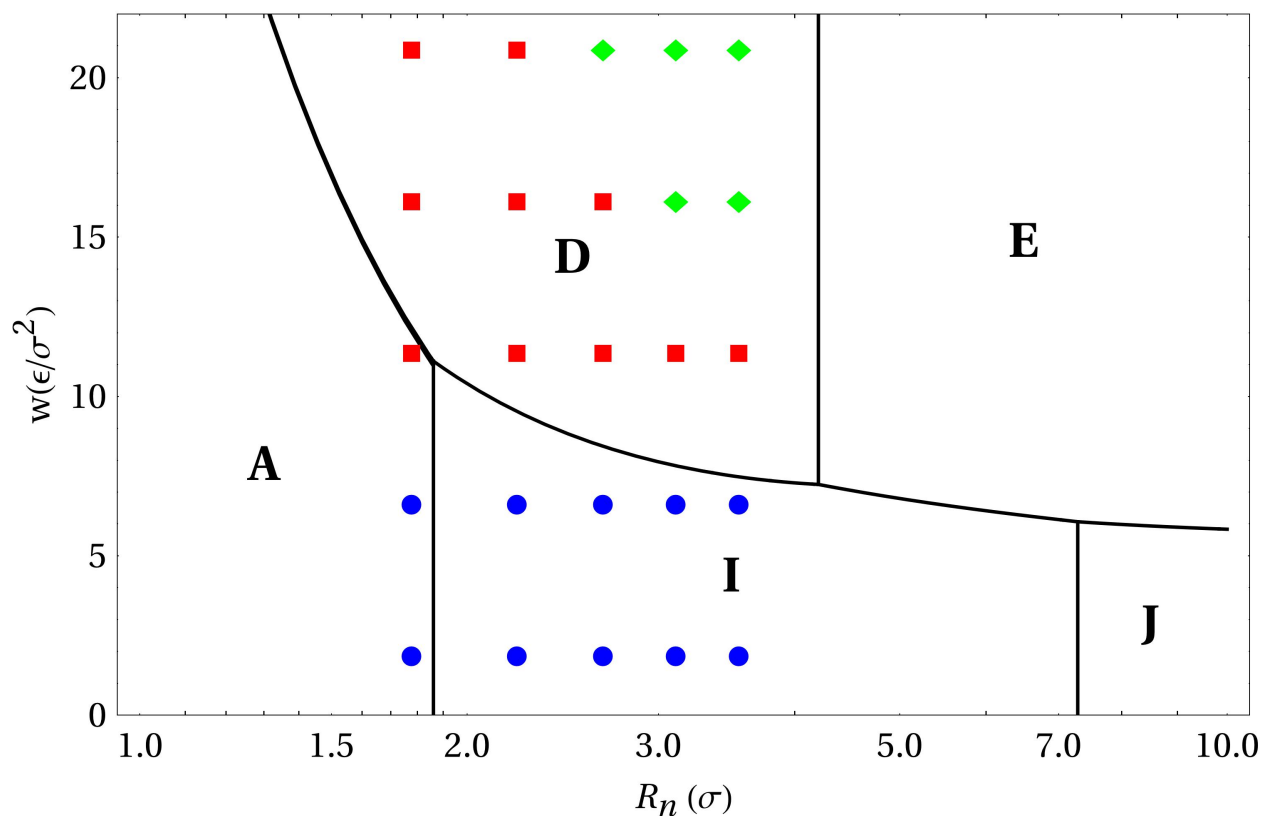


Figure 3.16: Phase diagram of spherical NP states. The x-axis shows the radius of the nanoparticle. The y-axis shows the attraction between the nanoparticle and lipid heads. **(A)** Dissociated reference state, **(D)** Embedded liposome without a pore, **(E)** Embedded liposome with a pore, **(I)** Embedded single-layer micelle without a pore, **(J)** Embedded single-layer micelle with a pore. Schematics and energies for each phase are given in figures (3.1 and 3.2).

Data points indicate my molecular dynamics results. **(Blue circles)**: Embedded micelles with no pores. **(Red squares)**: Embedded liposomes with no pores. **(Green diamonds)**: Embedded liposomes with pores.

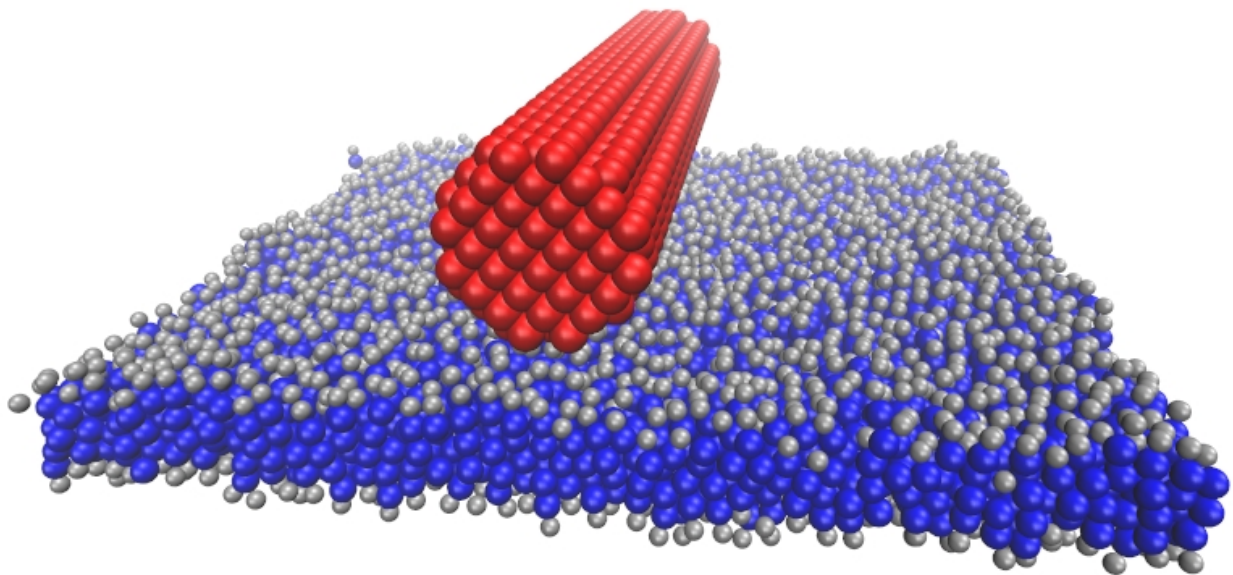


Figure 3.17: Typical starting configuration of my rod-shaped nanoparticle/lipid bilayer simulations.

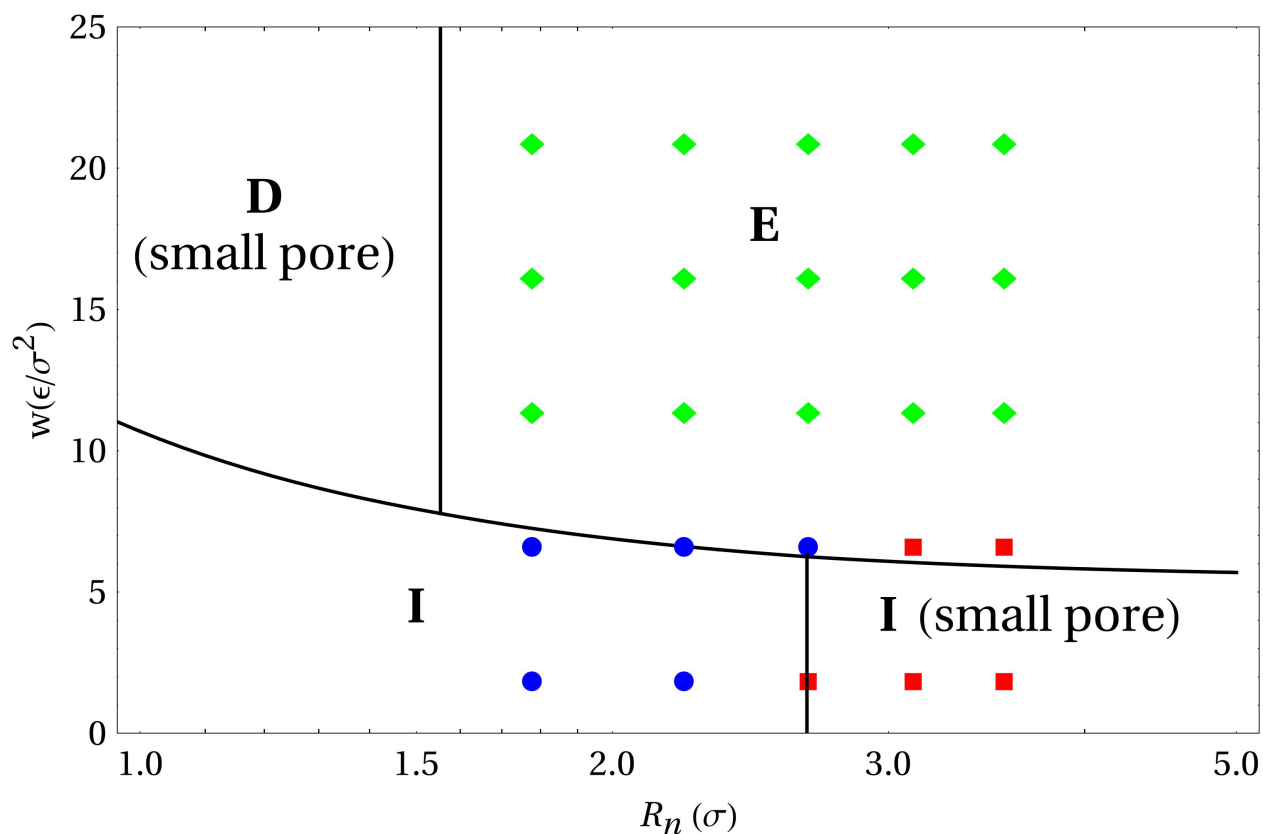


Figure 3.18: Phase diagram of rod-shaped NP states. The x-axis shows the radius of the nanoparticle. The y-axis shows the attraction between the nanoparticle and lipid heads. **(D)** Embedded liposome with a small pore, **(E)** Embedded liposome with a spanning pore, **(I)** Embedded single-layer micelle with a small pore or no pore. Schematics and energies for each phase are given in figures (3.3 and 3.4).

Data points indicate my molecular dynamics results. **(Blue circles)**: Embedded micelles with no pores. **(Red squares)**: Embedded micelles with small pores. **(Green diamonds)**: Embedded liposomes with spanning pores.

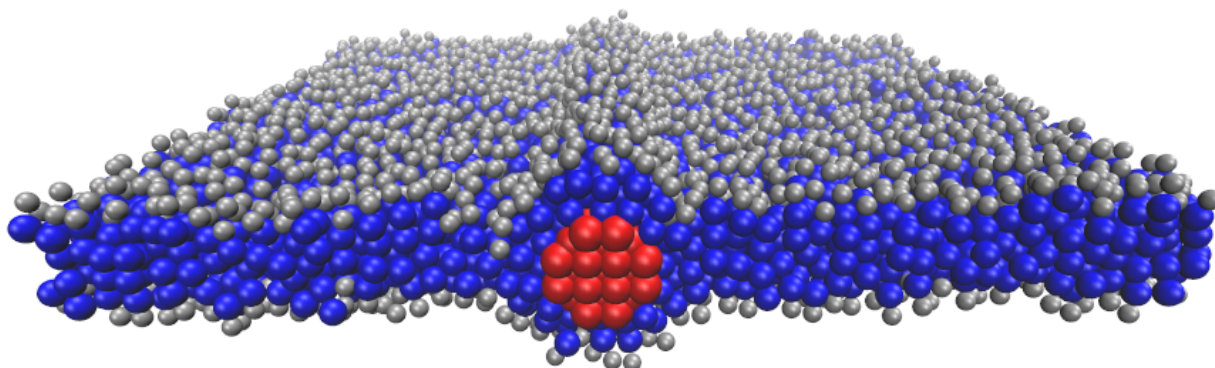


Figure 3.19: Narrow, hydrophobic, rod-shaped nanoparticle embedded in a bilayer. It is wrapped by a single layer of lipids and does not form a pore.

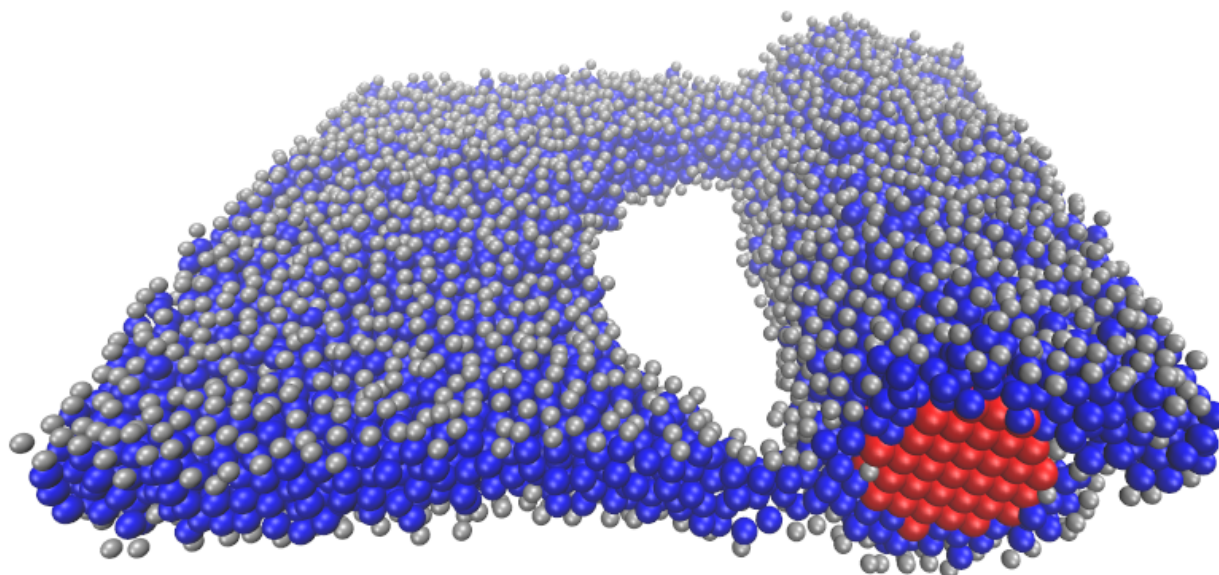


Figure 3.20: Thick, hydrophobic, rod-shaped nanoparticle embedded in a bilayer. It is wrapped by a single layer of lipids and does form a pore.

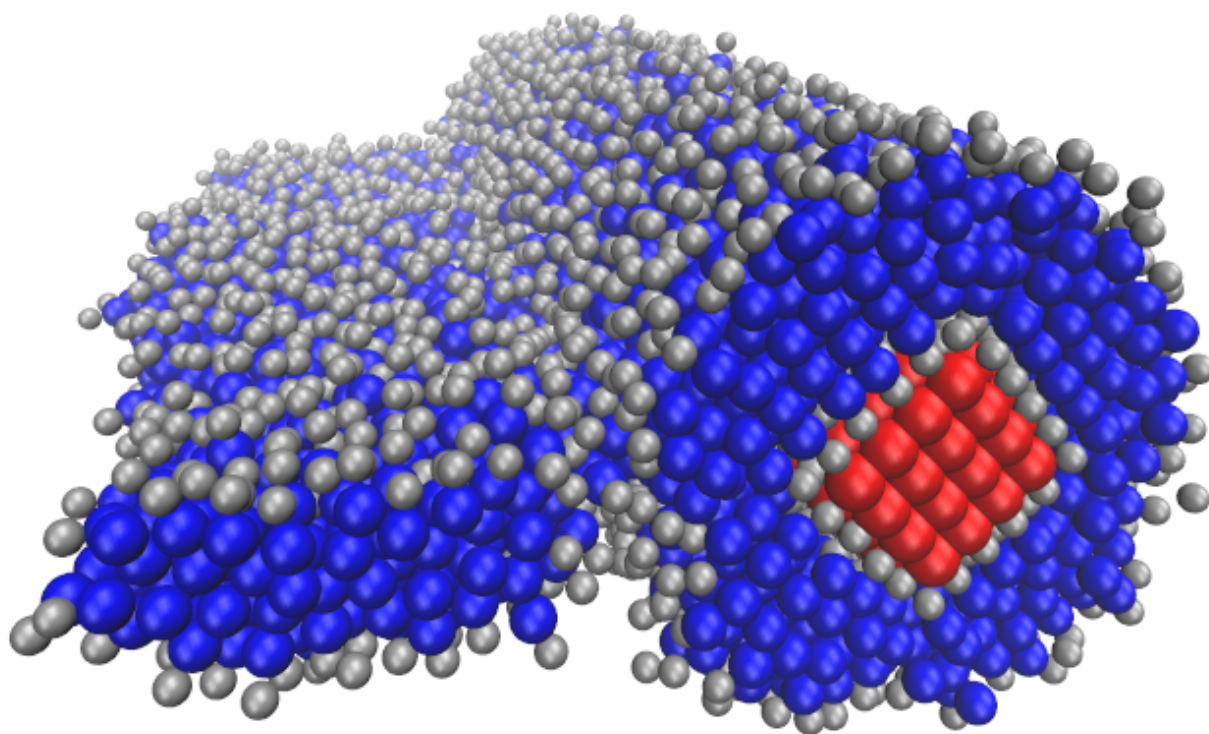


Figure 3.21: Strongly hydrophilic, rod-shaped nanoparticle embedded in a bilayer. It is wrapped by a double layer of lipids and has caused the membrane to rupture.

Chapter 4

LIPID BILAYER PORE DYNAMICS

4.1 Tension required for pore formation

There is an energy cost associated with membrane pores due to the curvature around the edge of the pore. This energy increases linearly with the radius of the pore. Therefore a pore is not energetically favorable unless a surface tension is applied to the membrane. Under low tension a pore will not form, or if formed will heal over time. For sufficiently large tension, a pore can lower the total energy by relieving this tension. In that case the energy will continue to decrease as the pore grows until all of the tension is released. In this section I will calculate the critical relation between surface tension and pore size.

4.1.1 Fracture mechanics

This problem is similar to the fracturing of materials. Griffith studied the effect of cracks on stressed materials [76]. Consider an object with an applied stress, σ , which experiences a corresponding strain, ε . The Young's modulus, E , is equal to the ratio σ/ε and is an intrinsic property of the material. The energy stored in the stretched material per unit volume is

$$U^* = \int \sigma d\varepsilon$$
$$U^* = \frac{E\varepsilon^2}{2} = \frac{\sigma^2}{2E} \quad (4.1)$$

Now consider a crack of length a perpendicular to the applied stress which spans the entire height of the material (t). The crack will lower the stress energy for part of the object while adding energy due to the broken bonds along the inner surface of the crack. If the crack starts at the outer edge of the object, the volume of the region of relieved stress will be a triangular prism of height t . The area of the triangular base turns out to be πa^2 . The relieved stress energy is then

$$U = -\frac{\sigma^2}{2E}(\pi a^2 t) \quad (4.2)$$

The additional surface energy is equal to the inner surface area of the crack, $2at$, times a material specific surface energy constant, γ .

$$S = 2\gamma at \quad (4.3)$$

The critical crack size can be found by setting the derivative of the total energy equal to zero

$$\frac{d(U+S)}{da} = -\frac{\pi\sigma^2 t}{E}a + 2\gamma t = 0 \quad (4.4)$$

$$\Rightarrow a_c = \frac{2\gamma E}{\pi\sigma^2} \quad (4.5)$$

For a given stress, a_c is the critical crack size. Cracks larger than this will continue to propagate. Solving equation (4.4) instead for σ gives the critical stress required for a starting crack of length a to grow.

$$\sigma_c = \sqrt{\frac{2\gamma E}{\pi a}} \quad (4.6)$$

Notice that these relations do not depend on the thickness of the object which means a similar approach can be used to analyze the continuum membrane model.

4.1.2 Membrane rupturing

In section 3.1.3 I used a similar energy balancing to look at the criteria for pore formation in a membrane under tension. I will briefly rederive the critical pore radius here. Considering only the pore dependent terms from equation (3.26) the free energy consists of a stretching term and a line energy term

$$F = -\pi R_p^2 \Sigma + 2\pi R_p \gamma \quad (4.7)$$

where Σ is the surface tension and γ is a constant related to the bending modulus. The line energy is due to the fact that lipid heads will curve around the edge of the pore to cover the hydrophobic tails and is proportional to the circumference of the pore. Differentiating this energy with respect to R_p gives

$$\frac{dF}{dR_p} = -2\pi\Sigma R_p + 2\pi\gamma = 0 \quad (4.8)$$

$$\Rightarrow R_{pc} = \frac{\gamma}{\Sigma} \quad (4.9)$$

For a given applied tension, R_{pc} gives the critical pore size. Small pores will heal over time. Pores larger than the critical size will grow indefinitely. The metastable pore can be observed if the membrane area is held constant. If a membrane is stretched to sufficient tension a pore will form. Figure 3.5 from section 3.2 shows tension versus membrane area for a simulation in which the area was slowly increased. The sharp drop indicates pore formation. Beyond that transition the tension decreases like $A^{-1/2}$ as shown by Cooke and Deserno [37, 40]. While the entire membrane does stretch, most of the increased area is added to the pore. Therefore the critical pore radius and critical tension are in fact inversely proportional. For any area above the critical value in figure 3.5 there is a pore and a corresponding tension given by equation (4.9). If the simulation is run instead at constant tension, then the pore will be unstable. If either the pore radius or tension are decreased, the pore will heal. If either are instead increased, then the pore will grow until it spans the entire membrane.

4.2 Dynamics of pore healing

In this section I will determine theoretically how the size of a pore changes over time and compare with MD simulations.

4.2.1 Predicted time dependence

I will now calculate how the time required for pore healing scales with the size of the pore. In order for the pore to heal in the presence of tension, the pore radius must not exceed the critical value in equation (4.9). In the absence of tension, the pore energy will always be positive and it will therefore always heal. A flat lipid bilayer with a pore can be viewed as a two dimensional system with two phases. The main phase is the homogeneous region containing lipids. The second phase is the pore which contains no lipids. We can use lipid concentration (c) as the order parameter to distinguish the two phases. In the case of zero tension the concentration is not conserved. Filling in the pore (increasing the concentration in one phase) does not change the concentration in the surrounding area. It is known that the interface between two phases in a non-conserved system will move with a speed proportional to the mean curvature of the interface [77]. I will rederive that result below.

Cahn and Hilliard showed that the free energy of a phase segregated system contains a homogeneous term representing the energy within each region as well as gradient term representing the energy of the interface [78]. The total free energy is then

$$F = N_v \int_V [f_0(c) + \kappa(\nabla c)^2 + \dots] dV \quad (4.10)$$

where N_v is the number of particles per unit volume, $f_0(c)$ is the homogeneous volume energy which depends only on the concentration, c . Only even powers of the gradient are present because the scalar energy must be invariant with respect to the direction of the gradient. While the energy can depend on higher powers of the gradient, only the lowest order term is kept if we assume the gradient to be much smaller than the reciprocal of the distance between particles. The variational derivative of the free energy with respect to the concentration is

$$\frac{\delta F}{\delta c} = \frac{\partial f_0}{\partial c} - \nabla \cdot \left(\frac{\partial}{\partial(\nabla c)} \kappa(\nabla c)^2 \right) \quad (4.11)$$

$$= f_0'(c) - 2\kappa(\nabla^2 c) \quad (4.12)$$

The variational derivative is a local thermodynamic force which is assumed to be proportional to the rate of change of the order parameter [77].

$$\frac{\partial c}{\partial t} = -\alpha \frac{\delta F}{\delta c} \quad (4.13)$$

This is a phenomenological assertion. It contains only the first time derivative because the system is in an overdamped liquid state. Combining equations (4.11) and (4.13) leads to

$$\frac{\partial c}{\partial t} = \alpha(2\kappa(\nabla^2 c) - f'_0(c)) \quad (4.14)$$

$$\Rightarrow \frac{1}{2\alpha\kappa} \frac{\partial c}{\partial t} = \nabla^2 c - \frac{f'_0(c)}{2\kappa} \quad (4.15)$$

By absorbing $2\alpha\kappa$ into the time scale and defining

$$V(c) = \frac{f_0(c)}{2\kappa} \quad (4.16)$$

we arrive at the time-dependent Ginzburg-Landau equation

$$\frac{\partial c}{\partial t} = \nabla^2 c - V'(c) \quad (4.17)$$

Now let us apply this equation to the case of a pore centered at the origin in a two dimensional membrane. I will follow the same procedure used by Krapivsky et al. to look at the shrinking of a spherical droplet [79]. The system can be described in polar coordinates with no angular dependence. We can assume the concentration has the following form

$$c(r,t) = m(r - R(t)) \quad (4.18)$$

where r is the radial coordinate and $R(t)$ is the time dependent pore radius. If we define $x = r - R(t)$, then $m(x)$ is defined over the domain $x \geq -R(t)$ with a sharp transition at $x = 0$. The concentration is zero for negative x and becomes a positive constant for positive x . The left-hand side of equation (4.17) becomes

$$\frac{\partial m}{\partial t} = \frac{\partial m}{\partial x} \frac{\partial x}{\partial t} = -m' \frac{\partial R}{\partial t} \quad (4.19)$$

Using polar coordinates, the Laplacian term becomes

$$\frac{1}{r} \frac{\partial}{\partial r} \left(r \frac{\partial m}{\partial r} \right) = m'' + \frac{m'}{r} = m'' + \frac{m'}{R(t) + x} \quad (4.20)$$

Equation (4.17) is then

$$m'' + \left(\frac{1}{R(t) + x} + \frac{\partial R}{\partial t} \right) m' - V'(m) = 0 \quad (4.21)$$

Multiplying equation (4.21) by m' and integrating over x from $-R(t)$ to ∞ gives

$$\frac{1}{2} (m')^2 \Big|_{-R(t)}^{\infty} + \int_{-R(t)}^{\infty} \left[\frac{1}{R(t) + x} + \frac{\partial R}{\partial t} \right] (m')^2 dx - V(x) \Big|_{-R(t)}^{\infty} = 0 \quad (4.22)$$

The first is zero because m is constant away from the interface. The third term is proportional to the difference in volume energy in the membrane compared to in the pore. It is equal to zero in the pore and equal to a constant in the membrane which I will call $-V$. It is negative because of the negative potential energy from lipid attraction. Since $(m')^2$ is large near the interface and zero away from it, the second term is equal to the expression in square brackets evaluated at the interface ($x = 0$). Equation (4.22) becomes

$$\left[\frac{1}{R(t) + x} + \frac{\partial R}{\partial t} \right]_{x \rightarrow 0} + V = 0 \quad (4.23)$$

which finally gives the equation of motion for the pore radius

$$\frac{dR}{dt} = \frac{-1}{R} - V \quad (4.24)$$

Remember that multiple material dependent constants were absorbed into the time scale. To make this clear I will add constants to equation (4.24).

$$\frac{dR}{dt} = \frac{-A}{R} - B \quad (4.25)$$

where A is proportional to the line energy around the pore and B is proportional to the volume energy inside the membrane. Since both A and B are positive, both terms are driving the pore shut. Separating variables and integrating, gives

$$\int_{R_0}^R \frac{-R'}{BR' + A} dR' = \int_0^t dt' \quad (4.26)$$

where R_0 is the initial pore radius. The resulting equation is

$$\frac{1}{B^2} \left(B(R_0 - R) - \text{Log} \left[\frac{A + BR}{A + BR_0} \right] \right) = T \quad (4.27)$$

While this does not have an analytic solution, it can be solved numerically. To understand its general behavior I will consider the two limiting cases where A or B are zero. $B = 0$ means that the volume energy is the same both inside the membrane and the pore. This corresponds to a magnetic system in which a region of spins with a certain orientation is surrounded by spins of the opposite orientation. The energy within each region is the same and the dynamics are governed completely by the curvature at the interface. Equation (4.25) reduces to the well known Allen-Cahn equation [77] in two dimensions. In a general non-conserved system, a non-equilibrium interface will move with a speed proportional to the mean curvature of the interface. In this limit, the equation of motion for the pore radius is

$$R = \sqrt{R_0^2 - 2At} \quad (4.28)$$

It is known that the size of domains in non-conserved systems scale as $t^{1/2}$. The area of the pore is

$$A_p = A_{p0} - 2\pi At \quad (4.29)$$

where A_{p0} is the initial pore area. The area decreases linearly with time.

If on the other hand we consider $A = 0$, we are completely neglecting the line energy around the pore. The system is governed by the difference in volume energies. It behaves like a pressure difference across the interface, closing the pore. The equation of motion becomes

$$R = R_0 - Bt \quad (4.30)$$

In this case the radius decreases linearly and the area is

$$A_p = \left(\sqrt{A_{p0}} - \sqrt{\pi B} t \right)^2 \quad (4.31)$$

We can expect the actual solution to equation (4.25) to lie somewhere between the two extremes of equations (4.29) and (4.31). In the next section I will show simulation results for pore healing. The area does appear to decrease quadratically. I will now show how the fit parameters from a second order polynomial fit can be related to the constants A and B in equation (4.25). If the initial pore radius at time zero is R_0 , then equation (4.25) can be used to find the initial first and second derivatives.

$$\dot{R}(0) = \frac{-A}{R_0} - B \quad (4.32)$$

$$\ddot{R}(0) = \frac{A\dot{R}(0)}{R_0^2} = \frac{-A}{R_0^2} \left(\frac{A}{R_0} + B \right) \quad (4.33)$$

Now assume that the pore area can be approximately fit by

$$A_p = C_0 t^2 + C_1 t + C_2 \quad (4.34)$$

C_2 is clearly the starting pore area (πR_0^2). The pore radius can be expressed as

$$R = \sqrt{\frac{C_0}{\pi} t^2 + \frac{C_1}{\pi} t + R_0^2} \quad (4.35)$$

The initial first and second derivatives of equation 4.35 are

$$\dot{R}(0) = \frac{C_1}{2\pi R_0} \quad (4.36)$$

$$\ddot{R}(0) = \frac{1}{2\pi} \left(\frac{2C_0}{R_0} - \frac{C_1^2}{2\pi R_0^3} \right) \quad (4.37)$$

By setting equation (4.32) equal to (4.36) and equation (4.33) equal to (4.37), C_0 and C_1 can be solved for in terms of A and B .

$$C_0 = \pi B \left(\frac{A}{R_0} + B \right) \quad (4.38)$$

$$C_1 = -2\pi(A + BR_0) \quad (4.39)$$

A quadratic approximation of the solution to equation (4.25) is therefore

$$A_p = \pi \left[B \left(\frac{A}{R_0} + B \right) t^2 - 2(A + BR_0)t + R_0^2 \right] \quad (4.40)$$

In order to determine the relative contributions to healing, one can fit data to see if it is mostly linear, as predicted by Allen-Cahn, or if there is a significant quadratic component.

4.2.2 Simulation results

I have run simulations on both a flat LB with periodic boundaries and a spherical LB vesicle and observed how a pore heals over time. The Cooke lipid model [36, 37] was again used.

4.2.2.1 Flat LB

I began with an equilibrated 80x80 LB with periodic boundaries under zero tension. Unlike the fixed area simulations in chapter 3 these simulations required free tensionless boundaries to allow closing of the pore. A pore was made in the center by removing lipids within a radius of 8σ (≈ 9 nm). That left tail beads initially exposed around the edge of the pore. Figure 4.1 shows three different states during healing.

I calculated the area of the pore by dividing the LB into a 2D grid of bins approximately $1 \sigma^2$ each. Any bin which doesn't contain a bead contributes to the pore area. Figure 4.2 shows the pore area calculated every 1τ for 20 different runs. There is initially a rapid decrease in area as lipids

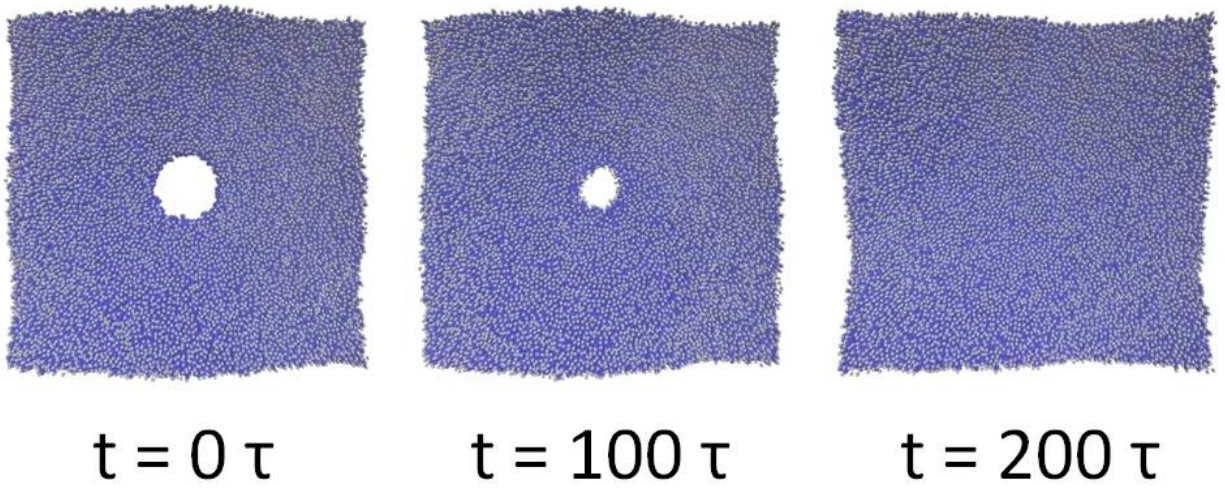


Figure 4.1: Snapshots of pore healing in a flat LB at three different times.

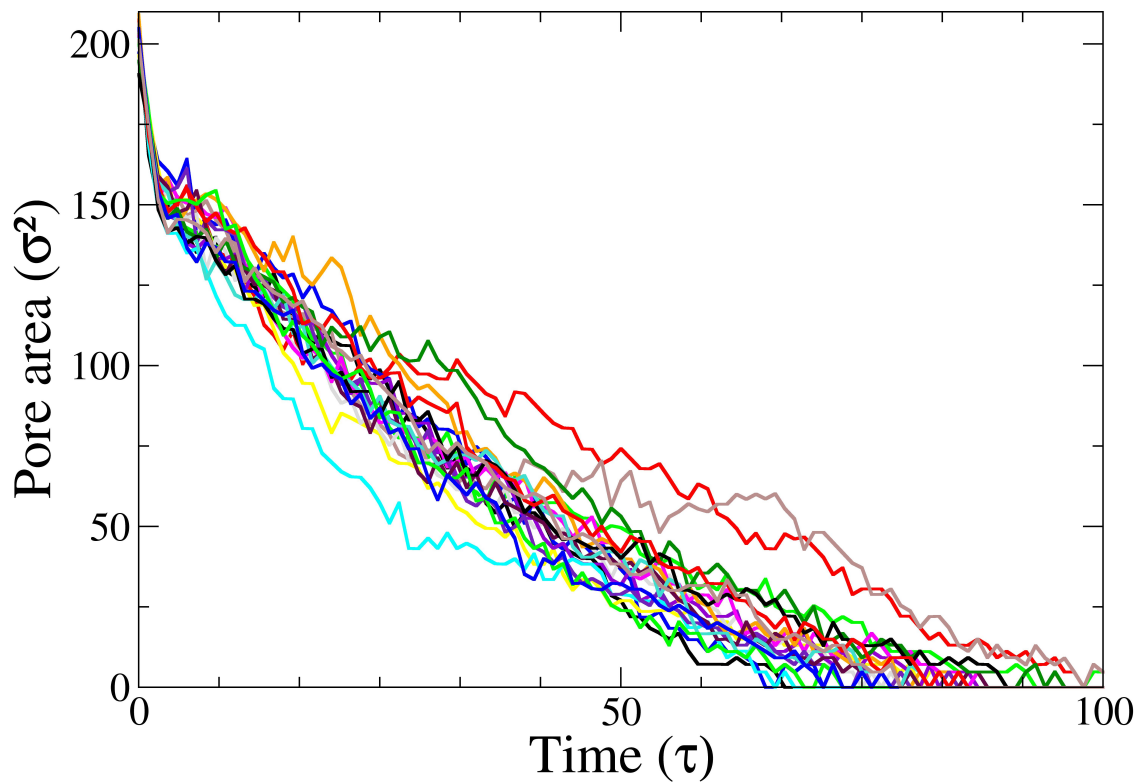


Figure 4.2: Pore area versus time in a flat lipid bilayer under zero tension. This is the raw data from 20 different runs.

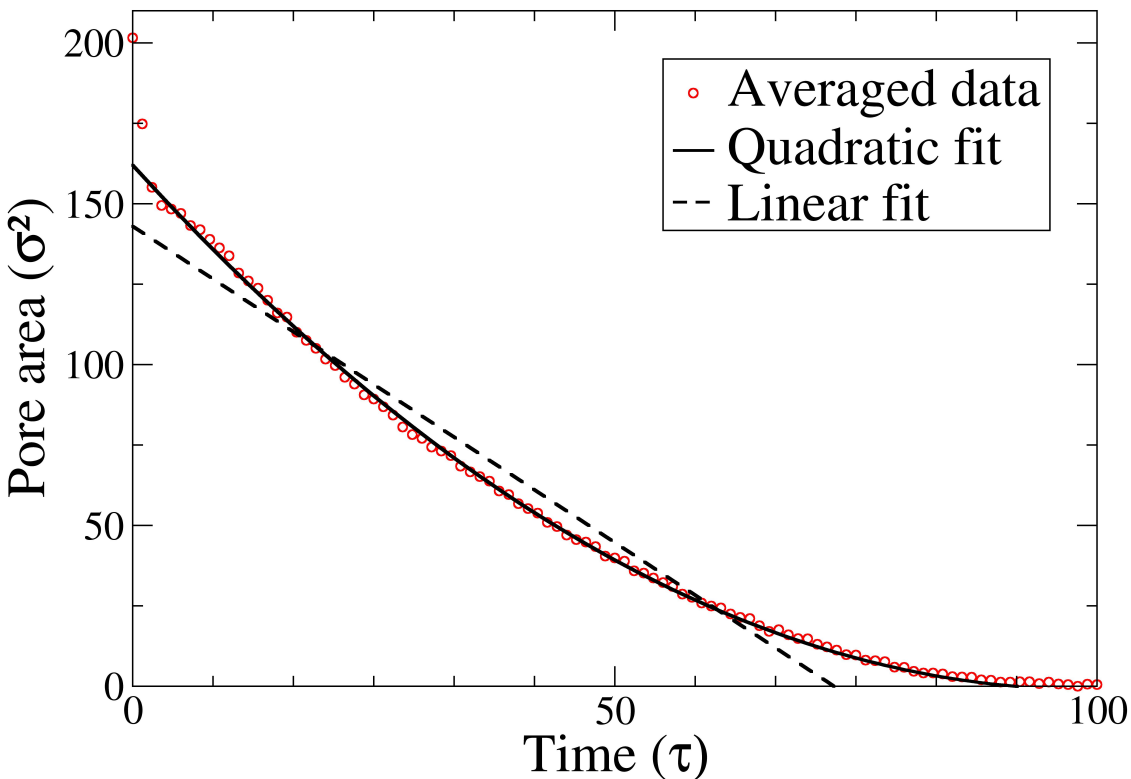


Figure 4.3: Averaged pore area versus time in a flat lipid bilayer under zero tension. The data in figure 4.2 was averaged (red circles) and fit to a quadratic function (solid black line) as well as a linear function (dashed black line).

curve around to coat the interior of the pore with lipid heads. This occurs within a few τ . There is a large variation in closing times, which I define as when the pore area first becomes zero.

Figure 4.3 shows an average of the 20 runs. Each run is a piecewise function which is decreasing at early times and becomes zero beyond the closing time. I believe the averaged data contains three distinct regions. There is a rapid decrease during the first 10 τ in which lipids are bending around the edge. After this initial relaxation there is a more gradual decrease in area lasting about 50 τ . This middle region is most likely to correspond to the dynamics discussed in the previous section. At late times there is a tail which I believe is mostly due to averaging data with different closing times.

	C_0	C_1	C_2
Flat LB	0.017 ± 0.002	-3.3 ± 0.2	162 ± 9
Vesicle	0.007 ± 0.002	-3.5 ± 0.3	342 ± 5

Table 4.1: Parameters for the pore area versus time data, fit to quadratic equation (4.34).

In order to isolate the middle region, I removed the very early time data as well as the zeros after the pore is closed before fitting each run separately to equation (4.34). The averages of those fit parameters are shown in table 4.1. The averaged quadratic fit is represented by the solid black line in figure 4.3.

While the coefficient for the quadratic term is not zero, the linear term is dominant throughout the closing process. The average closing time, equal to the first root of equation (4.34), is 92τ . The time at which the quadratic and linear terms are equal is 198τ . Therefore a linear approximation should be reasonable. Figure 4.3 also shows the average linear fit to the data represented by the dashed black line. The closing time predicted by the linear fit is 73τ which is an underestimate of about 20% compared to the quadratic fit.

4.2.2.2 Spherical vesicle

I also ran simulations on a spherical vesicle with an initial radius of about 20σ (≈ 18 nm). I created a pore by removing 10% of the lipids within a certain polar angle. Figure 4.4 shows the initial configuration as well as an intermediate state and the fully healed vesicle.

I calculated the pore area by dividing the surface of the spherical vesicle into equal area bins identified by their angular coordinates, θ and ϕ . Bins which did not contain any beads were counted as part of the pore. Figure 4.5 shows the pore area versus time for 20 different runs.

Figure 4.6 shows the average of the data in figure 4.5. There are again three distinct regions: an initial sharp drop, then a long gradual decline, and finally a rounded tail. I once more removed the early time data and late time zeros from each run before fitting them to a quadratic function. The averaged quadratic fit parameters are listed in table 4.1. This time the quadratic coefficient is

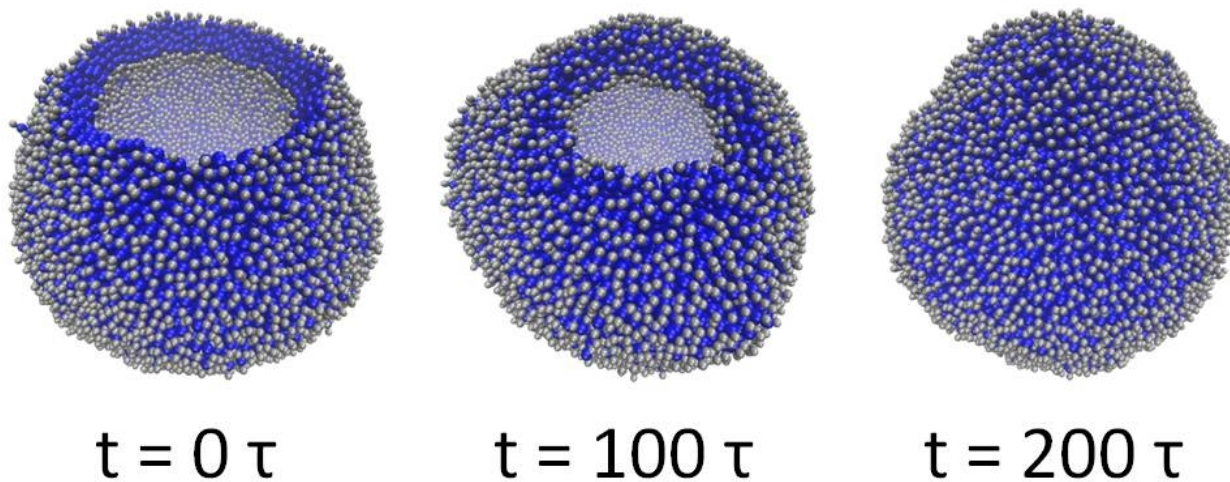


Figure 4.4: Snapshots of pore healing in a spherical vesicle at three different times.

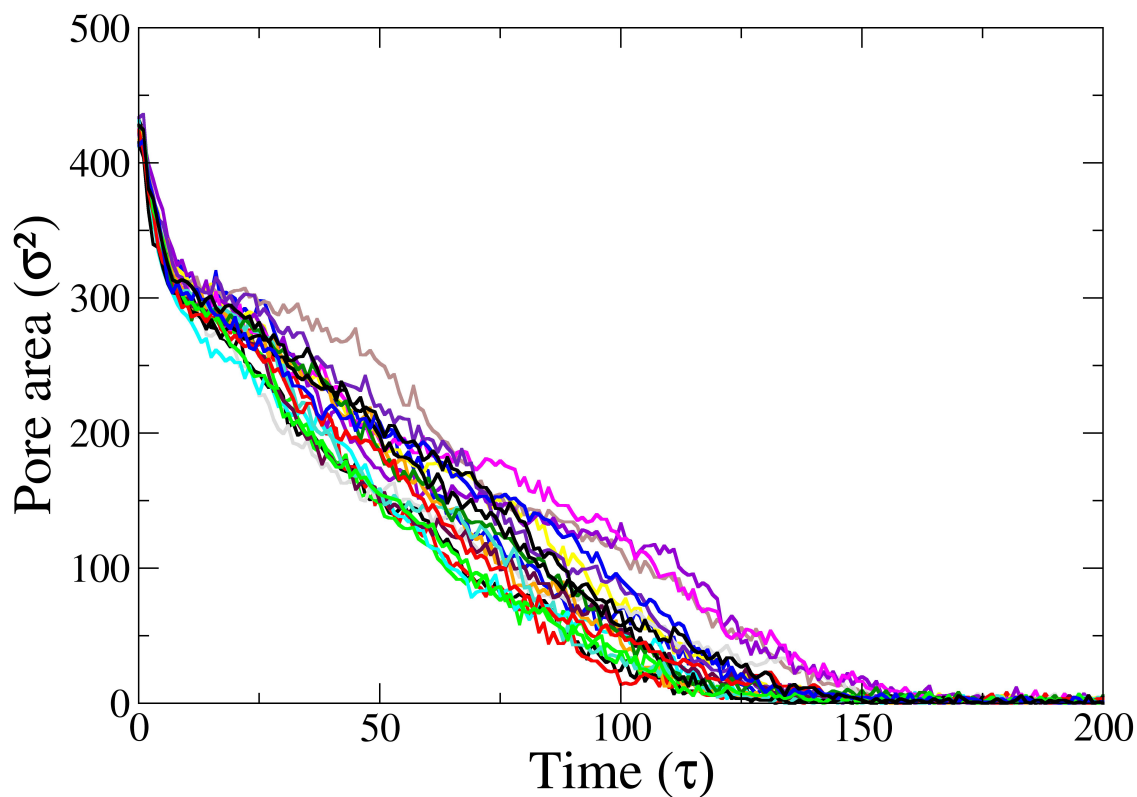


Figure 4.5: Pore area versus time for a spherical vesicle. This is the raw data from 20 different runs.

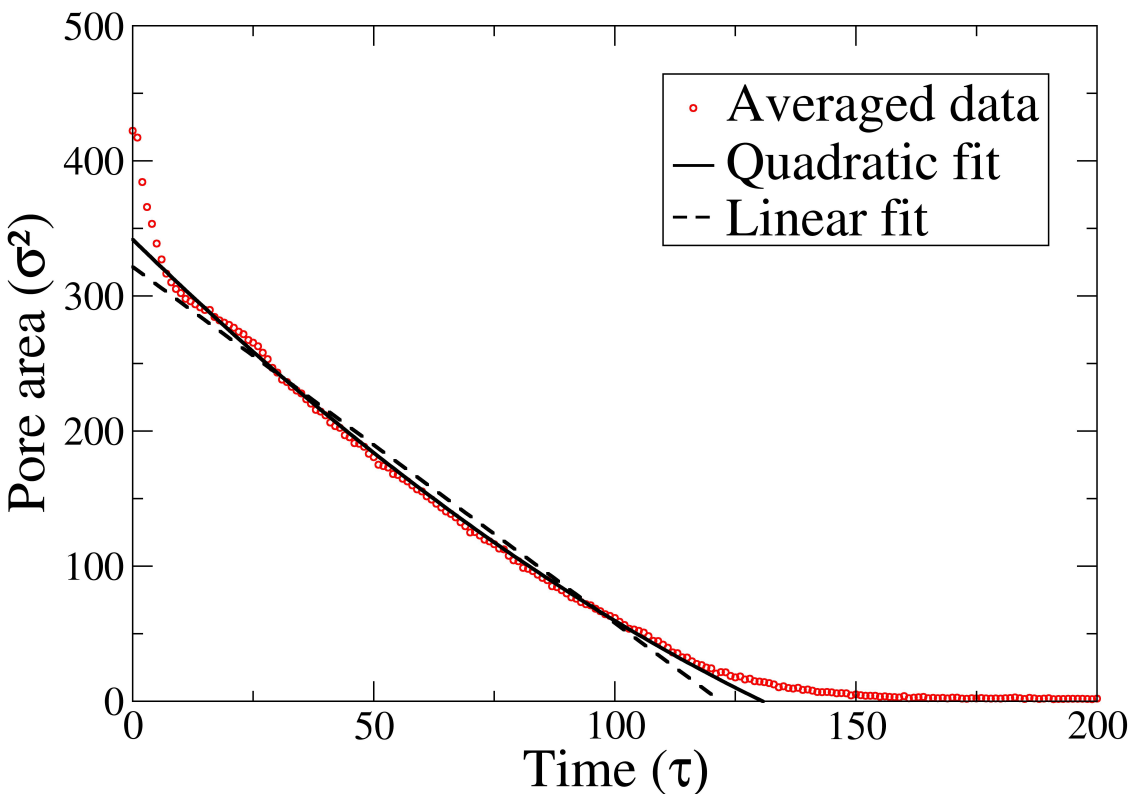


Figure 4.6: Averaged pore area versus time for a spherical vesicle. The data in figure 4.5 was averaged and fit to both a linear and quadratic function.

even smaller. The estimated closing times from the quadratic and linear fits are 131τ and 122τ respectively. The linear approximation still underestimates the closing time, but only by 7% in this case.

It appears that the area of pores decrease linearly at early times and that the process can be explained by a simple Allen-Cahn theory. The pore closing is driven primarily by the membrane curvature around the pore. I believe there is a different process at work later on. Lipids which are initially oriented with their heads pointing toward the center of the pore must reorient themselves. The large variation in closing times among my simulation runs indicates that this is an activated process. It is known that Allen-Cahn theory is only valid when the thickness of the interface, which

in this case is on the order of the LB thickness, is much smaller than the radius of curvature of the pore. In my flat LB simulation, the radius of curvature is only about twice as large as the interface thickness. In the vesicle simulation the ratio is closer to four, which may explain why the vesicle data is more linear.

While Allen-Cahn theory can explain the healing dynamics of pores which are much wider than the LB thickness, a different theory is needed to understand the final closing process.

4.2.2.3 Alternative fitting

While the quadratic and linear fits of the previous two sections are meant to describe the middle region of decreasing area, I have also fit the entire averaged data sets shown in figures 4.3 and 4.6. In an attempt to capture the nonlinear early and late time behavior, I fit each data set to the following two equations

$$A_p = A_0 \cdot \exp(-A_1 \cdot t) + A_2 \cdot t^2 + A_3 \cdot t \quad (4.41)$$

$$A_p = B_0 \cdot \exp(-B_1 \cdot t) + B_2 \cdot \exp(-B_3 \cdot t) \quad (4.42)$$

which I refer to as “exponential plus quadratic” and “double exponential”. Figure 4.7 shows the flat lipid bilayer data fit to both the exponential plus quadratic represented by the solid green line and the double exponential represented by the dashed blue line. Tables 4.2 and 4.3 list the corresponding fit parameters. After finding an insignificant quadratic coefficient I performed another fit excluding that term. Since equations (4.41) and (4.42) each contain four fit parameters they do a comparable job fitting the data. The two fit lines are nearly overlapping throughout the entire range.

Figure 4.8 shows the averaged vesicle data again fit to equations (4.41) and (4.42). While the quadratic coefficient was rather small, including the term significantly improved the fit in this case.

Both new functions do a reasonable job fitting the middle and late time behavior, but still miss the early time relaxation. Perhaps such models could be used to represent the entire evolution of

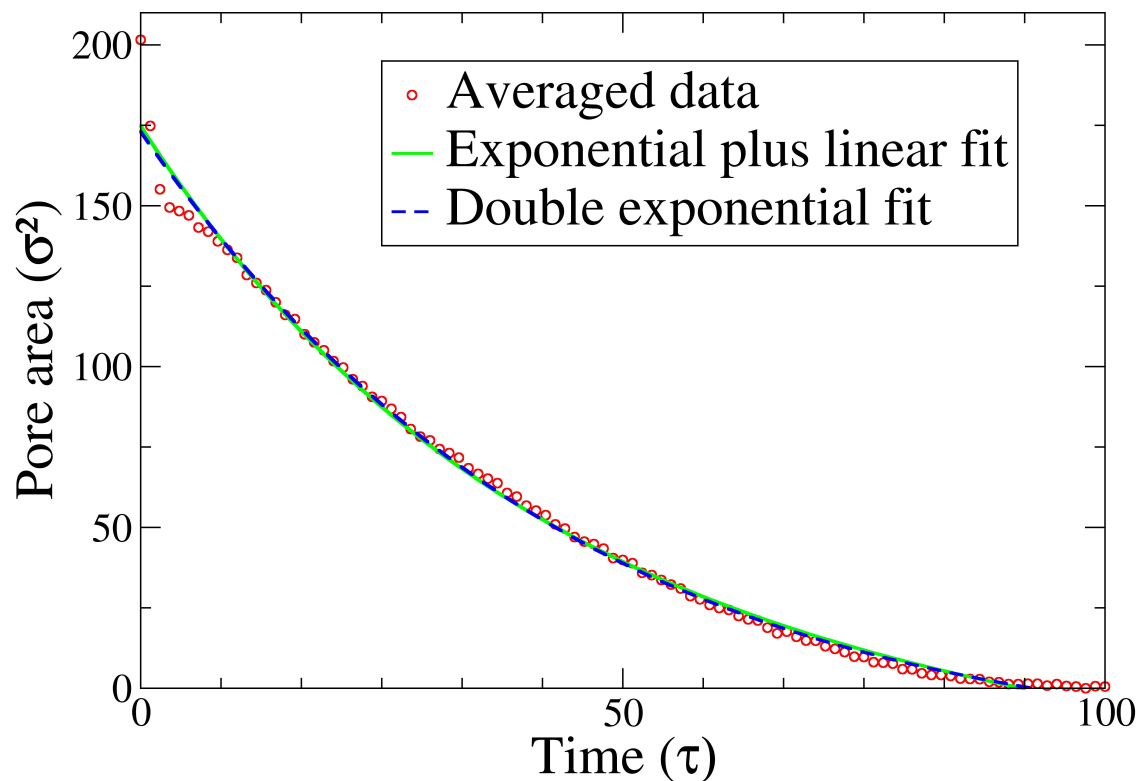


Figure 4.7: Averaged flat lipid bilayer pore data with alternative fits. The data in figure 4.2 was averaged (red circles) and fit to a an exponential plus a linear term (solid green line) as well as a double exponential (dashed blue line).

	A_0	A_1	A_2	A_3
Flat LB	175	0.0257	N/A	-0.182
Vesicle	366	0.00560	0.00934	-2.43

Table 4.2: Parameters for the pore area versus time data, fit to an exponential plus quadratic equation (4.41).

a healing pore. However, I believe it would be much more useful to understand and model the behavior in each of the three regions separately as part of a comprehensive model.

	B_0	B_1	B_2	B_3
Flat LB	9400	0.0145	-9230	0.0142
Vesicle	-1730	0.0322	2090	0.0280

Table 4.3: Parameters for the pore area versus time data, fit to a double exponential equation (4.42).

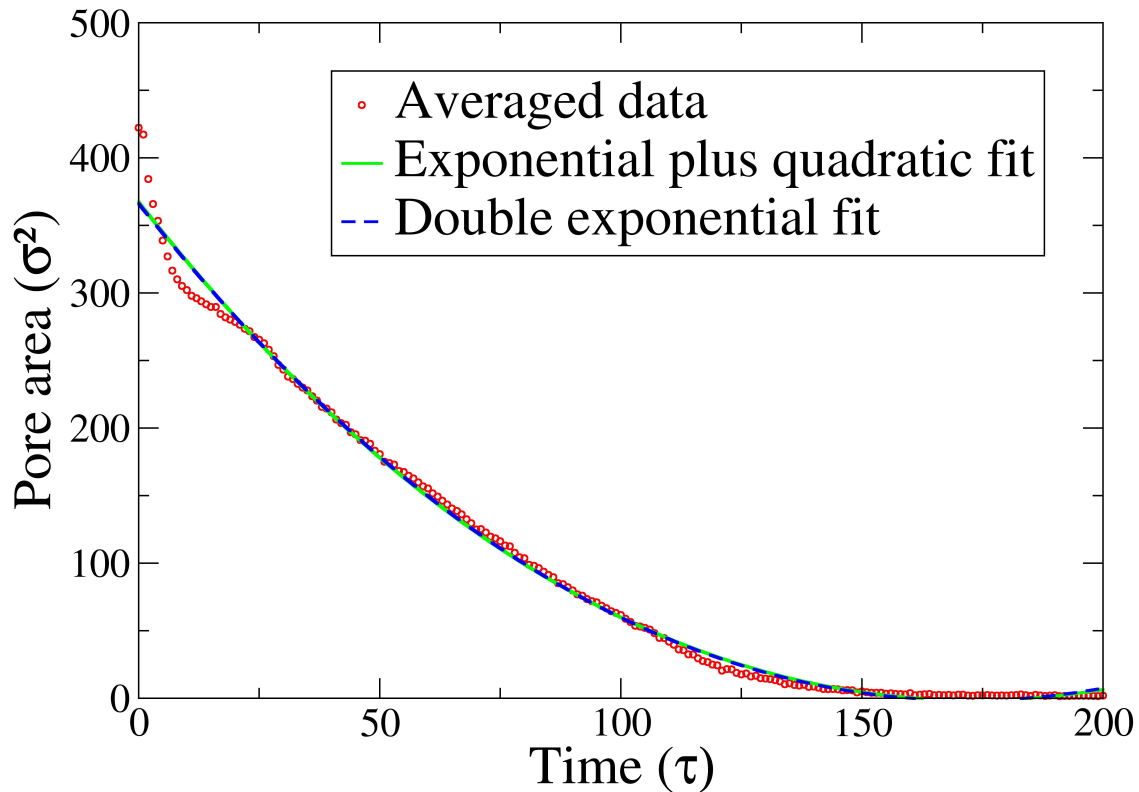


Figure 4.8: Averaged vesicle pore data with alternative fits. The data in figure 4.5 was averaged (red circles) and fit to an exponential plus a quadratic function (solid green line) as well as a double exponential (dashed blue line).

4.2.2.4 Ion transfer

When considering the possibly harmful effects of pores, it is not only important to know how long a pore remains open, but also what can happen while it is open. Cells maintain a difference in ion concentration inside compared to outside. Knowing how the pore area changes with time,

we can calculate how much charge can pass through the pore. If we assume the difference in ion concentration remains fairly constant during transfer, we can also assume a constant current density through the pore, J . The total charge that passes through the pore is then

$$Q = \int_0^T J \cdot A_p(t) dt \quad (4.43)$$

where T is closing time and $A_p(t)$ is the pore area for which we can use the linear or quadratic approximations considered in the previous sections. I have calculated the total charge transfer for both the flat LB and vesicle cases. Table 4.4 shows the results for the linear and quadratic approximations.

Total charge transferred ($J \cdot \sigma^2 / \tau$)		
	Flat LB	Vesicle
Quadratic	5.3E3	19.8E3
Linear	5.2E3	19.6E3

Table 4.4: Total calculated charge transferred through pores using linear and quadratic approximations.

The differences in charge transfer between the linear and quadratic approximations are much smaller compared to differences in closing times. One reason is that the underestimates of area that take place in the linear approximations at early and late times, are compensated for by overestimates in the middle (see figures 4.2 and 4.6). Also, most of the charge transfer occurs at early times when the decrease in area is mostly linear. The differences between the linear and quadratic approximations are only 1.7% for the flat LB and 1.1% for the vesicle cases. It appears that the linear approximation predicted by Allen-Cahn works quite well for calculating charge transfer.

Chapter 5

CONCLUSION

I have looked at the interactions between nanoparticles (NP) and lipid bilayers (LB). Simple continuum models can be used to determine both the thermodynamics of NP/LB states and the dynamics of pore healing in LB. I used a coarse-grained lipid model to simulate the behavior in both cases.

In chapter 3 I looked at various equilibrium states resulting from NP/LB interactions. Using a continuum theory, I defined a free energy for each possible state (figures 3.1-3.4). The theory depends on the size and attraction strength of the NP and the macroscopic properties of the membrane such as the bending and stretching moduli. By comparing the free energies, I identified the equilibrium states under different conditions and constructed a phase diagram (figures 3.6-3.8). I varied the properties of the NP while fixing the membrane parameters, This was done for both spherical and rod-shaped nanoparticles.

The driving force behind these interactions is the attraction between the NP and the lipid heads and tails. This attraction favors wrapping of the NP by the LB. It can be wrapped by a double or single layer of lipids depending on whether it is attracted more to the lipid heads or tails. Total wrapping involves a bending energy which is independent of the NP size and is therefore the dominant contribution for small NP. In that case the adhesion, which is proportional to the surface area of the NP, can not overcome the cost of bending.

The stretching energy is proportional to the square of the NP surface area and therefore dominates for large NP. The stretching energy can be relieved by forming a pore in the LB at the cost of line energy around the edge of the pore. Very small NP will not become wrapped due to the overwhelming cost of bending. Slightly larger NP will become embedded in the LB. NP larger than a critical size cause pore formation in the LB.

Ginzburg and Balijepalli studied these small NP interactions using density functional theory [65]. In section 3.4 I compared their results with my continuum model predictions. The gen-

eral range of transitions is in decent agreement with my phase diagram (figure 3.9). The slight discrepancies in the transition points are due to simplifications in my model which I explained.

In section 3.5 I used a coarse-grained particle model to simulate the interactions under the same conditions. The NP sizes and attraction strengths I used were the same as those used by Ginzburg and Balijepalli. The resulting states were reasonably well predicted by the continuum model (figures 3.16 and 3.18).

I have compared three different techniques for studying NP/LB interactions which are all in general agreement about the range of transitions. Mutual agreement lends credibility to all three methods. Such a multiscale approach is a good way to study these kinds of systems. Simulations which can quickly and easily be run over a wide range of conditions are an excellent supplement to experiments which can be difficult and expensive. Continuum theory can identify the interesting regions of phase space and help direct the conditions for simulation and experiment.

I have found a particular set of NP properties which result in absorption and pore formation. Given the membrane properties of another system, this method could be used to predict the effects of NP interaction.

In chapter 4 I looked at the dynamics of pore healing. The evolution of a pore is determined by the line energy around the edge of the pore as well as the volume energy of the LB away from the pore. The volume energy is related to the stretching or compression of the LB. A compressed LB will want to spread out and will accelerate the closing of the pore. A stretched lipid bilayer will instead work to increase the size of the pore. The line energy is always a positive energy related to the bending modulus of the LB and is proportional to the circumference of the pore. The line energy acts to close the pore.

I showed that the volume energy contribution will change the area of the pore quadratically with time while the line energy contribution produces a linear decrease in pore area. If both energies are present, the evolution will have both a linear and a quadratic component. Using the same coarse-grained lipid model, I simulated the closing of a pore in a flat LB and also in a spherical vesicle. By fitting the pore area data, I was able to compare the relative importance of the linear and quadratic

contributions. In both the flat LB and the spherical vesicle cases, the pore area decreased quite linearly. The quadratic fit determined the pore closing time more accurately than the linear fit. The linear fit underestimated the closing time by 20% in the flat LB case and by only 7% in the spherical vesicle case.

Charge flow through a pore is proportional to the time integral of the pore area curve. The total charge flow predicted by the linear and quadratic fits agreed even better. The predicted charge flows differed by less than 2% between the flat LB and spherical vesicle cases (table 4.4).

APPENDICES

APPENDIX A: GINZBURG AND BALIJEPALLI EQUATIONS

Here I will elaborate on the TGMB equations used in section 2.5.1. I am mostly rehashing the thorough explanation given in the paper by Ginzburg and Balijepalli [65]. Once again, the total free energy can be written as

$$\frac{FN_D}{k_B T \rho_0 V} = f_1 + f_2 + f_3 + f_4 \quad (1)$$

$$f_1 = \frac{\varphi_P}{\alpha} \ln \left(\frac{Q_P}{V} \right) - \varphi_D \ln \left(\frac{Q_D}{V} \right) - N_D \varphi_W \ln \left(\frac{Q_W}{V} \right) \quad (2)$$

$$f_2 = \frac{1}{V} \int dr \left[\sum_{\alpha, \beta} \left(\chi_{\alpha\beta} N_D \right) \phi_\alpha(r) \phi_\beta(r) - \xi(r) \left(1 - \sum_{\alpha} \phi_\alpha(r) \right) \right] \quad (3)$$

$$f_3 = \frac{1}{V} \int dr \left[- \sum_{\alpha (\neq P)} w_\alpha(r) \phi_\alpha(r) - w_P(r) \rho_P(r) \right] \quad (4)$$

$$f_4 = \frac{1}{V} \int dr [\rho_P(r) \Psi_{CS}(\bar{\phi}_P(r))] \quad (5)$$

In the first equation (1) N_D is the degree of polymerization of the lipid diblocks or the number of segments in each lipid, either hydrophilic (H) or lipophilic (L). Each segment has a Khun length $a = 0.4$ nm and therefore a volume of $(\rho_0)^{-1} = 0.064$ nm³. V is simply the system volume.

The first term, f_1 (2), contains the entropic free energies. φ_P , φ_D , and φ_W are the volume fractions of the nanoparticle, lipids, and water respectively which add to one. Q_P , Q_D , and Q_W are the individual partition functions for each component. α is the particle to diblock volume ratio

$$\alpha = \frac{4\pi R_p^3 \rho_0}{3N_D} \quad (6)$$

where R_p is the radius of the nanoparticle.

The second term, f_2 (3), contains the local interactions determined by Flory-Huggins parameters [68, 69] as discussed in section 3.5.1. $\phi_\alpha(r)$ represents the local volume fraction of each

component. The last part of (3) also enforces incompressibility. $\xi(r)$ is a pressure field which I will define later in this section.

The third term, f_3 (4), introduces the chemical potential fields, w , which depend on the local interactions. $\rho_P(r)$ in (4) is the particle center density which is related to the particle's local volume fraction, $\phi_P(r)$, and “smoothed density” function, $\bar{\phi}_P(r)$, as follows

$$\phi_P(r) = \frac{1}{N_D} \int dr' \rho_P(r') \Theta \left(1 - \frac{|r-r'|}{(R_P/R_{gD})} \right) \quad (7)$$

$$\bar{\phi}_P(r) = \frac{1}{2^d N_D} \int dr' \rho_P(r') \Theta \left(1 - \frac{|r-r'|}{(2R_P/R_{gD})} \right) \quad (8)$$

d is the dimensionality of the simulation box. Θ is the Heaviside step function. $R_{gD} = a(N_D/6)^{1/2}$ is the radius of gyration of the diblock.

Finally, the fourth term, f_4 (5), contains the non-ideal hard-sphere interactions. It involves a density functional theory approximation used by Tarazona [80]. The hard-sphere fluid free energy is given by the Carnahan-Starling [81] equation of state

$$\Psi_{CS}(x) = \frac{4x - 3x^2}{(1-x)^2} \quad (9)$$

The partition functions used in f_1 (2) are given by

$$Q_W = \int \exp\{-w_W(r)\} dr \quad (10)$$

$$Q_P = \int \exp\{-w_P(r)\} dr \quad (11)$$

$$Q_D = \int q(r, 1) dr \quad (12)$$

The propagator $q(r, s)$ and its counterpart $q^\dagger(r, s)$ are defined by the following diffusion equations

$$\frac{\partial q(r, s)}{\partial s} = [\nabla^2 - w_{t(s)}] q(r, s) \quad (13)$$

$$\frac{\partial q^\dagger(r, s)}{\partial s} = [\nabla^2 - w_{t(s)}] q^\dagger(r, s) \quad (14)$$

s is an index denoting the position along the diblock which ranges from 0 to 1. $t(s) = L$ if $s < f$, and H otherwise. These equations are subject to the boundary conditions $q(r, 0) = q^\dagger(r, 1) = 1$.

The chemical potential fields, w are given by

$$w_H(r) = \chi_{HL}N_D\phi_L(r) + \chi_{HP}N_D\phi_P(r) + \xi(r) \quad (15)$$

$$w_L(r) = \chi_{HL}N_D\phi_H(r) + \chi_{WL}N_D\phi_W(r) + \xi(r) \quad (16)$$

$$w_W(r) = \chi_{WL}N_D\phi_L(r) + \chi_{WP}N_D\phi_P(r) + \xi(r) \quad (17)$$

$$\begin{aligned} w_P(r) = & \Psi_{CS}(\bar{\phi}_P(r)) + \frac{1}{N_D} \int dr' \Theta \left(1 - \frac{|r-r'|}{(R_P/R_{gD})} \right) \times \\ & [\chi_{HP}N_D\phi_H(r') + \chi_{WP}N_D\phi_W(r') + \xi(r')] + \\ & \frac{1}{2^d N_D} \int dr' \Theta \left(1 - \frac{|r-r'|}{(2R_P/R_{gD})} \right) \times [\rho_P(r') \Psi'_{CS}(\bar{\phi}_P(r'))] \end{aligned}$$

The pressure field, $\xi(r)$, is given by

$$\xi(r) = P(r) + \varepsilon (\phi_P(r) + \phi_W(r) + \phi_H(r) + \phi_L(r) - 1) \quad (18)$$

$$P(r) = \frac{H_W(r) + H_H(r) + H_L(r)}{3} \quad (19)$$

where $H_H(r)$, $H_L(r)$, and $H_W(r)$ are the right hand sides of equations (15-17) except for the ξ terms. ε is a heuristic parameter which Ginzburg and Balijepalli found to be convergent when set equal to 60.

The algorithm used by Ginzburg and Balijepalli was adapted from the one used by Drolet and Fredrickson [82] and in the original TGMB paper [66]. The first step is to initialize the chemical potential and pressure fields. Those can then be used to calculate the density fields with the help of equations (7) and (8) as well as these relations

$$\rho_P(r) = \frac{\phi_P}{\alpha} \frac{V}{Q_P} \exp[-w_P(r)] \quad (20)$$

$$\phi_W(r) = \phi_W \frac{V}{Q_P} \exp[-w_W(r)] \quad (21)$$

$$\phi_L(r) = \phi_D \frac{V}{Q_D} \int_0^f q(r,s) q^\dagger(r,s) ds \quad (22)$$

$$\phi_H(r) = \varphi_D \frac{V}{Q_D} > \int_f^1 q(r,s) q^\dagger(r,s) ds \quad (23)$$

$$\phi_H(r) + \phi_L(r) + \phi_P(r) + \phi_W(r) = 1 \quad (24)$$

Then the chemical potentials are updated according to

$$w_i^{t+1}(r) = (1 - \lambda_i) w_i^t(r) + \lambda_i \mu_i(r) \quad (25)$$

where t is the iteration number. The index i refers to H , L , W , or P . μ_i are the new chemical potentials calculated from equations (15-18). λ_i acts as an effective time step. Ginzburg and Balijepalli set $\lambda_P = 0$ in order to maintain a constant particle field while setting all other $\lambda_i = 0.025$. Finally, the pressure field is updated by equations (18) and (19). These steps are iterated until the fields converge.

APPENDIX B: NOSÉ-HOOVER THERMOSTAT/BAROSTAT

My simulations were run in the isothermal-isobaric ensemble fixing the number of particles, temperature, and pressure (NPT). The natural ensemble for molecular dynamics is the microcanonical ensemble in which the number of particles, volume, and total energy (NVE) are conserved. The isothermal-isobaric ensemble is more desirable because it can be directly compared to experiments in which temperature and pressure are controlled. The temperature and pressure are fixed using a Nosé-Hoover thermostat and barostat [73, 74] which I will explain now.

The standard Hamiltonian consists of kinetic energy including coordinates \mathbf{q}'_i and masses m_i as well as potential energy $\phi(\mathbf{q}')$. In this system the total energy will be conserved while the kinetic energy (temperature) and pressure are free to fluctuate. Nosé and Hoover introduced a different Hamiltonian which allows the total energy to fluctuate while conserving the temperature and pressure. The temperature and pressure can be included separately and I will discuss the thermostat first.

Thermostat

The Nosé-Hoover formulation transforms the real variables $(\mathbf{q}', \mathbf{p}', t')$ where \mathbf{p}' are the momenta, to virtual variables $(\mathbf{q}, \mathbf{p}, t)$ through the following transformations

$$\mathbf{q}'_i = \mathbf{q}_i \quad (26)$$

$$\mathbf{p}'_i = \mathbf{p}_i/s \quad (27)$$

$$t' = \int^t \frac{dt}{s} \quad (28)$$

Nosé interpreted these transformations as a rescaling of time by $dt' = dt/s$. The new Hamiltonian in terms of the virtual variables is

$$H = \sum_i \frac{\mathbf{p}_i^2}{2m_i s^2} + \phi(\mathbf{q}) + \frac{p_s^2}{2Q} + gkT \ln s \quad (29)$$

where g is the number of degrees of freedom, k is the Boltzmann constant, and T is the fixed external temperature. p_s is the conjugate momentum for s . Q behaves like an effective mass for the variable s . It determines the strength of the coupling between the system and the heat bath and sets a time scale for temperature fluctuations. A small value for Q corresponds to strong coupling and causes frequent velocity rescaling. Extremely small values can make the simulation unstable. A large value for Q corresponds to weak coupling and can cause very slow temperature equilibration. It has been shown that the most efficient equilibration occurs when the heat bath fluctuations are in resonance with the natural system fluctuations. Nosé derived an estimate of the heat bath frequency [83, 84] which I will now show. The Hamiltonian equations of motion are

$$\frac{d\mathbf{q}_i}{dt} = \frac{\partial H}{\partial \mathbf{p}_i} = \frac{\mathbf{p}_i}{m_i s^2} \quad (30)$$

$$\frac{d\mathbf{p}_i}{dt} = -\frac{\partial H}{\partial \mathbf{q}_i} = -\frac{\partial \phi}{\partial \mathbf{q}_i} \quad (31)$$

$$\frac{ds}{dt} = \frac{\partial H}{\partial p_s} = \frac{p_s}{Q} \quad (32)$$

$$\frac{dp_s}{dt} = -\frac{\partial H}{\partial s} = \left(\sum_i \frac{\mathbf{p}_i^2}{m_i s^2} - gkT \right) / s \quad (33)$$

Setting the time derivative of (32) equal to (33) a second order differential equation for s is obtained.

$$Q \frac{d^2 s}{dt^2} = -\frac{\partial H}{\partial s} = \left(\sum_i \frac{\mathbf{p}_i^2}{m_i s^2} - gkT \right) / s \quad (34)$$

When the system is in equilibrium s will fluctuate around its average value $\langle s \rangle$. We can then replace s with $\langle s \rangle + \delta s$ where δs contains the time dependence. A linear expansion of (34) gives

$$Q \frac{d^2 \delta s}{dt^2} = \frac{1}{\langle s \rangle} \left(\sum_i \frac{\mathbf{p}_i^2}{m_i \langle s \rangle^2} - gkT \right) - \frac{\delta s}{\langle s \rangle^2} \left(3 \sum_i \frac{\mathbf{p}_i^2}{m_i \langle s \rangle^2} - gkT \right) \quad (35)$$

For small values of Q or strong coupling to the heat bath the variable s will fluctuate more quickly than the particles in the system. The temperature can then be defined as

$$gkT = \sum_i \frac{\mathbf{p}_i^2}{m_i \langle s \rangle^2} \quad (36)$$

and (35) reduces to

$$\frac{d^2 \delta s}{dt^2} = \frac{-2gkT}{Q \langle s \rangle^2} \delta s \quad (37)$$

This is simply a harmonic oscillator equation whose angular frequency is

$$\omega = \sqrt{\frac{2gkT}{Q \langle s \rangle^2}} \quad (38)$$

The period of fluctuations in s is therefore

$$\tau = \frac{2\pi}{\omega} = \pi \langle s \rangle \sqrt{\frac{2Q}{gkT}} \quad (39)$$

Nosé found through simulations that $\langle s \rangle$ was on the order of one [83]. Multiple studies have been done to determine the effect of the parameter Q on simulations [83, 84, 75]. Fluctuations in s show up in the temperature and kinetic energy and can be on a much different time scale than the natural system fluctuations. If the frequency of s fluctuations are significantly larger than that of the system, it can result in an isolated mode and cause a non-Gaussian distribution of kinetic energy.

Figure B.1 shows a histogram of the kinetic energy of a simulated lipid bilayer for a small value of Q . Notice the slight dip at the center. This bimodal distribution was predicted by Nosé [84]. Extremely small values of Q can even make the simulations unstable, similar to using too large of a time step. Large values for Q correspond to weak coupling to the heat bath and result in long equilibration times. The optimal value for Q is one which places the fluctuations of s in resonance with those of the system. It will maintain a Gaussian distribution while being able to equilibrate in the least amount of time.

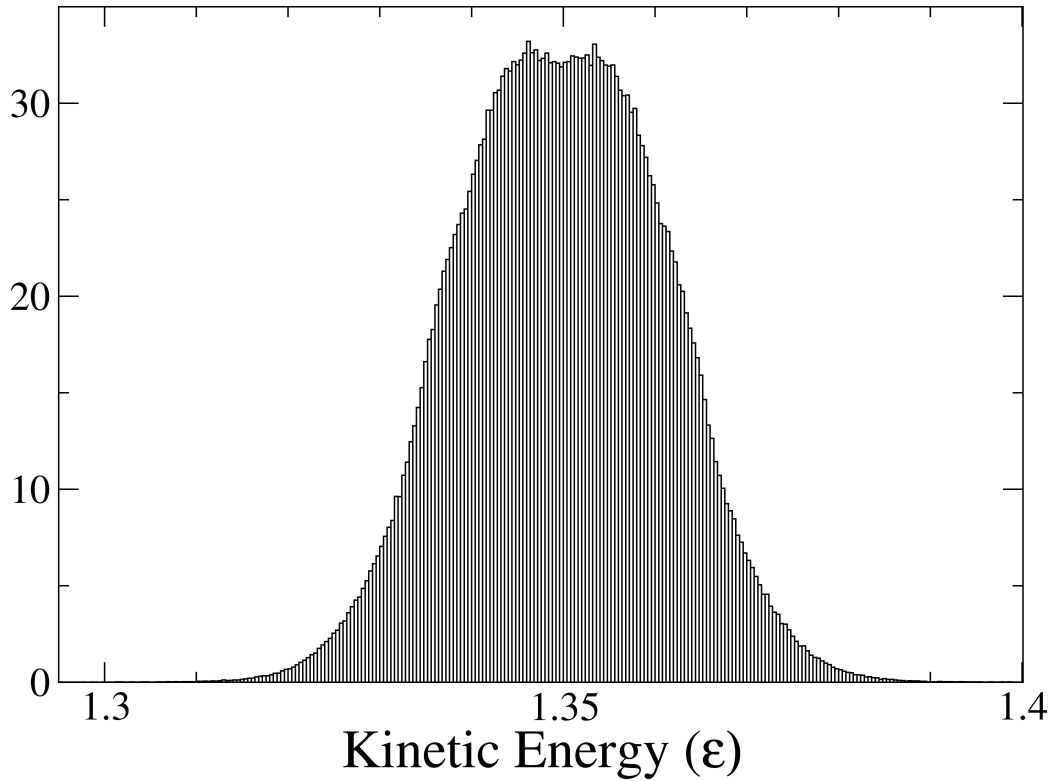


Figure B.1: Histogram of kinetic energy for strong heat bath coupling ($Q = 0.648, T_{damp} = 0.005$). The scaling variable s fluctuates faster than the system and causes a bimodal, non-Gaussian distribution.

The characteristic timescale of the system can be estimated from the potential. For small oscillations about the equilibrium positions the motion will appear harmonic. The spring constant for an equivalent harmonic potential can be found by taking the second derivative of the original potential and evaluating it at the equilibrium position. The potential between tail beads in the Cooke model is given by the sum of equations (2.1) and (2.4) and is represented in figure 2.1. The second derivative of that potential evaluated at $r = 2^{1/6} * b$ is approximately $57 \epsilon / \sigma^2$. The period then follows as

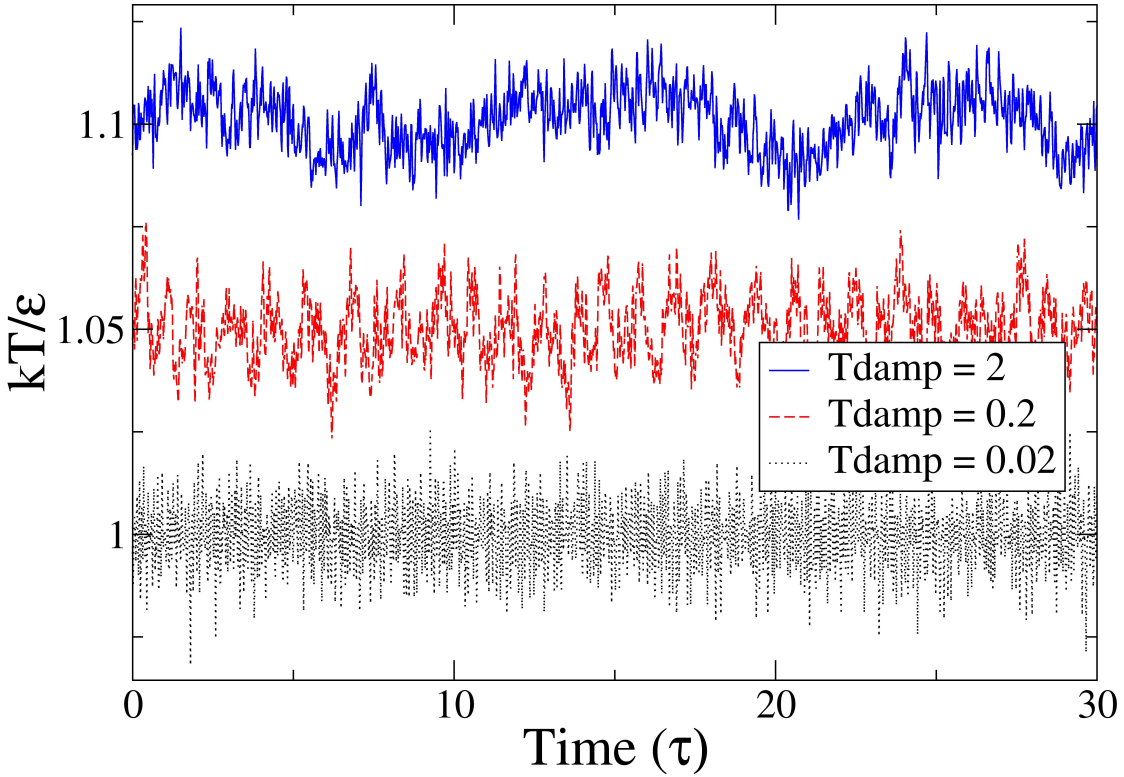


Figure B.2: Temperature versus time for various T_{damp} .

$$\tau' = 2\pi\sqrt{\frac{m}{k}} \approx 0.83 \quad (40)$$

The molecular dynamics package, LAMMPS, which I've used for my simulations uses a parameter called T_{damp} which is related to Q by

$$T_{\text{damp}} = \sqrt{\frac{Q}{gkt}} \quad (41)$$

They define T_{damp} as a rough timescale for temperature equilibration. It is directly proportional to the period derived in (39). Using the period in (40) implies a T_{damp} value of around 0.2.

I ran simulations of a 40x40 lipid bilayer at a temperature of $kT = \epsilon$. I varied $Tdamp$ from 0.02 to 2 to observe the effects of the damping parameter. The units for $Tdamp$ are the standard Lennard-Jones time units ($\sqrt{\frac{m\sigma^2}{\epsilon}}$). There were 9600 particles making $g = 28800$ degrees of freedom. Figure B.2 shows temperature versus time for three different values of $Tdamp$. All three simulations were run at the same temperature and are simply displaced for clarity.

The small features in the top two traces are due to the normal fluctuations of the system. The larger features in the top two traces are due to fluctuations of the heat bath. The bottom trace ($Tdamp = 0.02$) contains fluctuations which are faster than the normal system fluctuations and could prevent equilibration. In the middle trace ($Tdamp = 0.2$) the heat bath fluctuations are on the same order though slightly longer than the system fluctuations which is ideal. The system will be able to equilibrate and the temperature and kinetic energy will have the proper distribution. The heat bath coupling used in the top trace ($Tdamp = 2$) would also work but the system would take ten times longer to equilibrate. The LAMMPS documentation recommends trying a $Tdamp$ value equal to 100 time steps. Since my time step was 0.01, that would suggest a $Tdamp$ equal to 1 which I believe is larger than necessary in this case. Again, it would produce reasonable results, but simulations would have to be run for much longer. All simulations shown in other chapters were run with $Tdamp = 0.2$.

Barostat

Pressure can also be held constant through use of a barostat. The method was originally used by Andersen [85] and involves a rescaling of the coordinates by $V^{1/3}$, where V is the volume of the simulation box. Similar to equations (26-28)

$$\mathbf{q}'_i = \mathbf{q}_i V^{1/3} \quad (42)$$

$$\mathbf{p}'_i = \frac{\mathbf{p}_i}{sV^{1/3}} \quad (43)$$

$$t' = \int^t \frac{dt}{s} \quad (44)$$

The Hamiltonian for the isothermal/isobaric ensemble is

$$H = \sum_i \frac{\mathbf{p}_i^2}{2m_i s^2 V^{1/3}} + \phi(\mathbf{q}V^{1/3}) + \frac{p_s^2}{2Q} + gkT \ln s + \frac{p_V^2}{2W} + P_{ex}V \quad (45)$$

where P_{ex} is the externally applied pressure and p_V is the conjugate momentum of V . The fifth term on the right looks like a kinetic energy making W act as an effective mass similar to Q . It determines the strength of the pressure coupling and hence the frequency of volume fluctuations. W is sometimes referred to as the mass of an imagined piston that is controlling the pressure. While a normal piston compresses the volume along one dimension, these volume changes occur in all three dimensions.

Care must be taken in choosing a value for W . A value which is too small can again cause rapid, independent oscillation that produce a non-Gaussian ensemble distribution. Fluctuations that are short relative to the time step of the simulation can also cause instability. Similar to the derivation of temperature fluctuations above, Nosé and Klein [86] derived a relation between the period of volume fluctuations and W as follows

$$\tau_0 = 2\pi \sqrt{\frac{W}{3LB}} \quad (46)$$

where L is the length of the simulation box and B is the bulk modulus. In the same paper Nosé and Klein offer another approximation for the fluctuation period

$$\tau'_0 = 2\pi \frac{L}{v_1} \quad (47)$$

where v_1 is the speed of sound in the simulated material. If equations (46) and (47) are set equal, W can be solved for.

$$W = \frac{3BL^3}{v_1^2} \quad (48)$$

This can be further simplified because the bulk modulus and speed of sound are related as follows

$$B = \rho \frac{\partial P}{\partial \rho} \quad (49)$$

$$v_1^2 = \frac{\partial P}{\partial \rho} \quad (50)$$

where P is pressure and ρ is the mass density. Therefore

$$B = \rho v_1^2 \quad (51)$$

Equation 48 can then be simplified to

$$W = 3L^3 \rho = \frac{3L^3 mN}{V} \quad (52)$$

where m is the mass per particle which is equal to one. L is the length of the simulation box along which pressure waves propagate. In my simulations I'm interested in fluctuations parallel to the lipid bilayer surface or the xy plane. I also use square bilayers so that

$$L = L_x = L_y \quad (53)$$

The volume of the bilayer is equal to the area times the height or thickness of the bilayer (h)

$$V = L^2 h \quad (54)$$

W can once again be reduced to

$$W = \frac{3NL}{h} \quad (55)$$

LAMMPS sets W through another parameter called $Pdamp$ defined as

$$Pdamp = \sqrt{\frac{W}{NkT}} \quad (56)$$

They describe it as the timescale for pressure equilibration. Substituting (55) into (56) gives

$$Pdamp = \sqrt{\frac{3L}{kTh}} \quad (57)$$

The units for $Pdamp$ are again the standard Lennard-Jones time units ($\sqrt{\frac{m\sigma^2}{\epsilon}}$). Using the approximate dimensions of my bilayer ($40 \times 40 \times 5 \sigma^3$) and my temperature of $kT = 0.9 \epsilon$ implies that $Pdamp$ should be around 5. That corresponds to 1000 time steps which is exactly what the LAMMPS documentation recommends. Since all of my simulations use the same size bilayer, I have used this $Pdamp$ value for all of them.

BIBLIOGRAPHY

BIBLIOGRAPHY

- [1] Wen-Che Hou, Babak Yaghoubi Moghadam, Charlie Corredor, Paul Westerhoff, and Jonathan D Posner. Distribution of functionalized gold nanoparticles between water and lipid bilayers as model cell membranes. *Environmental science & technology*, 46(3):1869–76, February 2012.
- [2] Yuri Roiter, Maryna Ornatska, Aravind R Rammohan, Jitendra Balakrishnan, David R Heine, and Sergiy Minko. Interaction of lipid membrane with nanostructured surfaces. *Langmuir : the ACS journal of surfaces and colloids*, 25(11):6287–99, June 2009.
- [3] Yuri Roiter, Maryna Ornatska, Aravind R Rammohan, Jitendra Balakrishnan, David R Heine, and Sergiy Minko. Interaction of nanoparticles with lipid membrane. *Nano letters*, 8(3):941–4, March 2008.
- [4] Pascale R Leroueil, Stephanie a Berry, Kristen Duthie, Gang Han, Vincent M Rotello, Daniel Q McNerny, James R Baker, Bradford G Orr, and Mark M Banaszak Holl. Wide varieties of cationic nanoparticles induce defects in supported lipid bilayers. *Nano letters*, 8(2):420–4, February 2008.
- [5] Pascale R Leroueil, Seungpyo Hong, Almut Mecke, James R Baker, Bradford G Orr, and Mark M Banaszak Holl. Nanoparticle interaction with biological membranes: does nanotechnology present a Janus face? *Accounts of chemical research*, 40(5):335–42, May 2007.
- [6] Seungpyo Hong, Pascale R Leroueil, Elizabeth K Janus, Jennifer L Peters, Mary-Margaret Kober, Mohammad T Islam, Bradford G Orr, James R Baker, and Mark M Banaszak Holl. Interaction of polycationic polymers with supported lipid bilayers and cells: nanoscale hole formation and enhanced membrane permeability. *Bioconjugate chemistry*, 17(3):728–34, 2006.
- [7] S a Klein, S J Wilk, T J Thornton, and J D Posner. Formation of nanopores in suspended lipid bilayers using quantum dots. *Journal of Physics: Conference Series*, 109:012022, March 2008.
- [8] Maurits R R de Planque, Sara Aghdaei, Tiina Roose, and Hywel Morgan. Electrophysiological Characterization of Membrane Disruption by Nanoparticles - Supporting Information. *ACS nano*, pages 8–10, April 2011.
- [9] Nastassja Lewinski, Vicki Colvin, and Rebekah Drezek. Cytotoxicity of nanoparticles. *Small (Weinheim an der Bergstrasse, Germany)*, 4(1):26–49, January 2008.
- [10] Wim H De Jong and Paul J a Borm. Drug delivery and nanoparticles: applications and hazards. *International journal of nanomedicine*, 3(2):133–49, January 2008.
- [11] M Wang and M Thanou. Targeting nanoparticles to cancer. *Pharmacological research : the official journal of the Italian Pharmacological Society*, 62(2):90–9, August 2010.

- [12] Alexander P. Lyubartsev and Alexander L. Rabinovich. Recent development in computer simulations of lipid bilayers. *Soft Matter*, 7(1):25, 2011.
- [13] Jan Hermans, Herman J. C. Berendsen, Wilfred F. Van Gunsteren, and Johan P. M. Postma. A consistent empirical potential for water-protein interactions. *Biopolymers*, 23(8):1513–1518, August 1984.
- [14] W F van Gunsteren, SR Billeter, AA Eising, PH Hunenberger, P Kruger, AE Mark, WRP Scott, and IG Tironi. *Biomolecular Simulation: The GROMOS96 Manual and User Guide*. Hochschulverlag AG, ETH Zurich, 1996.
- [15] Nathan Schmid, Andreas P Eichenberger, Alexandra Choutko, Sereina Riniker, Moritz Winger, Alan E Mark, and Wilfred F van Gunsteren. Definition and testing of the GROMOS force-field versions 54A7 and 54B7. *European biophysics journal : EBJ*, 40(7):843–56, July 2011.
- [16] David Poger, Wilfred F Van Gunsteren, and Alan E Mark. A new force field for simulating phosphatidylcholine bilayers. *Journal of computational chemistry*, 31(6):1117–25, April 2010.
- [17] Alexander D. MacKerell, Joanna Wiorkiewicz-Kuczera, and Martin Karplus. An all-atom empirical energy function for the simulation of nucleic acids. *Journal of the American Chemical Society*, 117(48):11946–11975, December 1995.
- [18] A. D. MacKerell, D Bashford, R. L. Dunbrack, J D Evanseck, M J Field, S Fischer, J Gao, H Guo, S Ha, D. Joseph-McCarthy, L Kuchnir, K Kuczera, F T K Lau, C Mattos, S Michnick, T Ngo, D T Nguyen, B Prodhom, W E Reiher, B Roux, M Schlenkrich, J C Smith, R Stote, J Straub, M Watanabe, J. Wiórkiewicz-Kuczera, D Yin, and M Karplus. All-Atom Empirical Potential for Molecular Modeling and Dynamics Studies of Proteins. *The Journal of Physical Chemistry B*, 102(18):3586–3616, April 1998.
- [19] Jeffery B Klauda, Richard M Venable, J Alfredo Freites, Joseph W O’Connor, Douglas J Tobias, Carlos Mondragon-Ramirez, Igor Vorobyov, Alexander D MacKerell, and Richard W Pastor. Update of the CHARMM all-atom additive force field for lipids: validation on six lipid types. *The journal of physical chemistry. B*, 114(23):7830–43, June 2010.
- [20] Scott J Weiner, Peter A Kollman, David A Case, U Chandra Singh, Caterina Ghio, Guliano Alagona, Salvatore Profeta, and Paul Weiner. A new force field for molecular mechanical simulation of nucleic acids and proteins. *Journal of the American Chemical Society*, 106(3):765–784, February 1984.
- [21] Junmei Wang, Romain M Wolf, James W Caldwell, Peter a Kollman, and David a Case. Development and testing of a general amber force field. *Journal of computational chemistry*, 25(9):1157–74, July 2004.
- [22] Balázs Jójárt and Tamás A Martinek. Performance of the general amber force field in modeling aqueous POPC membrane bilayers. *Journal of computational chemistry*, 28(12):2051–8, September 2007.

- [23] D Peter Tieleman. The molecular basis of electroporation. *BMC biochemistry*, 5:10, July 2004.
- [24] Mounir Tarek. Membrane electroporation: a molecular dynamics simulation. *Biophysical journal*, 88(6):4045–53, June 2005.
- [25] Steve O Nielsen, Carlos F Lopez, Goundla Srinivas, and Michael L Klein. Coarse grain models and the computer simulation of soft materials. *Journal of Physics: Condensed Matter*, 16(15):R481–R512, April 2004.
- [26] Grace Brannigan, Lawrence C-L Lin, and Frank L H Brown. Implicit solvent simulation models for biomembranes. *European biophysics journal : EBJ*, 35(2):104–24, January 2006.
- [27] M Muller, K Katsov, and M Schick. Biological and synthetic membranes: What can be learned from a coarse-grained description? *Physics Reports*, 434(5-6):113–176, November 2006.
- [28] M Venturoli, M Maddalenasperotto, M Kranenburg, and B Smit. Mesoscopic models of biological membranes. *Physics Reports*, 437(1-2):1–54, December 2006.
- [29] Gary S Ayton, Will G Noid, and Gregory A Voth. Systematic Coarse Graining of Biomolecular and Soft-Matter Systems. *MRS Bulletin*, 32(November):929–934, 2007.
- [30] Sandra V Bennun, Matthew I Hoopes, Chenyue Xing, and Roland Faller. Coarse-grained modeling of lipids. *Chemistry and physics of lipids*, 159(2):59–66, June 2009.
- [31] T. Murtola, A. Bunker, I. Vattulainen, M. Deserno, and M. Karttunen. Multiscale modeling of emergent materials: biological and soft matter. *Physical Chemistry Chemical Physics*, 11(12):1869–1892, 2009.
- [32] Gary Ayton and Gregory a Voth. Bridging microscopic and mesoscopic simulations of lipid bilayers. *Biophysical journal*, 83(6):3357–70, December 2002.
- [33] J M Drouffe, a C Maggs, and S Leibler. Computer simulations of self-assembled membranes. *Science (New York, N.Y.)*, 254(5036):1353–6, November 1991.
- [34] Oded Farago. “Water-free” computer model for fluid bilayer membranes. *The Journal of Chemical Physics*, 119(1):596, 2003.
- [35] Grace Brannigan and Frank L H Brown. Solvent-free simulations of fluid membrane bilayers. *The Journal of chemical physics*, 120(2):1059–71, January 2004.
- [36] Ira Cooke, Kurt Kremer, and Markus Deserno. Tunable generic model for fluid bilayer membranes. *Physical Review E*, 72(1):011506, July 2005.
- [37] Ira R Cooke and Markus Deserno. Solvent-free model for self-assembling fluid bilayer membranes: stabilization of the fluid phase based on broad attractive tail potentials. *The Journal of chemical physics*, 123(22):224710, December 2005.

- [38] Berk Hess, S León, N Van Der Vegt, and Kurt Kremer. Long time atomistic polymer trajectories from coarse grained simulations: bisphenol-A polycarbonate. *Soft Matter*, 2(5):409, 2006.
- [39] V. A. Harmandaris, N. P. Adhikari, N. F. A. van der Vegt, K. Kremer, B. A. Mann, R. Voelkel, H. Weiss, and CheeChin Liew. Ethylbenzene Diffusion in Polystyrene: United Atom Atomistic/Coarse Grained Simulations and Experiments. *Macromolecules*, 40(19):7026–7035, September 2007.
- [40] Markus Deserno. Mesoscopic Membrane Physics: Concepts, Simulations, and Selected Applications. *Macromolecular Rapid Communications*, 30(9-10):752–771, May 2009.
- [41] P F Fahey and W W Webb. Lateral diffusion in phospholipid bilayer membranes and multilamellar liquid crystals. *Biochemistry*, 17(15):3046–53, July 1978.
- [42] Rudiger Goetz and Reinhard Lipowsky. Computer simulations of bilayer membranes: Self-assembly and interfacial tension. *The Journal of Chemical Physics*, 108(17):7397, 1998.
- [43] Mark Stevens, Jan Hoh, and Thomas Woolf. Insights into the Molecular Mechanism of Membrane Fusion from Simulation: Evidence for the Association of Splayed Tails. *Physical Review Letters*, 91(18):188102, October 2003.
- [44] C. Loison, M. Mareschal, K. Kremer, and F. Schmid. Thermal fluctuations in a lamellar phase of a binary amphiphile–solvent mixture: A molecular-dynamics study. *The Journal of Chemical Physics*, 119(24):13138, 2003.
- [45] C Loison, M Mareschal, and F Schmid. Pores in bilayer membranes of amphiphilic molecules: coarse-grained molecular dynamics simulations compared with simple mesoscopic models. *The Journal of chemical physics*, 121(4):1890–900, July 2004.
- [46] Siewert J Marrink, H Jelger Risselada, Serge Yefimov, D Peter Tieleman, and Alex H de Vries. The MARTINI force field: coarse grained model for biomolecular simulations. *The journal of physical chemistry. B*, 111(27):7812–24, July 2007.
- [47] Siewert J. Marrink, Alex H. de Vries, and Alan E. Mark. Coarse Grained Model for Semi-quantitative Lipid Simulations. *The Journal of Physical Chemistry B*, 108(2):750–760, January 2004.
- [48] John C. Shelley, Mee Y. Shelley, Robert C. Reeder, Sanjoy Bandyopadhyay, and Michael L. Klein. A Coarse Grain Model for Phospholipid Simulations. *The Journal of Physical Chemistry B*, 105(19):4464–4470, May 2001.
- [49] John C. Shelley, Mee Y. Shelley, Robert C. Reeder, Sanjoy Bandyopadhyay, Preston B. Moore, and Michael L. Klein. Simulations of Phospholipids Using a Coarse Grain Model. *The Journal of Physical Chemistry B*, 105(40):9785–9792, October 2001.
- [50] P. J Hoogerbrugge and J. M. V. A Koelman. Simulating Microscopic Hydrodynamic Phenomena with Dissipative Particle Dynamics. *Europhysics Letters (EPL)*, 19(3):155–160, June 1992.

- [51] J. M. V. A Koelman and P. J Hoogerbrugge. Dynamic Simulations of Hard-Sphere Suspensions Under Steady Shear. *Europhysics Letters (EPL)*, 21(3):363–368, January 1993.
- [52] R D Groot and K L Rabone. Mesoscopic simulation of cell membrane damage, morphology change and rupture by nonionic surfactants. *Biophysical journal*, 81(2):725–36, August 2001.
- [53] Hwanky Lee and R.G. Larson. Membrane Pore Formation Induced by Acetylated and Polyethylene Glycol-Conjugated Polyamidoamine Dendrimers. *The Journal of Physical Chemistry C*, pages 5316–5322, 2011.
- [54] Shikha Nangia and Radhakrishna Sureshkumar. Effects of Nanoparticle Charge and Shape Anisotropy on Translocation through Cell Membranes. *Langmuir : the ACS journal of surfaces and colloids*, 28(51):17666–71, December 2012.
- [55] P B Canham. The minimum energy of bending as a possible explanation of the biconcave shape of the human red blood cell. *Journal of theoretical biology*, 26(1):61–81, January 1970.
- [56] W. Helfrich. Elastic properties of lipid bilayers: theory and possible experiments. *Z. Naturforsch*, 28(11):693–703, 1973.
- [57] Frank L H Brown. Elastic modeling of biomembranes and lipid bilayers. *Annual review of physical chemistry*, 59:685–712, January 2008.
- [58] E Evans. Bending Resistance and Chemically Induced Moments in Membrane Bilayers. *Biophysical Journal*, 14(12):923–931, December 1974.
- [59] Jejoong Yoo, Meyer B Jackson, and Qiang Cui. A comparison of coarse-grained and continuum models for membrane bending in lipid bilayer fusion pores. *Biophysical journal*, 104(4):841–52, February 2013.
- [60] Markus Deserno and William M. Gelbart. Adhesion and Wrapping in Colloid Vesicle Complexes. *The Journal of Physical Chemistry B*, 106(21):5543–5552, May 2002.
- [61] Markus Deserno. Elastic deformation of a fluid membrane upon colloid binding. *Physical Review E*, 69(3):031903, March 2004.
- [62] Markus Deserno. When do fluid membranes engulf sticky colloids? *Journal of Physics: Condensed Matter*, 16(22):S2061–S2070, June 2004.
- [63] Teresa Ruiz-Herrero, Enrique Velasco, and Michael F Hagan. Mechanisms of budding of nanoscale particles through lipid bilayers. *The journal of physical chemistry. B*, 116(32):9595–603, August 2012.
- [64] Reid C. Van Lehn and Alfredo Alexander-Katz. Penetration of lipid bilayers by nanoparticles with environmentally-responsive surfaces: simulations and theory. *Soft Matter*, 7(24):11392, 2011.
- [65] Valeriy V Ginzburg and Sudhakar Balijepalli. Modeling the thermodynamics of the interaction of nanoparticles with cell membranes. *Nano letters*, 7(12):3716–22, December 2007.

- [66] R B Thompson, V V Ginzburg, M W Matsen, and a C Balazs. Predicting the mesophases of copolymer-nanoparticle composites. *Science (New York, N.Y.)*, 292(5526):2469–72, June 2001.
- [67] Russell B. Thompson, Valeriy V. Ginzburg, Mark W. Matsen, and Anna C. Balazs. Block Copolymer-Directed Assembly of Nanoparticles: Forming Mesoscopically Ordered Hybrid Materials. *Macromolecules*, 35(3):1060–1071, January 2002.
- [68] Maurice L. Huggins. Solutions of Long Chain Compounds. *The Journal of Chemical Physics*, 9(5):440, 1941.
- [69] Paul J. Flory. Thermodynamics of High Polymer Solutions. *The Journal of Chemical Physics*, 9(8):660, March 1941.
- [70] Yang Li and Ning Gu. Thermodynamics of charged nanoparticle adsorption on charge-neutral membranes: a simulation study. *The journal of physical chemistry. B*, 114(8):2749–54, March 2010.
- [71] Jiaqi Lin, Hongwu Zhang, Zhen Chen, and Yonggang Zheng. Penetration of lipid membranes by gold nanoparticles: insights into cellular uptake, cytotoxicity, and their relationship. *ACS nano*, 4(9):5421–9, September 2010.
- [72] T V Tolpekina, W K den Otter, and W J Briels. Simulations of stable pores in membranes: system size dependence and line tension. *The Journal of chemical physics*, 121(16):8014–20, October 2004.
- [73] Shuichi Nose. A unified formulation of the constant temperature molecular dynamics methods. *The Journal of Chemical Physics*, 81(1):511, 1984.
- [74] WG Hoover. Canonical dynamics: Equilibrium phase-space distributions. *Physical Review A*, 31(3):1695–1697, 1985.
- [75] K. Cho and JD Joannopoulos. Ergodicity and dynamical properties of constant-temperature molecular dynamics. *Physical Review A*, 45(10):7089, 1992.
- [76] AA Griffith. The phenomena of rupture and flow in solids. *Philosophical Transactions of the Royal Society of London, A*, 221:163–198, 1921.
- [77] SM Allen and JW Cahn. A microscopic theory for antiphase boundary motion and its application to antiphase domain coarsening. *Acta Metallurgica*, 27:1085–1095, 1979.
- [78] John W. Cahn and John E. Hilliard. Free Energy of a Nonuniform System. I. Interfacial Free Energy. *The Journal of Chemical Physics*, 28(2):258, 1958.
- [79] Pavel L. Krapivsky, Sidney Redner, and Eli Ben-Naim. *A Kinetic View of Statistical Physics*. 2010.
- [80] P. Tarazona. A density functional theory of melting. *Molecular physics*, 52(1):81–96, August 1984.

- [81] Norman F Carnahan and Kenneth E Starling. Equation of state for nonattracting rigid spheres. *The Journal of Chemical Physics*, 51(2):635, 1969.
- [82] F Drolet and Glenn H Fredrickson. Combinatorial screening of complex block copolymer assembly with self-consistent field theory. *Physical review letters*, 83(1):4317–4320, 1999.
- [83] Shichi Nosé. A molecular dynamics method for simulations in the canonical ensemble. *Molecular Physics*, 52(2):255–268, June 1984.
- [84] Shuichi Nosé. Constant temperature molecular dynamics methods. *Progress of theoretical physics. Supplement*, (103):1–46, 1991.
- [85] Hans C. Andersen. Molecular dynamics simulations at constant pressure and/or temperature. *The Journal of Chemical Physics*, 72(4):2384, 1980.
- [86] Shuichi Nosé and M.L. Klein. Constant pressure molecular dynamics for molecular systems. *Molecular Physics*, 50(5):1055–1076, December 1983.